

Charge carrier effects in free standing Si membranes investigated by linear and second harmonic optical techniques

by

Wilfrid Innocent Ndebeka



*Dissertation presented for the degree of Doctorate of
Philosophy in the Faculty of Sciences at Stellenbosch
University*

Supervisors:

Prof. Erich G. Rohwer
Dr. Pieter H. Neethling
Dr. Christine M. Steenkamp
Prof. Herbert Stafast

December 2016

Declaration

By submitting this dissertation electronically, I declare that the entirety of the work contained therein is my own, original work, that I am the sole author thereof (save to the extent explicitly otherwise stated), that reproduction and publication thereof by Stellenbosch University will not infringe any third party rights and that I have not previously in its entirety or in part submitted it for obtaining any qualification.

Copyright © 2016 Stellenbosch University
All rights reserved.

Abstract

Charge carrier effects in free standing Si membranes investigated by linear and second harmonic optical techniques

W.I. Ndebeka

*Department of Physics,
University of Stellenbosch,
Private Bag X1, Matieland 7602,
South Africa.*

Dissertation: PhD

December 2016

Silicon (Si) based materials have been of technological importance throughout the years and today silicon remains a leading material in microelectronics industries. The silicon/silicon dioxide (Si/SiO₂) interface has been one of the most studied systems in the realms of material and condensed matter physics. Despite the great outpouring research and huge technological success, there has been little effort to construct a comprehensive, unified microphysical model of the Si/SiO₂ interface. The optical properties, both linear and nonlinear, of the interface region are of interest since they vary considerably from those of the adjacent bulk phases. Second harmonic generation is used as a versatile tool to investigate surfaces and buried interfaces of centrosymmetric materials such as Si. Specifically, the electric field induced second harmonic (EFISH) generation process is used as a valuable technique to investigate the mechanisms of charge transfer and trap generation and population, both by electrons and holes being pumped across the interface. In this work, the transmission of the fundamental laser beam (90 fs pulse trains at 80 MHz repetition rate, 800 nm) through 10 μm to 30 μm thick silicon (Si) membranes as well as simultaneous measurements of the electric field induced second harmonic (EFISH) generated in reflection from and transmission through the Si membranes are reported for the first time. The transmission of the laser power through Si membranes, irradiated at

ABSTRACT

iii

an incident angle of 45° , shows an increase with increased power, then reaches a maximum, and finally continues to decrease considerably as the incident power is increased. A similar behavior is observed with the EFISH signals in transmission of the Si membranes. The nonlinear behavior of the fundamental transmitted signal is attributed to free charge carrier absorption (FCA) in Si. The experimental setup and these results are discussed in this thesis.

Uittreksel

Ladingsdraer-effekte in vrystaande silikon membrane ondersoek deur lineêre en optiese tweede harmoniese tegnieke

W.I. Ndebeka

*Fisika Departement,
Universiteit van Stellenbosch,
Privaatsak X1, Matieland 7602,
Suid Afrika.*

Proefskrif: PhD

Desember 2016

Silikon (Si) gebaseerde materiale is reeds vir jar van tegnologiese belang en vandag Si steeds 'n prominente materiaal in die mikroëlektronika nywerheid. Die silikon/silikondioksied (Si/SiO₂) skeidingsvlak is een van die mees bestudeerde stelsels in die navorsingsveld van materiaal- en vastetoestand- Fisika. Ten spyte van die omvangryke navorsing en groot tegnologiese sukses, is daar nog min werk gedoen om 'n omvattende, verenigde fisiese model op die mikroskopiese skaal van die Si/SiO₂ skeidingsvlak te ontwikkel. Die optiese eienskappe, sowel lineêre en nie-lineêre, van die skeidingsvlak-gebied is van belang aangesien die oorgangsgebied se eienskappe beduidend verskil van dié van aangrensende uniforme fases. Tweede harmoniek generering word gebruik as 'n veelsydige tegniek om oppervlaktes en interne skeidingsvlakke van sentrosimmetriese materiale soos Si te ondersoek. Die elektriese veld geïnduseerde tweede harmoniek (EFISH) genereringsproses word spesifiek gebruik as 'n veelsydige tegniek om die meganismes van ladingsoordrag, ladingsval-generering en die bevolking van ladingsvalle te ondersoek-, deur beide elektrone en holtes oor die skeidingsvlak te pomp. In hierdie werk word vir die eerste keer verslag gedoen van meting van die transmissie van die fundamentele laserbundel (90 fs pulse teen 'n herhalings tempo van 80 MHz, 800 nm) deur 10 mikrometer tot 30 mikrometer dik silikon (Si) membrane, sowel as gelyktydige meting van die

electriese veld geïnduseerde tweede harmoniek (EFISH) wat gegenereer word in refleksie van en transmissie deur die Si membrane. Die deurgelate fundamentele laserdrywing deur Si membrane, teen 45 grade invalshoek, too 'n toename met verhoogde drywing van die invallende lig, dan 'n maksimum, en verminder daarna aansienlik met verdere toename in drywing van die invallende lig. Die nie-lineêre gedrag van die fundamentele sein in transmissie word toegeskryf aan vrye ladingsdraer-absorpsie (FCA) in Si. Die eksperimentele opstelling en hierdie resultate sal in hierdie proefskrif bespreek word.

Acknowledgements

I would like to thank the African Laser Centre (ALC), the Council for Scientific and Industrial Research (CSIR) and the University of Stellenbosch for funding my doctoral studies. My thanks also go to the Laser Research Institute (LRI) for providing the equipment used.

I would like to express my deepest gratitude to my supervisors Prof E. G. Rohwer, Dr P. H. Neethling, Dr, C. M. Steenkamp and Prof H. Stafast for their guidance, encouragement, support and understanding throughout my studies: without your patience and wisdom, my PhD thesis work would have been a frustrating pursuit.

My sincere appreciations also go to all members of the LRI for fruitful discussions during our weekly LRI meeting and for the excellent collaboration.

I would not forget my friend and family who shared their love, moral and financial support which have tremendously contributed in the accomplishment of my studies.

Dedications

I dedicate this thesis to my father for his love, encouragement and support and to my late mother who could not see the completion of my studies: she taught me to persevere when I wanted to quit and with the help of God she prepared me to face challenges with faith and humility. Though she is no longer with us, I can still feel her presence and support which urge me to achieve my goals in life.

Contents

Declaration	i
Abstract	ii
Uittreksel	iv
Acknowledgements	vi
Dedications	vii
Contents	viii
List of Figures	x
List of Tables	xiv
1 Introduction	1
2 Research overview	5
3 Physical background	9
3.1 Electromagnetic waves	9
3.2 Light propagation	14
3.3 Free charge carrier absorption	17
3.4 Nonlinear optical interactions	18
3.5 Electric field induced second harmonic (EFISH) generation	28
4 Experimental	34
4.1 Experimental setup	34
4.2 Sample fabrication and preparation	36
4.3 Laser pulse characterization	37
5 Results	44
5.1 Reflection and transmission of the fundamental laser beam	45
5.2 Estimation of the thickness of the Si sample	50
5.3 Time-dependent second harmonic measurements	53

<i>CONTENTS</i>	ix
6 Discussion	63
6.1 Reflection and transmission of the fundamental laser wavelength power	63
6.2 Time-dependent second harmonic measurements	73
7 Summary, conclusion and outlook	83
List of References	86

List of Figures

1.1	Schematic representation of the laser beam reflection from and transmission through a thin silicon membrane at an external incident angle $\theta = 45^\circ$ and the propagation angle inside silicon $\gamma \approx 11^\circ$.	3
1.2	EFISH signals obtained by the same incident power (100 mW) recorded in transmission (a) and reflection (b) from a $10 \mu\text{m}$ thick Si membrane.	3
3.1	Light ray incident on the separation interface of two media with refractive indices n_i and n_t , respectively. The incident electric field is perpendicular to the plane of incidence; θ_i and θ_t are the incident and transmitted angles. i , r and t are subscripts for the incident, reflected and transmitted. \vec{E} , \vec{B} and \vec{k} are the electric, magnetic and wave propagation vectors, respectively.	12
3.2	Light ray incident on the separation surface of two media with refractive indices n_i and n_t , respectively. The incident electric field is parallel to the plane of incidence; θ_i and θ_t are the incident and transmitted angles, respectively.	15
3.3	Reflectance and transmittance of fundamental light incident on Si with $n_i = 1$ and $n_t = 3.69$	17
	(a) Reflectance	17
	(b) Transmittance	17
3.4	Energy band diagram showing electrons and holes. E_c is the minimum conduction electron energy, E_v the minimum hole energy and E_g the energy band gap.	18
3.5	Energy levels in Si/SiO ₂ for intrinsic and weakly doped silicon: CB, conduction band; VB, valence band; E_{vac} , vacuum energy level.	30
3.6	Schematic energy band diagram in Si/SiO ₂ system when illuminated with a femtosecond laser light at low incident peak intensities; CB _{direct} and CB _{indirect} are the direct and indirect conduction band, respectively; VB is the valence band; E_{vac} , the vacuum energy level; transfer of electron into SiO ₂ is achieved by three-photon and cascade of one- and two-photon processes; electron can be trapped at SiO ₂ /air interface (A), in the bulk Si (B) and at the Si/SiO ₂ interface (C).	32

3.7	Hole (h^+) transfer and trapping in Si/SiO ₂ after injection by four-photon excitation: decrease of net interfacial electric field. E_{vac} , vacuum energy level; E_{el} , electric field due to electron transition and trapping from Si to SiO ₂ ; E_h , small contribution of hole processes.	33
4.1	Schematic diagram of the experimental setup used for simultaneously measuring second harmonic signals in reflection and in transmission from a thin Si membrane; Ti:Sa, Ti:Sapphire femtosecond laser; $\lambda/2$, half wave plate; F, filter; P_i , polarizers; L_i , lenses; M, silver mirror; PM, photomultiplier tube; ω and 2ω , fundamental and second harmonic signals, respectively; (A) black box shielding PMTs from external light; S, XY translation stage with rotating platform.	35
4.2	Photograph of arrays of weakly p-doped $3 \times 3 \text{ mm}^2$ Si(100) with doping concentration of $2.67 \times 10^{15} \text{ cm}^{-3}$	36
4.3	Measured pulse train of the femtosecond laser.	38
4.4	illustration of Michelson interferometer. B.S, beam splitter, M_i , silver mirrors; AlGaAs, aluminum gallium arsenide photo detector.	38
4.5	Measured spectrum of the optical femtosecond laser used. The pulse duration is calculated using Eq. (4.3.3).	39
4.6	Autocorelation trace measured using Michelson interferometer of Fig. 4.4.	40
4.7	Simultaneous measurement of the beam radius in reflection and in transmission at the sample position $z = 0$ on a thin Si membrane. Solid curves are fits according to Eq. (4.3.11).	41
4.8	Calibration of the photomultiplier tubes; a) in transmission geometry and b) in reflection geometry	42
	(a) Transmission	42
	(b) Reflection	42
5.1	Reflected laser power P_{ref} from thin Si membranes as a function of the incident power P_{in} yielding a reflectivity $R = 0.15 \pm 0.01$. Solid lines are linear fits.	46
5.2	Average laser transmitted power P_{trans} of a fs laser pulse train using thin Si membranes as a function of the incident power P_{in} . Solid lines are fits according to Eq. (6.1.12) with n considered as a variable parameter in the fit.	46
5.3	Average laser transmitted power P_{trans} of a fs laser pulse train using thin Si membranes as a function of the incident power P_{in} . Solid lines are fits according to Eq. (6.1.12) with $n = 2$ fixed.	47
5.4	Sketch of the beam paths considered in the model for (a) reflection and (b) transmission geometries. Blue beams represent the second harmonic beams escaping from the sample into air. Red beams represent the fundamental beams.	48

5.5	Typical power dependence of the fs laser beam reflection and transmission through a thin silicon membrane of $32.9 \mu\text{m}$ when irradiated with a fs laser at 800 nm with the contributions of linear absorption ($e^{-\alpha z}$) and free charge carrier absorption (FCA) indicated by arrows; inset: scheme of the experimental setup with an external angle of incidence $\theta = 45^\circ$ and propagation angle $\gamma = 11^\circ$ within silicon.	53
5.6	Temporal evolution of the EFISH signal in native Si/SiO ₂ interfaces of a Si membrane illuminated at peak intensities $> 33 \text{ GW/cm}^2$ (high regime) and $\leq 33 \text{ GW/cm}^2$ (low regime). Solid lines are fit curves using two exponential functions (Eq. (3.5.8) for electron dynamics at low regime and four exponential functions, i.e., two functions as in low regime complemented by two exponential functions for hole dynamics (high regime), represented by Eq. (3.5.9).	55
5.7	Temporal evolution of the EFISH signal in native Si/SiO ₂ interfaces irradiated at various peak intensities. A-G indicate dark periods of 10 s (A), 20 s (B), 30 s (C), 60 s (D), 180 s (E), 360 s (F), and 600 s (G).	55
5.8	Time dependent SH signals from a $33.6 \mu\text{m}$ thick Si membrane measured in reflection, for different incident laser peak intensities at the front SiO ₂ /Si interface, as a function of the irradiation time. The solid lines are fits according to Eq. (3.5.9).	56
5.9	Time dependent SH signals through a $33.6 \mu\text{m}$ thick Si membrane measured in transmission, for different calculated laser peak intensities at the rear Si/SiO ₂ interface, as a function of the irradiation time. The solid lines are fits according to Eq. (3.5.8).	57
5.10	SH traces measured in reflection from a $33.6 \mu\text{m}$ thick Si membrane with interrupted irradiation time of 10 s (A), 20 s (B), 30 s (C), 60 s (D), 180 s (E), 360 s (F) and 600 s (G) with irradiation times of 180 s in between (D), (E), (F) and (G).	58
5.11	SH traces measured in transmission through a $33.6 \mu\text{m}$ thick Si membrane with interrupted irradiation time of 10 s (A), 20 s (B), 30 s (C), 60 s (D), 180 s (E), 360 s (F) and 600 s (G) with irradiation times of 180 s in between (D), (E), (F) and (G).	58
5.12	Time dependent SH signal in transmission from a Si membrane with thickness of $\approx 19.4 \mu\text{m}$	59
5.13	Time dependent SH signal in reflection from a Si membrane with thickness of $\approx 19.4 \mu\text{m}$	60
5.14	Time dependent SH signal in transmission from a Si membrane with thickness of $\approx 28.2 \mu\text{m}$	60
5.15	Time dependent SH signal in reflection from a Si membrane with thickness of $\approx 28.2 \mu\text{m}$	61
5.16	Time dependent SH signal in transmission from a Si membrane with thickness of $\approx 32.3 \mu\text{m}$	61

5.17	Time dependent SH signal in reflection from a Si membrane with thickness of $\approx 32.3 \mu\text{m}$	62
5.18	Saturated SH intensity in transmission, obtained on Si membranes with thicknesses of $28 \mu\text{m}$ and $34 \mu\text{m}$, respectively	62
6.1	Plot of $\ln(P_{\text{trans}}/P_{\text{in}}) - \ln T^2 = -\alpha_1 z_m$ from Eq. (6.1.3) where $I(z = z_m)$ and $I_0 = I(z = 0)$ are the laser beam intensities at the rear and the front sides of the Si membrane as a function of the natural logarithm $\ln(P_{\text{in}})$ of the average laser power P_{in} incident onto the Si membranes.	65
6.2	Square root of the deviation $\Delta I_{\text{FCA}}/\eta$ W of the measured transmission values from the ideal behavior of Beer's law (Eq. (6.1.13)) plotted versus the average laser power P_{in} [W] incident onto the Si membranes.	71
6.3	Fit parameters of the FCA model of Eq. (6.1.11) namely F (squares), E (diamonds), C (filled circles), n (triangles; from Table 6.2) and the slope of Fig. 6.2 (stars) and threshold values of Fig. 6.2 (empty circles) are graphed as a function of the membrane thickness d . . .	72
6.4	Time constants τ_i , $i = 1, 2, 3, 4$ extracted from the numerical fit of the data in Fig. 5.6 using Eq. (3.5.8) and Eq. (3.5.9), respectively.	75
6.5	Time constants τ_i , $i = 1, 2, 3$, for reflection geometry, as a function of the incident intensities at the front Si/SiO ₂ interface.	77
6.6	Time constants τ_i , $i = 1, 2$, for transmission geometry, as a function of the calculated intensities at the back Si/SiO ₂ interface.	79
6.7	Time dependent SH signals measured in transmission at a calculated peak intensity of 4.92 GW/cm^2 , 5.92 GW/cm^2 and in reflection at an incident (behind Si/SiO ₂ interface) peak intensity of 7.25 GW/cm^2 . Solid curves are fits according to Eq. (3.5.8).	82

List of Tables

5.1	Calculated intensities from transmitted and incident powers where $P_{in}, P_{trans}, P_{ref}, I_{in}, I_{ref}, I_{front}, I_{rear}$ and I_{trans} are the incident power, transmitted power, reflected power, the incident intensity, the intensity at the front interface, the intensity at the rear interface and the transmitted intensity, respectively	52
6.1	Parameters ($\alpha_1 z_m$) and thickness d_i of the Si membranes obtained from linear absorption regime (Beer's law, Fig. 5.5, index: lin) and the FCA model (Eqs. 5 and 7) used to fit the measurement point in Fig. 5.2 (with n taken as variable, index: FCA, var) and Fig. 5.3 (with $n = 2$ fixed, index: FCA, fix); d_{mean} is the average and Δd_{SD} is the standard deviation of the 3 values	67
6.2	Fit parameters for the $P_{trans}(P_{in})$ traces in Fig. 5.2 and Fig. 5.3 obtained from Eq. (6.1.12). The parameter values for n are graphed in Fig.6.3	70
6.3	Extracted time constants τ_i from numerical fits of Fig. 5.6 using Eq. 6.2.1	75
6.4	Extracted time constants τ_i from numerical fits of Fig. 5.8 using Eq. (6.2.4)	78
6.5	Extracted time constants τ_1 and τ_2 from numerical fits of Fig. 5.9 using Eq. 3.5.8	80
6.6	Extracted time constants τ_1 and τ_2 from numerical data fit of Fig. 6.7 using Eq. 3.5.8 to compare the TDSH in transmission and in reflection	82

Chapter 1

Introduction

Increasing device integration and miniaturization in modern metal-oxide semiconductor (MOS) technology requires a proper understanding of the structure and particularly the electronic properties of the materials and interfaces. Devices manufactured for microelectronics have structures on the nanometer scale. Surface and interface effects play a significant role in their functionality and reliability via charge carrier dynamics as well as defect related effects.

Silicon (Si) based materials have been of technological importance throughout the years. In particular the silicon/silicon dioxide (Si/SiO₂) interface is used as the gate between the source and drain of most transistors. Today, Si is still a leading material in microelectronics, optoelectronic, micro-mechanics, photovoltaic materials, and increasingly in photonics. The material properties of Si are very important in photonics devices. Si/SiO₂ is a very interesting system in solid state physics as it allows the study of the transition between Si and SiO₂ phases [1]. These properties include high thermal conductivity, high optical damage threshold, high quality and stable oxide [2].

The Si/SiO₂ system has been studied in the domains of materials and condensed matter physics. The main force behind this intense effort is the critical role of the structure in the metal-oxide-semiconductor field effect transistor (MOSFET), which controls the modern age "integrated circuit" technologies [3]. The growing interest in Si/SiO₂ research started just after the invention of the MOSFET by Kahng and Atalla (1960). Since then numbers of articles have been published. Over this time period, MOS circuits have progressed exponentially, with the size of present day transistor below the 1 μm [3]. Regardless the great outgrowing of research and the huge commercial success, there has been little effort to construct a comprehensive, unified microphysical model of the Si/SiO₂ system [3–5]. A good knowledge of the structure and the physics of Si/SiO₂ interface is required to understand its component materials such as the crystalline silicon substrate (Si) and the amorphous silicon dioxide (SiO₂) [3].

Silicon devices can be processed by laser technology with a range of different methods. These methods require a good knowledge of the linear and nonlinear optical phenomena in Si. Some of the nonlinear optical phenomena may occur simultaneously and be difficult to discriminate like coherent two-photon absorption (TPA), free charge carrier absorption (FCA), and thermally induced absorption enhancement (TEA) [6]. FCA has been studied for decades [7] by standard spectroscopy and free charge carrier generation, however with the invention of the laser in 1960, the contactless and well defined photo generation of free charge carriers has become amenable, convenient, and very important. The bulk part of the FCA studies are, however, related to FCA in the wavelength range $\lambda > 0.9 \mu\text{m}$ with small (negligible) interference from the indirect optical transition of Si at $\lambda \leq 1.13 \mu\text{m}$ (1.1 eV optical band gap). Only a few papers address FCA in the spectral overlap region with the indirect and direct optical Si transitions [6, 8–11].

Other methods/techniques have been used to study the optical properties of Si, especially the Si/SiO₂ interface. One laser diagnostic method of high surface and interface selectivity is optical second harmonic generation (SHG), which is a non-destructive, contactless, sensitive diagnostic technique with *in situ* capability for studying the electronic and structural properties of Si/SiO₂ [12–22], MOS [23–25] and metal/Si systems [26–28] which cannot be accessed by conventional electronic probes [12, 13, 17, 29–37].

High repetition rate femtosecond (fs) laser pulses can produce high signal-to-noise ratios, while reducing the sample heating effects. When silicon sample are irradiated with a fs laser pulse trains (800 nm, 75 fs) [13, 18, 19, 38], charging of the sample surface is achieved via internal photoemission (IPE) of electrons from Si to SiO₂. IPE requires the injection of electrons from the Si valence band (VB) to the SiO₂ conduction band (CB) by absorption of at least three photons [38, 39]. Electron transfer across the surface decreases with increasing oxide thickness and vanishes for oxides thicker than 10 nm [19]. In the case of the Si/SiO₂ interface, particularly electric field induced second harmonic (EFISH) processes provide a valuable tool to investigate the mechanisms of charge transfer and trap generation processes in this technologically important system. The photo-induced electric field across the interface changes the nonlinear optical properties of the material interface.

The Laser Research Institute (LRI) at the University of Stellenbosch could, for the first time worldwide detect EFISH signals in transmission through a thin oxidized silicon membrane of about 10 μm thickness [40] with the electric field generated by the laser itself. The EFISH signals obtained in transmission through and reflection from a naturally oxidized Si membrane are compared with identical laser irradiation parameters as shown in Fig. 1.1 (800 nm, 75 fs, 80 MHz, incident average power: 100 mW). The results obtained show that the EFISH signal in transmission geometry is larger and its build-up kinetics

is faster than that obtained in reflection (Fig. 1.2). The results obtained are in contradiction to what one would intuitively expect as the femtosecond (fs) laser beam passes through the Si membrane. The SH harmonic intensity $I^{2\omega} \propto (I^\omega)^2$ and the build-up kinetics of the electric field E_{dc} across the Si/SiO₂ interfaces, are expected to be enhanced by the local laser electric field at the interface [41]. The experimental setup used for the EFISH signal measurements (transmission and reflection) is improved relative to that previously applied to investigate SH generation in "bulk" Si [29, 41].

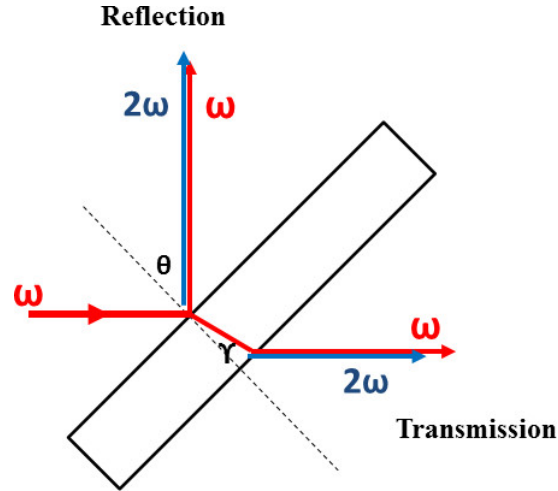


Figure 1.1: Schematic representation of the laser beam reflection from and transmission through a thin silicon membrane at an external incident angle $\theta = 45^\circ$ and the propagation angle inside silicon $\gamma \approx 11^\circ$.

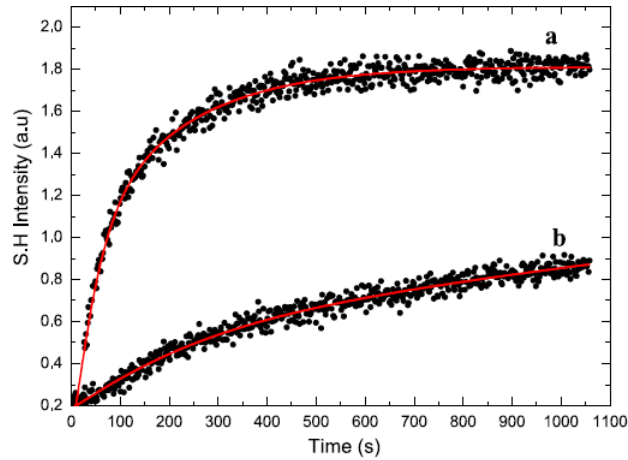


Figure 1.2: EFISH signals obtained by the same incident power (100 mW) recorded in transmission (a) and reflection (b) from a 10 μm thick Si membrane.

In the present work, an investigation of the findings mentioned above will be conducted by implementing an improved experimental setup capable of

simultaneously measuring EFISH signals in reflection and transmission from the same Si membrane. A fs Ti:sapphire laser tuned to $\lambda_{las} = 800$ nm ($h\nu = 1.55$ eV) is applied to investigate the behavior of thin Si membranes in the $10\ \mu\text{m}$ to $30\ \mu\text{m}$ thickness range by measuring the average laser powers of the fs pulse train reflected P_{ref} from and transmitted P_{trans} through the membranes as a function of the average incident power P_{in} (Figs. 5.2, 5.3 and 5.5) as well as measuring simultaneous EFISH signals in transmission and reflection from the same Si membrane.

The obtained results [11] show an unexpected nonlinear behavior of the transmitted laser beam through the Si membranes. The reflected laser powers P_{ref} displays a linear behavior while the transmitted laser power P_{trans} deviates considerably from linearity (Figs. 5.2, 5.3 and 5.5). The transmitted power starts with an initial linear increase, reaches a maximum before decreasing considerably as the input power P_{in} is increased. The nonlinearity observed is attributed to free charge carrier absorption (FCA) in Si. A FCA model is developed and tested [10, 11]

The time-dependent second harmonic (TDSH) signals of the Si membranes are obtained by simultaneously measuring the transmitted through and reflected signals from the Si membranes. The time dependence of the resulting EFISH signal is a measure of the rate of trap site generation and population, both by electrons and holes being pumped across the interface. SHG technique is used to investigate the charge carrier dynamics.

The main experimental findings (FCA) provide an extension of our recent results [10] and address the membrane thickness d , the linear absorption coefficient α_1 , as well as α_{FCA} , absorption coefficient due to free carrier absorption.

This thesis is presented as follows:

Chapter 2 gives a summary of some progress made over the years in the field of second harmonic generation in silicon. Chapter 3 gives a physical background necessary for the concept used in this work, like the formalism of light and matter, the evolution in research involving the Si/SiO₂ interface, the concepts of nonlinear susceptibility tensors, polarization and optical second harmonic generation. Chapters 4 and 5 give the description of the experimental measurements and results obtained, respectively. Discussion of the obtained results is presented in Chapter 6. Summary and conclusion, along with an overview of future work, is given in Chapter 7.

Chapter 2

Research overview

This chapter summarizes few accomplishments in the field of second harmonic generation in silicon (Si) within the past decades.

The silicon/silicon dioxide (Si/SiO₂) interface has been extensively studied due to its technological importance in the micro electronic industries. Different techniques have been used to investigate the Si/SiO₂ structure such as x-ray photoelectron spectroscopy (XPS) [42] for the characterization of ultra thin oxide films, electron spin resonance (ESR) [43, 44], second harmonic generation (SHG) [45], etc.

SHG technique was reported for the first time by Franken and his group ([45]) where they generated SH by focusing a Ruby laser beam into quartz. Few years later (1966), Bloembergen and Shen [46] started theoretical work of SHG with the introduction of gaseous plasma model (free electron gas model), and they went on to apply SHG on silicon surfaces as a probe technique [47] in which the dependence of SHG yield with incident angle from the sample surface was reported in reflection geometry. Two years later they reported SHG in reflection from media with inversion symmetry such as silver [48] and silicon [47].

In 1982 Heinz and Shen demonstrated the sensitivity of submonolayer using SHG to probe monolayers adsorbed to surfaces [49].

Azimuthal rotational anisotropy measurements on Si/SiO₂ interfaces were conducted by Tom et al. [50]. The rotational patterns for different polarization combinations of input and output was used to study Si(100) and Si(111) surfaces. The obtained results from Si(100) and Si(111) indicated differences in surface structural symmetry and exhibited a strong SHG dependence on the angle of rotation. During that period it was shown that rotational anisotropy is sensitive to different phases of surface reconstruction which is caused by different bonding configurations of surface atoms, which produce neighboring dangling bonds. Rotational anisotropy has been applied in different surface and

interface investigations such as vicinal surfaces with steps and terraces [33, 51–53], structure strain [12, 17], microroughness [54–56], chemical modifications of the interface [57–62] and oxide thickness and annealing effect [33, 61, 63, 64]

In the years 1988 - 1989, Shen and Richmond [30, 65] used SHG as a powerful tool to study charge transfer across Si/SiO₂. The spectrum generated with SHG on Si/SiO₂ interface is measured while the incident radiation is changed. A creation of a strong electric field induced second harmonic (EFISH) is captured into the oxide layer. This electric field is caused by charge transfer across the interface. SHG has been proven to be extremely sensitive to a presence of electric fields when an external voltage is applied [66].

Mihaychuk et al. demonstrated for the first time in 1995 that EFISH signal are time dependent in the absence of any external voltage which resulted to say that small interfacial electric field can be established at Si/SiO₂ interface when Si is illuminated with a fs laser pulse trains [18].

In 1997 surface charging and electron trapping in the ultrathin (1.6 μm) SiO₂ films on *n*-type silicon during bombardment by 350 – 600 eV electrons were observed by EFISH generation technique [20]. Four years later, EFISH was reported on semiconductors such as gallium nitride. In these EFISH measurements, the SH signal was observed to increase with the applied voltage. Results show that the application of an external voltage to the crystal breaks the symmetry and SHG can originate from the bulk crystal. In non-centrosymmetric media, the increase in the external bias voltage increases the strength of the third order susceptibility tensor which then increases SH signal generated from the crystal.

Between 2004 and 2008, the effects in time-dependent SH response of native Si/SiO₂ interfaces for peak intensities > 45 GW/cm² was reported by Scheidt et al. Results indicated that hole injection and trapping in the oxide layer contribute to the SH response. An empirical model was developed to extract the characteristic time constants for electron and hole [41]. SH imaging using fs laser pulse (80 fs, 1.59 eV, 80 MHz) was used to spatially investigate the structural homogeneity of zinc oxide ZnO and Pb_{*x*}Cd_{1-*x*}Te ternary alloys (*x* ≈ 2) thin films grown by metal organic chemical vapor deposition (MOCVD)[67–69]. Investigation in the variation of time dependent EFISH signals from bulk boron doped Si(100) of different doping concentrations was also investigated by Scheidt et al [70]. The same year (2008), SH imaging was used to evaluate the quality of thin films manufactured with metal organic chemical vapour deposition (MOCVD) on glass and Si substrates [71]. The results show that SH imaging of the samples is a very useful tool to evaluate the thickness and uniformity of the sample. Being a non-intrusive technique, SH has the capability for an *in-situ* quality control system. SHG as a powerful and sensitive technique was used to study the doping effect in the case of highly boron doped

Si [70, 72–74]

EFISH generation of fs laser pulses ($\lambda = 800$ nm, 75 ± 5 fs, 80 MHz, $E_{pulse} \leq 10$ nJ) is observed for the first time (2011) in transmission through thin free-standing silicon (Si) membrane of $10 \mu\text{m}$ thickness [40]. The results are compared with the well-known EFISH results in reflection.

SHG has also been used to investigate Si waveguides strained by silicon nitride [75]. It is shown that a sizeable second-order nonlinearity at optical wavelengths is induced in a silicon waveguide by using a stressing silicon nitride overlayer. The obtained result suggests that nonlinear strained silicon could provide a competing platform for a new class of integrated light sources spanning the near to mid-infrared spectrum from 1.2 to $10 \mu\text{m}$. An investigation into SHG by Si rich SiN_x thin films deposited by RF sputtering over a wide range of Si concentrations was reported by Akihiro et al [76]. SHG has been used in a hybrid nanostructure with gold gratings embedded in a silicon nitride film [77]. The obtained result shows a strong enhancement of SHG. This enhancement arises from a resonance between the waveguide modes and grating.

In the past few years, studies have been conducted on doping silicon wafers and nanostructures with phosphine oxide monolayers [78], silicon nanoparticles [79], organo-arsenic molecular layers on silicon for high-density doping [80] and complex investigations of multilayer nanostructures of Si/ $\text{SiO}_{1.9}$ have been carried out by probe spectroscopic analysis techniques [81].

SHG has been used to investigate small structures such as silicon nanostructures for photonics and photovoltaics [82, 83]. The study reviews recent progress in silicon nanocrystals, nanowires and photonic crystals as key examples of functional nanostructures. They assessed and highlighted the state-of-the-art in each field and the challenges needed to be overcome to make silicon a truly high performing photonic material.

Optical SH generation and EFISH techniques were recently used to demonstrate different interface properties of molecular beam epitaxial layers grown on Si [84], characterize measurements of amorphous Si interfaces [85] where it was demonstrated that SHG is a sensitive tool for probing strong electric fields present in the 10 nm a-Si:H layer in solar cells. SHG has also been studied as a non-destructive method for the characterization of silicon on insulator wafers [86] in which the quality of film, oxide and interfaces in silicon-on insulator (SOI) wafers was monitored by SHG. SHG has been used to study tunneling holes [87, 88] and probing of dopant type and density at the Si/ SiO_2 interfaces [74]. Nelson et al. [89] reported the development of femtosecond spectral interferometric technique for SHG with time, energy and phase resolution. Using the model systems of passivated GaAs(100) surface and copper

phthalocyanine/GaAs(100) interface, they demonstrated the application of the technique in unveiling the rich dynamics of band renormalization, charge carrier motion and interfacial charge transfer, all induced by across-band gap optical excitation of the semiconductor.

Finally SHG technique is being used to study the interface of Si/SiO₂ of Si membranes [10, 11, 40, 90, 91] by simultaneously measuring the laser transmitted and reflected powers as a function of the incident power as well as EFISH signals generated in transmission and reflection geometries from the same Si membrane. Preliminary results show a nonlinear dependence of the laser transmitted power as the incident laser power is increased, while the reflected laser power show a linear dependence with the incident laser power [11, 91]

Chapter 3

Physical background

In this chapter, the interaction of light with matter will be classically described using Maxwell's equations; the Fresnel's coefficients for two states of polarization at the interface of two media will also be discussed since they (Fresnel's equations) will be used in a developed model to optically estimate the thickness of the silicon membrane sample under investigation. The nonlinear optical interactions of light with matter is given as well as the symmetry properties of the nonlinear susceptibility tensor $\chi^{(2)}$. And finally a quick review on the work done on the electric field induced second harmonic generation is presented

3.1 Electromagnetic waves

3.1.1 Maxwell equations

Maxwell's equations provide a set of four equations describing a complete model of optical propagation phenomena. The Maxwell equations (SI units) are given by:

$$\nabla \cdot \vec{D} = \rho \quad \text{Gauss's law for electric field,} \quad (3.1.1a)$$

$$\nabla \cdot \vec{B} = 0 \quad \text{Gauss's law for magnetic field,} \quad (3.1.1b)$$

$$\nabla \times \vec{E} = -\frac{\partial \vec{B}}{\partial t} \quad \text{Ampere's law,} \quad (3.1.1c)$$

$$\nabla \times \vec{H} = \vec{J} + \frac{\partial \vec{D}}{\partial t} \quad \text{Faraday's law.} \quad (3.1.1d)$$

Here \vec{D} , \vec{B} , \vec{E} and \vec{H} are the dielectric field, the magnetic field, the electric field and the magnetic field intensity, respectively. ρ and \vec{J} represent the volume charge density and the current density vector, respectively. For a given test charge q_0 subject to the electric field \vec{E} , the force experienced by q_0 is given by:

$$\vec{F} = q_0 \vec{E}. \quad (3.1.2)$$

The relationship between \vec{D} , \vec{B} , \vec{E} and \vec{H} is given by:

$$\vec{D} = \varepsilon_0 \vec{E} + \vec{P} = \varepsilon_0 \vec{E} + (\vec{P}^{(1)} + \vec{P}^{NL}) \quad (3.1.3)$$

$$= \varepsilon_0 (1 + \chi^{(1)}) \vec{E} + \vec{P}^{NL} = \varepsilon_0 \varepsilon^{(1)} \vec{E} + \vec{P}^{NL} \quad (3.1.4)$$

$$\vec{B} = \mu_0 \vec{H} + \vec{M}, \quad (3.1.5)$$

where $\varepsilon_0 = (1/36\pi) \times 10^{-9}$ (F/m) and $\mu_0 = 4\pi \times 10^{-7}$ (H m⁻¹) are the permittivity and permeability of free space, respectively. $\vec{P} = \vec{P}^{(1)} + \vec{P}^{NL} = \varepsilon_0 \chi \vec{E} + \vec{P}^{NL}$ is the nonlinear polarization, it characterizes the response of the medium to the incident electric field \vec{E} ; χ is the susceptibility and $\varepsilon^{(1)} = \varepsilon_0 (1 + \chi^{(1)})$ is the frequency dependent first order dielectric tensor, and \vec{M} is the magnetization of the optical medium. In the case where there are no free charge carriers in the medium ($\rho = 0$), the currents are negligible ($\vec{J} = 0$) and where the medium is non-magnetic ($\vec{M} = 0$), Maxwell's equations simplify to:

$$\nabla \cdot \vec{E} = 0, \quad (3.1.6a)$$

$$\nabla \cdot \vec{B} = 0, \quad (3.1.6b)$$

$$\nabla \times \vec{E} = -\frac{\partial \vec{B}}{\partial t}, \quad (3.1.6c)$$

$$\nabla \times \vec{B} = \varepsilon \mu \frac{\partial \vec{E}}{\partial t}. \quad (3.1.6d)$$

Here $\vec{D} = \varepsilon \vec{E}$ (from Eq. 3.1.4) and $\vec{B} = \mu \vec{H}$.

3.1.2 Wave equations

Using Eqs. (3.1.6c) and (3.1.6d) and applying the identity $\nabla \times (\nabla \times \vec{X}) = \nabla (\nabla \cdot \vec{X}) - \nabla^2 \vec{X}$ on Eq. (3.1.6c), where X is a vector, the following equations called *wave equations* are obtained:

$$\nabla^2 \vec{E} - \mu \varepsilon \frac{\partial^2 \vec{E}}{\partial t^2} = 0, \quad (3.1.7a)$$

$$\nabla^2 \vec{B} - \mu \varepsilon \frac{\partial^2 \vec{B}}{\partial t^2} = 0. \quad (3.1.7b)$$

The general form of the wave equation is given by:

$$\nabla^2 f(\vec{r}, t) = \frac{1}{v^2} \frac{\partial^2}{\partial t^2} f(\vec{r}, t), \quad (3.1.8)$$

where v is the phase velocity (or speed) of the wave. The phase velocity is defined as:

$$v = 1/\sqrt{\mu\epsilon}. \quad (3.1.9)$$

In vacuum, the velocity is $c = 1/\sqrt{\mu_0\epsilon_0} = 2.998 \times 10^8$ m/s. For most optical materials $\mu \sim \mu_0$, thus

$$v = \frac{1}{\sqrt{\mu_0\epsilon_0\epsilon_r}} = \frac{c}{n}, \quad (3.1.10)$$

where n is the refractive index. The solution to the wave equation is a simple harmonic wave, which is given by:

$$\vec{E}(\vec{r}, t) = \vec{E}_0 e^{i(\omega t - \vec{k}\vec{r})}, \quad (3.1.11)$$

where \vec{k} is the wave vector and ω is the frequency of the simple harmonic wave. Substituting Eq. (3.1.11) into Eq. (3.1.7a), it is found that:

$$k = \omega\sqrt{\mu\epsilon}. \quad (3.1.12)$$

Eq. (3.1.12) is called the dispersion relation which relates the wave vector \vec{k} to the frequency ω . Substituting the plane wave equation into Eq. (3.1.6a) gives:

$$\nabla \cdot \vec{E} = 0 \quad \Rightarrow \quad \vec{k} \cdot \vec{E} = 0. \quad (3.1.13)$$

Eq. (3.1.13) shows that the electric field is transverse to the direction of propagation (which is also true for \vec{B}). From Eq. (3.1.6d), we have:

$$\nabla \times \vec{E} = -\frac{\partial}{\partial t} \vec{B} \quad \Rightarrow \quad \vec{k} \times \vec{E} = \omega \vec{B}. \quad (3.1.14)$$

Thus \vec{k} , \vec{E} and \vec{B} of the plane wave are perpendicular to each other; and \vec{E} and \vec{B} are in phase. The magnitude of \vec{B} is :

$$|\vec{B}| = \frac{|\vec{k}|}{\omega} |\vec{E}| = \frac{\omega\sqrt{\mu\epsilon}}{\omega} |\vec{E}| = \frac{n}{c} |\vec{E}|. \quad (3.1.15)$$

3.1.3 Polarization

A number of things could happen when a light wave, which travels from a medium with refractive index n_i , strikes an object with a refractive index n_t : the light wave could be absorbed by the object, e.g. the object can fluoresce , i.e. it can absorb light of short wavelength and re-emit it with light of longer wavelength; or it could be reflected by the object or it could also be transmitted through the object as it shown in Fig. 3.1.

3.1.4 States of polarization

Light, which is considered as a plane wave in free space or in an isotropic medium, propagates as a transverse wave where both the electric field, \vec{E} and magnetic field \vec{B} are perpendicular to the wave's direction of propagation, \vec{k} . Both \vec{E} and \vec{B} are oscillating but in different directions. Light as an electromagnetic wave exhibits polarization. Usually, the polarization of light refers to the polarization of the electric field, \vec{E} . Polarization can be linear, circular or elliptical. In the following we consider a linearly polarized light beam. There are two independent states of polarization namely s- and p-polarization

3.1.5 s- Polarisation

For s-polarization, the electric field \vec{E} is perpendicular to the plane of the incident wave as shown in Fig. 3.1. From Eq. (3.1.14), we have: $\vec{B} = (\vec{k}/\omega) \times \vec{E}$.

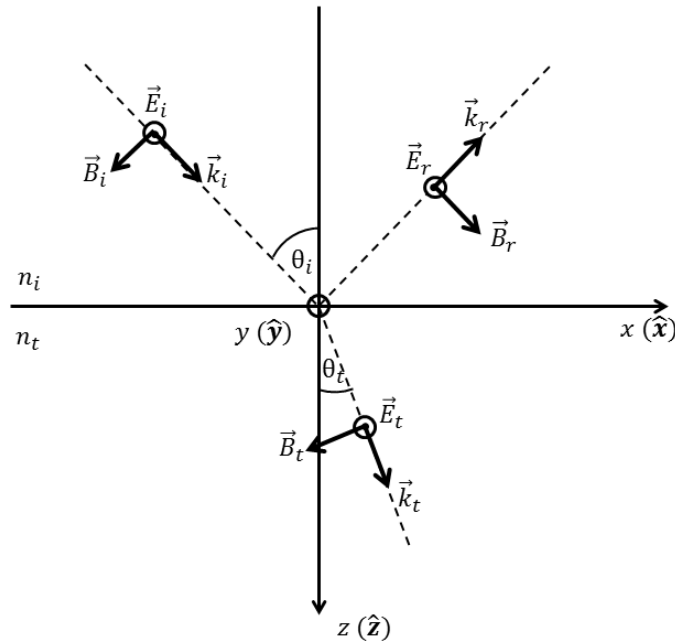


Figure 3.1: Light ray incident on the separation interface of two media with refractive indices n_i and n_t , respectively. The incident electric field is perpendicular to the plane of incidence; θ_i and θ_t are the incident and transmitted angles. i , r and t are subscripts for the incident, reflected and transmitted. \vec{E} , \vec{B} and \vec{k} are the electric, magnetic and wave propagation vectors, respectively.

For the incident wave

$$\vec{E}_i = \hat{y}E_i \exp \left[i(\omega t - \vec{k} \cdot \vec{r}) \right], \quad (3.1.16a)$$

$$\vec{k}_i = \frac{\omega n_i}{c} (\hat{x} \sin \theta_i + \hat{z} \cos \theta_i), \quad (3.1.16b)$$

$$\vec{B}_i = \frac{n_i}{c} (-\hat{x} \cos \theta_i + \hat{z} \sin \theta_i) E_i \exp \left[i(\omega t - \vec{k} \cdot \vec{r}) \right]. \quad (3.1.16c)$$

For the reflected wave:

$$\vec{E}_r = \hat{y}E_r \exp \left[i(\omega t - \vec{k} \cdot \vec{r}) \right], \quad (3.1.17a)$$

$$\vec{k}_r = \frac{\omega n_i}{c} (\hat{x} \sin \theta_i - \hat{z} \cos \theta_i), \quad (3.1.17b)$$

$$\vec{B}_r = \frac{n_i}{c} (\hat{x} \cos \theta_i + \hat{z} \sin \theta_i) E_r \exp \left[i(\omega t - \vec{k} \cdot \vec{r}) \right]. \quad (3.1.17c)$$

For the refracted (or transmitted) wave:

$$\vec{E}_t = \hat{y}E_t \exp \left[i(\omega t - \vec{k} \cdot \vec{r}) \right], \quad (3.1.18a)$$

$$\vec{k}_t = \frac{\omega n_t}{c} (\hat{x} \sin \theta_t + \hat{z} \cos \theta_t), \quad (3.1.18b)$$

$$\vec{B}_t = \frac{n_t}{c} (-\hat{x} \cos \theta_t + \hat{z} \sin \theta_t) E_t \exp \left[i(\omega t - \vec{k} \cdot \vec{r}) \right]. \quad (3.1.18c)$$

Applying the boundary condition (at $\vec{r} = 0$), the normal (\hat{z}) of \vec{B} gives:

$$\frac{n_i}{c} \sin \theta_i (E_i + E_r) = \frac{n_t}{c} \sin \theta_t E_t. \quad (3.1.19)$$

The tangential component (\hat{x}) of $\vec{H} = \frac{1}{\mu} \vec{B}$ gives:

$$\frac{n_i}{\mu_i c} \cos \theta_i (E_i - E_r) = \frac{n_t}{\mu_t c} \cos \theta_t E_t. \quad (3.1.20)$$

Using Snell's law on Eq. (3.1.19), we have $E_i + E_r = E_t$;

$$\frac{n_i}{\mu_i c} \cos \theta_i (E_i - E_r) = \frac{n_t}{\mu_t c} \cos \theta_t (E_i + E_r) \quad (3.1.21)$$

Thus after rearranging Eq. (3.1.21) and by defining $r_s \equiv E_r/E_i$, one would get the following expression:

$$r_s = \frac{\frac{n_i}{\mu_i} \cos \theta_i - \frac{n_t}{\mu_t} \cos \theta_t}{\frac{n_i}{\mu_i} \cos \theta_i + \frac{n_t}{\mu_t} \cos \theta_t}. \quad (3.1.22)$$

Snell's law at the interface of medium with refractive index n_i and medium with refractive index n_t is

$$n_i \sin \theta_i = n_t \sin \theta_t \quad \Rightarrow \quad n_t = n_i \frac{\sin \theta_i}{\sin \theta_t}. \quad (3.1.23)$$

Substituting Eq. (3.1.23) into Eq. (3.1.20) and using $E_i + E_r = E_t$, the following expression could be found:

$$t_s = \frac{2\mu_t \tan \theta_t}{\mu_i \tan \theta_i + \mu_t \tan \theta_t} \quad \text{or} \quad t_s = \frac{\frac{2n_i}{\mu_i} \cos \theta_i}{\frac{n_i}{\mu_i} \cos \theta_i + \frac{n_t}{\mu_t} \cos \theta_t}, \quad (3.1.24)$$

where $t_s \equiv E_t/E_i$.

3.1.6 p-polarization

For p-polarization, the incident electric field \vec{E} is in the incident plane and perpendicular to both the magnetic field \vec{B} and \vec{k} , respectively.

Fig. 3.2 shows a light ray incident at the separation surface of two media with refractive indices n_i and n_t , respectively. Following the same procedure as for s-polarization discussed in section 3.1.5, the following expressions are obtained:

$$r_p = \frac{-\varepsilon_i \tan \theta_i + \varepsilon_t \cos \theta_t}{\varepsilon_i \tan \theta_i + \varepsilon_t \cos \theta_t} = \frac{\frac{n_t}{\mu_t} \cos \theta_i - \frac{n_i}{\mu_i} \cos \theta_t}{\frac{n_t}{\mu_t} \cos \theta_i + \frac{n_i}{\mu_i} \cos \theta_t}, \quad (3.1.25a)$$

$$t_p = \frac{2\varepsilon_i \sin \theta_i}{\cos \theta_t (\varepsilon_i \tan \theta_i + \varepsilon_t \cos \theta_t)} = \frac{\frac{2n_i}{\mu_i} \cos \theta_i}{\frac{n_t}{\mu_t} \cos \theta_i + \frac{n_i}{\mu_i} \cos \theta_t}. \quad (3.1.25b)$$

Here $r_p \equiv E_r/E_i$ and $t_p \equiv E_t/E_i$.

3.2 Light propagation

3.2.1 Fresnel equations

Fresnel equations are equations which determine the reflection and transmission of light incident at the interface between two homogeneous media of different indices [92]. If $r_{s,p}$ and $t_{s,p}$ are defined as the Fresnel coefficients for reflection and transmission, in the state of polarization s or p , respectively; and

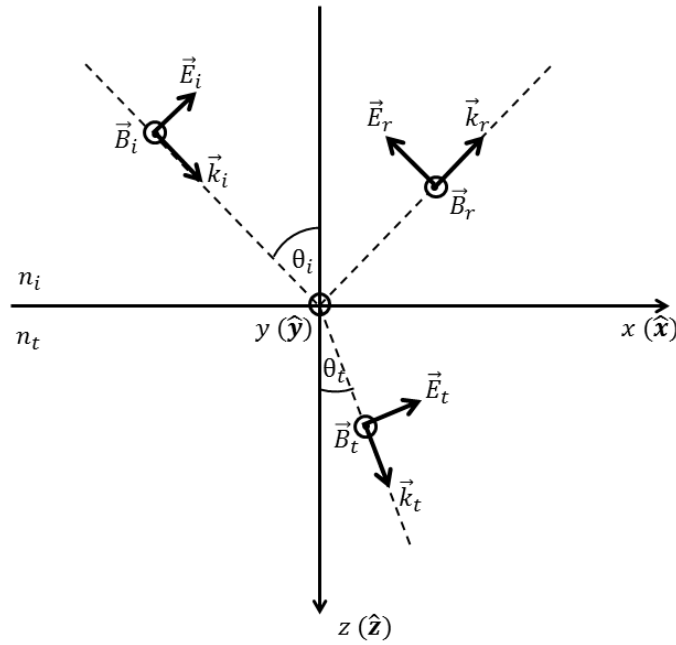


Figure 3.2: Light ray incident on the separation surface of two media with refractive indices n_i and n_t , respectively. The incident electric field is parallel to the plane of incidence; θ_i and θ_t are the incident and transmitted angles, respectively.

if θ_i and θ_t are the incident and refracted (or transmitted) angles, the Fresnel coefficients are given from Eqs. (3.1.22), (3.1.24), (3.1.25a) and (3.1.25b) such as:

$$r_s = \frac{n_i \cos \theta_i - n_t \cos \theta_t}{n_i \cos \theta_i + n_t \cos \theta_t} \quad t_s = \frac{2n_i \cos \theta_i}{n_i \cos \theta_i + n_t \cos \theta_t} \quad (3.2.1a)$$

$$r_p = \frac{n_t \cos \theta_i - n_i \cos \theta_t}{n_i \cos \theta_t + n_t \cos \theta_i} \quad t_p = \frac{2n_i \cos \theta_i}{n_i \cos \theta_t + n_t \cos \theta_i}. \quad (3.2.1b)$$

Here we have taken the case where $\mu_i \sim \mu_t \sim 1$ for most optical media and we have considered that the system is non-magnetic.

From Eqs. (3.2.1a) and (3.2.1b), one can show that $t_s = 1 + r_s$ and $t_p \neq 1 + r_p$. If R and T are the reflectance and transmittance, respectively, the relationship between R and r_j $j = s, p$, where r_j is the amplitude reflection coefficient, is given by [93]:

$$R = |r|^2. \quad (3.2.2)$$

Thus, the reflectance of s-polarized light is:

$$R_s = \left(\frac{n_i \cos \theta_i - n_t \cos \theta_t}{n_i \cos \theta_i + n_t \cos \theta_t} \right)^2, \quad (3.2.3)$$

while the reflectance for p-polarized light is given by:

$$R_p = \left(\frac{n_t \cos \theta_i - n_i \cos \theta_t}{n_i \cos \theta_i + n_t \cos \theta_t} \right)^2. \quad (3.2.4)$$

The transmittance T is not equal to $|t|^2$ because the speed of light in the two media is different. The relationship between the transmittance and the amplitude transmission, t , is given by [93]:

$$T_j = \frac{n_t \cos \theta_t}{n_i \cos \theta_i} |t_j|^2. \quad (3.2.5)$$

Thus, for s-polarized light the transmittance will be:

$$T_s = \frac{n_t \cos \theta_t}{n_i \cos \theta_i} \left(\frac{2n_i \cos \theta_i}{n_i \cos \theta_i + n_t \cos \theta_t} \right)^2, \quad (3.2.6)$$

and for p-polarized light:

$$T_p = \frac{n_t \cos \theta_t}{n_i \cos \theta_i} \left(\frac{2n_i \cos \theta_i}{n_t \cos \theta_i + n_i \cos \theta_t} \right)^2. \quad (3.2.7)$$

From Eqs. (3.2.3), (3.2.4), (3.2.6) and (3.2.7), one can show that $T_s = 1 - R_s$ and $T_p = 1 - R_p$. For the particular case of normal incidence, i.e., $\theta_i = 0$, we have:

$$R_s = R_p = \left(\frac{n_i - n_t}{n_i + n_t} \right)^2, \quad (3.2.8a)$$

$$T_s = T_p = \frac{4n_i n_t}{(n_i + n_t)^2}. \quad (3.2.8b)$$

In this work, it is the reflection and transmission at the air/SiO₂/Si interfaces of a silicon membrane, with refractive index $n = 3.69$ [40], which will be investigated.

3.2.2 Brewster angle

In Eq. (3.2.4), at a specific angle of incidence, the intensity of p-component of the reflected light is zero; and the reflected light becomes linearly polarized

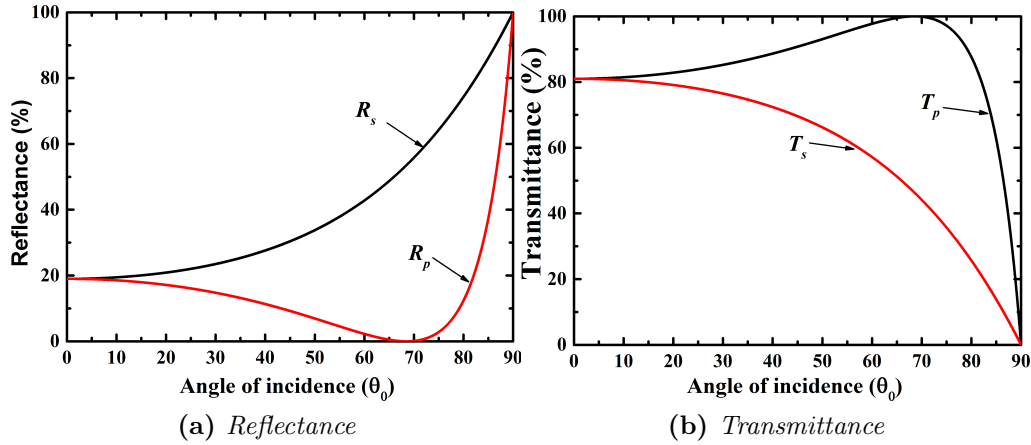


Figure 3.3: Reflectance and transmittance of fundamental light incident on Si with $n_i = 1$ and $n_t = 3.69$

with only the 's' component. This specific angle is called the Brewster angle or the polarization angle. The Brewster angle is given by:

$$\tan \theta_B = \frac{n_t}{n_i}, \quad (3.2.9)$$

where θ_B is the polarization angle (Brewster angle).

Fig. 3.3 shows the theoretical amounts of light which is reflected (Fig. 3.3a) or transmitted (Fig. 3.3b) for both s- and p-polarization for a silicon membrane with refractive index $n = 3.65$. Results from the theoretical model plotted in Fig. 3.3a and Fig. 3.3b show the Brewster angle $\theta_B = 68.6^\circ$.

3.3 Free charge carrier absorption

Free charge carrier absorption (FCA) occurs when a photon is absorbed and an electron or hole is excited in either the conduction or the valence band. Electrons and holes are considered as particles of equal importance, in which electrons and holes carry negative and positive charge, respectively. Holes are the electron voids in the valence band.

In Fig. 3.4, E_c , E_v and E_g are the minimum conduction electron energy, the minimum hole energy and the energy band gap, respectively. Any electron energy above E_c is the electron kinetic energy. A lower location in the valence energy diagram represents a higher hole kinetic energy. The energy band diagram is important for quantitative analysis of semiconductors and devices [94]. The valence band (VB) and the conduction band (CB) are separated by an energy band gap; in Si this band gap is 1.12 eV.

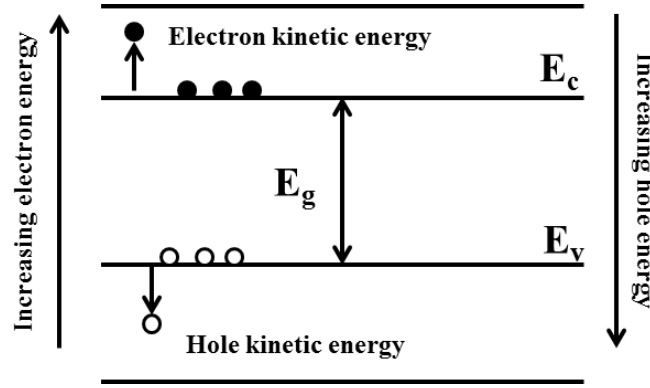


Figure 3.4: Energy band diagram showing electrons and holes. E_c is the minimum conduction electron energy, E_v the minimum hole energy and E_g the energy band gap.

3.3.1 Absorption coefficient

When light travels through a medium, it can be absorbed by that medium. If we assume that the incident intensity on the medium is I_0 , then the transmitted intensity I through that medium can be expressed by

$$I = I_0 e^{-\alpha z_m}, \quad (3.3.1)$$

where α is the absorption coefficient of that particular medium and z_m is the optical path length for a beam of light incident on the medium. The absorption coefficient α is given by [95]

$$\alpha(\lambda) = \frac{4\pi\kappa(\lambda)}{\lambda}, \quad (3.3.2)$$

where κ is the extinction coefficient.

The absorption coefficient determines how far into the material light of a particular wavelength can penetrate before it is absorbed. In a material with a low absorption coefficient, light is poorly absorbed, and if the material is thin enough, it will appear transparent to the wavelength of the incident radiation.

3.4 Nonlinear optical interactions

3.4.1 Optical nonlinear polarization

The optical response of a material to an induced electric field is expressed in terms of the induced polarization, \vec{P} . This response could be linear, for electric field amplitudes $\leq 10^8$ V/cm, or nonlinear, for electric field amplitudes $\geq 10^8$ V/cm [39]. For linear response, the relationship between the induced polarization and the incident electric field is given by:

$$\vec{P}^L = \epsilon_0 \chi^{(1)} \vec{E}. \quad (3.4.1)$$

Here $\chi^{(1)}$ is the well-known linear susceptibility; in this case $\chi^{(1)}$ is a scalar. For nonlinear polarization, the induced polarization is given by:

$$\vec{P}^{NL} = \varepsilon_0 \left(\sum_{jk} \chi_{ijk}^{(2)} \mathbf{E}_j \mathbf{E}_k + \sum_{jkl} \chi_{ijkl}^{(3)} \mathbf{E}_j \mathbf{E}_k \mathbf{E}_l + \dots \right), \quad (3.4.2)$$

where $\chi^{(n)}$ are tensors of rank $n + 1$ and are called the $n - th$ order optical susceptibilities. The general expression of the induced polarization is defined as the sum of the linear and nonlinear polarization and is given by the following expression [96]:

$$\vec{P}_i = \varepsilon_0 \left(\sum_j \chi_{ij}^{(1)} \mathbf{E}_j + \sum_{jk} \chi_{ijk}^{(2)} \mathbf{E}_j \mathbf{E}_k + \sum_{jkl} \chi_{ijkl}^{(3)} \mathbf{E}_j \mathbf{E}_k \mathbf{E}_l + \dots \right). \quad (3.4.3)$$

The dielectric field defined in Eq. (3.1.3) can then be written as the sum of linear and nonlinear contributions as given by:

$$\begin{aligned} \vec{D} &= \varepsilon_0 \vec{E} + \vec{P} = \varepsilon_0 \vec{E} + \vec{P}^L + \vec{P}^{NL} = \varepsilon_0 (1 + \chi^{(1)}) \vec{E} + \vec{P}^{NL} \\ \vec{D} &= \varepsilon_0 \varepsilon^{(1)} \vec{E} + \vec{P}^{NL}. \end{aligned} \quad (3.4.4)$$

$\varepsilon^{(1)} = 1 + \chi^{(1)}$ is the first order dielectric tensor. In the case of isotropic media, $\chi^{(1)}$ is related to the refractive index, n , of the medium by:

$$\varepsilon^{(1)} = 1 + \chi^{(1)} = (n + i\kappa)^2, \quad (3.4.5)$$

in which κ describes the linear absorption and is related to the absorption coefficient α by the equation $\alpha = 2\kappa\omega/c$.

3.4.2 Nonlinear wave equation

Using Eq. (3.4.4), one can show that the wave equation defined in Eq. (3.1.7a) can be written as follows:

$$\nabla^2 \vec{E} - \frac{1}{\varepsilon_0 c^2} \frac{\partial^2}{\partial t^2} \vec{D}^{(1)} = \frac{1}{\varepsilon_0 c^2} \frac{\partial^2}{\partial t^2} \vec{P}^{NL}, \quad (3.4.6)$$

where

$$\vec{D}^{(1)} = \varepsilon_0 \vec{E} + \vec{P}^{(1)} = \varepsilon_0 \varepsilon^{(1)} \vec{E}. \quad (3.4.7)$$

where $\varepsilon^{(1)}$ is a scalar quantity and $\varepsilon_0 = 8.85 \times 10^{-12}$ F/m is the permittivity of free space. Eq. (3.4.6) is the nonlinear wave equation for anisotropic, dispersive and lossless media; it gives the theoretical explanation of the nonlinear optical effects in dielectric media [39].

For the case of isotropic material, the wave equation becomes:

$$\nabla^2 \vec{E} - \frac{\varepsilon^{(1)}}{c^2} \frac{\partial^2}{\partial t^2} \vec{E} = \frac{1}{\varepsilon_0 c^2} \frac{\partial^2}{\partial t^2} \vec{P}^{NL}. \quad (3.4.8)$$

The nonlinear wave equation in Eq. (3.4.8) has the form of a driven (i.e. inhomogeneous) wave equation where the nonlinear response of the medium acts as a source term. In the absence of this term, Eq. (3.4.8) give solutions of the form of free waves propagating with velocity c/n where n is the (linear) index of refraction that satisfy $n^2 = \varepsilon^{(1)}$. For a dispersive medium, the frequency components of the electric field must be considered separately. Thus, the electric field vector, $\vec{E}(\mathbf{r}, t)$, as well as the nonlinear polarization vector, $\vec{P}(\mathbf{r}, t)$ are represented as the sums of their various frequency components ω_n :

$$E(z, t) = \sum_n E_n(\mathbf{r}, t) e^{i(\mathbf{k}_n \mathbf{r} - \omega_n t)} + c.c. \quad (3.4.9)$$

$$P^{NL}(z, t) = \sum_n P_n^{NL}(\mathbf{r}, t) e^{i(\mathbf{k}_n \mathbf{r} - \omega_n t)} + c.c., \quad (3.4.10)$$

where *c.c.* means complex conjugate; k_n and ω_n are the wave vectors and angular frequencies, respectively, and the propagation direction is along the z -axis. The nonlinear wave equation is a second order differential equation; it can be linearized using the so-called slowly varying envelope approximation (SVEA) [97–99]. In the SVEA, the following approximations are applicable for the electric field:

$$\frac{\partial^2}{\partial t^2} E_n \ll \omega_n \frac{\partial}{\partial t} E_n \quad (3.4.11)$$

$$\frac{\partial^2}{\partial z^2} E_n \ll k_n \frac{\partial}{\partial z} E_n. \quad (3.4.12)$$

It is also assumed that the first order derivatives of the envelope functions of the nonlinear polarization are negligible [39], where higher harmonics are considered as carrier waves

$$\frac{\partial^2}{\partial t^2} P_n^{NL} \ll \omega_n \frac{\partial}{\partial t} P_n^{NL} \ll \omega_n^2 P_n^{NL}. \quad (3.4.13)$$

Differentiating Eqs.(3.4.11) and (3.4.12) to a second-order the derivative gives

$$\frac{\partial^2}{\partial t^2} E(z, t) = \left[\frac{\partial^2}{\partial t^2} E_n - 2i\omega_n \frac{\partial}{\partial t} E_n - \omega_n^2 E_n \right] e^{i(k_n z - \omega t)} \quad (3.4.14)$$

$$\frac{\partial^2}{\partial z^2} E(z, t) = \left[\frac{\partial^2}{\partial z^2} E_n - 2ik_n \frac{\partial}{\partial z} E_n - k_n^2 E_n \right] e^{i(k_n z - \omega t)} \quad (3.4.15)$$

$$\frac{\partial^2}{\partial t^2} P^{NL}(z, t) = \left[\frac{\partial^2}{\partial t^2} P_n^{NL} - 2i\omega_n \frac{\partial}{\partial t} P_n^{NL} - \omega_n^2 E_n \right] e^{i(k_n z - \omega t)}. \quad (3.4.16)$$

Substituting Eqs. (3.4.14), (3.4.15) and (3.4.16) and taking into account the SVEA, the nonlinear Eq.(3.4.8) becomes

$$\left(\frac{\partial}{\partial z} - \frac{\omega_n \varepsilon^{(1)}}{k_n c^2} \frac{\partial}{\partial t} \right) E_n(z, t) + \frac{1}{2ik_n} \left(k_n^2 - \omega_n^2 \frac{\varepsilon^{(1)}}{c^2} \right) E_n(z, t) = \frac{i\omega_n^2}{2\varepsilon_0 c^2} P_n^{NL}(z, t). \quad (3.4.17)$$

To get a converging solution to Eq. (3.4.17), the dispersion condition must be satisfied:

$$k_n^2 - \omega_n^2 \frac{\varepsilon^{(1)}}{c^2} = 0 \quad \Rightarrow \quad k_n = \omega_n \frac{n_{\omega_n}}{c}, \quad (3.4.18)$$

where $n_{\omega_n} = \sqrt{\varepsilon^{(1)}}$.

In the SVEA, the nonlinear wave equation of Eq.(3.4.8) is then simplified to:

$$\left(\frac{\partial}{\partial z} - \frac{n_{\omega_n}}{c} \frac{\partial}{\partial t} \right) E_n(z, t) = \frac{i\omega_n}{2\varepsilon_0 n_{\omega_n} c} P_n^{NL}(z, t). \quad (3.4.19)$$

Equation (3.4.19) is the linearized form of the wave equation (Eq.(3.4.8)) and with the SVEA represents the electric field in the medium due to the induced nonlinear polarization.

3.4.3 Optical second harmonic generation (SHG)

Optical second harmonic generation (SHG) is a nonlinear conversion of two photons of frequency ω to a single photon of frequency 2ω which, in the dipole moment approximation, interacts with a noncentrosymmetric medium [36]. The optical second harmonic is used as method for probing buried interfaces that cannot be accessed by conventional electronic techniques. In 1968, Bloembergen et al [47] showed that second harmonic signals could be generated from the surface of centrosymmetric materials. It is the second term of Eq. (3.4.3) responsible for the SHG in a material. The second harmonic polarization is given by:

$$P_i^{(2)}(t) = \varepsilon_0 \left(\sum_{jk} \chi_{ijk}^{(2)} E_j(t) E_k(t) \right) \quad (3.4.20)$$

χ is a proportionality constant called second-order nonlinear susceptibility. It is a tensor of rank three and consists of 27 Cartesian components. $P_i^{(2)}$ with $i = x, y, z$ is the i^{th} component of the second-order polarization; $E(t)$ is the optical electric field. In the incident field with frequency ω is given such as:

$$E_i = \varepsilon_i \exp(-i\omega t) + c.c., \quad (3.4.21)$$

where ε_i is the field amplitude at a given position and *c.c.* means complex conjugate. The second-order nonlinear polarization can easily be found to be

$$P_i^{(2)}(t) = \varepsilon_0 \left(\sum_{jk} \chi_{ijk}^{(2)} (\varepsilon_i \varepsilon_j \exp(-i2\omega t) + \varepsilon_i^* \varepsilon_j^* \exp(i2\omega t) + \varepsilon_i \varepsilon_j^* + \varepsilon_i^* \varepsilon_j) \right). \quad (3.4.22)$$

This equation contains a component that radiates at twice the frequency of the incident field. It also contains a dc component at zero frequency, an effect known as optical rectification [96, 100]. A symmetry aspect of Eq. (3.4.22) shows that all even-order coefficients in the dipole approximation are forbidden in the bulk of a centrosymmetric medium [34, 51, 101], i.e., the operation $\vec{r} \rightarrow -\vec{r}$ leaves the inversion symmetry media unaffected, but does add minus signs to both $\vec{P} \rightarrow -\vec{P}$ and $\vec{E} \rightarrow -\vec{E}$. This is only possible when $\chi^{(n)} = 0$ for even n [102]. SHG exhibits a degree of surface sensitivity for centrosymmetric media [103, 104]. This would mean that no SHG is allowed in a centrosymmetric medium. However, at the interface between two different bulk media, where inversion symmetry is no longer conserved, $\chi^{(2)}$ is not necessarily zero. Thus, SHG from interfaces of membranes is allowed.

3.4.4 Symmetry properties of the second-order susceptibility tensor $\chi^{(2)}$

If the electric field $\tilde{E}(\mathbf{r}, t)$ can be expressed by a sum of discrete frequency components $\mathbf{E}(\omega_n)$ such as

$$\tilde{\mathbf{E}}(\mathbf{r}, t) = \sum_n \mathbf{E}(\omega_n) e^{-i\omega_n t} + c.c., \quad (3.4.23)$$

then the component of the second-order nonlinear susceptibility tensor can be defined as [105]:

$$P_i^{(2)}(\omega_n + \omega_m) = \varepsilon_0 \sum_{jk} \sum_{(nm)} \chi_{ijk}^{(2)}(\omega_n + \omega_m) E_j(\omega_n) E_k(\omega_m). \quad (3.4.24)$$

i, j, k refer to the Cartesian coordinates, and the notation (nm) indicates that the sum over n and m is to be made with the sum $\omega_n + \omega_m$ held constant. For the complete description of the nonlinear susceptibility tensor of Eq. (3.4.24), one would need to know all the 324 complex numbers which account for all permutations of the Cartesian coordinates and of all the frequency components for both positive and negative frequencies [105]. This number is reduced to a number of independent components by symmetry properties of the nonlinear susceptibility. The symmetry properties of the second-order susceptibility are the reality of fields, the intrinsic permutation symmetry, the reality of the nonlinear susceptibility tensor, the full permutation symmetry, the inversion symmetry and the Kleinman symmetry. Those symmetry properties preserve the numerical value of $\chi^{(2)}$. The following properties are the symmetry properties of nonlinear optical susceptibility tensors [105]:

Reality of fields

This symmetry property changes the sign of all frequency components and take the complex conjugate.

$$\chi_{ijk}^{(2)}(-\omega_n - \omega_m, -\omega_n, -\omega_m) = \chi_{ijk}^{(2)}(\omega_n + \omega_m, \omega_n, \omega_m)^* \quad (3.4.25)$$

Intrinsic permutation symmetry

It simultaneously interchanges the last two frequency components and the last two Cartesian coordinates.

$$\chi_{ijk}^{(2)}(\omega_n + \omega_m, \omega_n, \omega_m) = \chi_{ikj}^{(2)}(\omega_n + \omega_m, \omega_m, \omega_n) \quad (3.4.26)$$

Reality of the nonlinear susceptibility tensor

For a lossless medium, it takes the complex conjugate.

$$\chi_{ijk}^{(2)}(\omega_n + \omega_m, \omega_n, \omega_m) = \chi_{ijk}^{(2)}(\omega_n + \omega_m, \omega_n, \omega_m)^* \quad (3.4.27)$$

Full permutation symmetry

For a lossless medium, this symmetry property simultaneously interchanges any frequency components and the corresponding Cartesian coordinates

$$\chi_{ijk}^{(2)}(\omega_n + \omega_m, \omega_m, \omega_n) = \chi_{jki}^{(2)}(\omega_m - \omega_n, \omega_m, -\omega_n). \quad (3.4.28)$$

Inversion symmetry

In a centrosymmetric medium, all values of the second-order susceptibility are zero.

$$\chi_{ijk}^{(2)}(\omega_n + \omega_m, \omega_m, \omega_n) = 0 \quad (3.4.29)$$

Kleinman's symmetry

In this symmetry property, $\chi^{(2)}$ is independent of frequency and the medium is lossless. The symmetry interchanges the Cartesian coordinates without interchanging the frequency components.

$$\begin{aligned}\chi_{ijk}^{(2)}(\omega_n + \omega_m, \omega_m, \omega_n) &= \chi_{jki}^{(2)}(\omega_n + \omega_m, \omega_m, \omega_n) = \chi_{kij}^{(2)}(\omega_n + \omega_m, \omega_m, \omega_n) \\ &= \chi_{ikj}^{(2)}(\omega_n + \omega_m, \omega_m, \omega_n) = \chi_{jik}^{(2)}(\omega_n + \omega_m, \omega_m, \omega_n) \\ &= \chi_{kji}^{(2)}(\omega_n + \omega_m, \omega_m, \omega_n)\end{aligned}\quad (3.4.30)$$

3.4.5 Contracted notation

When the validity of Kleinman's symmetry condition is valid, a contracted notation for the second-order nonlinear susceptibility is introduced by defining a tensor as

$$d_{ijk} = \frac{1}{2}\chi_{ijk}^{(2)} \quad (3.4.31)$$

Under Kleinman's symmetry conditions, in general for second harmonic generation, the tensor d_{ijk} is symmetric in its last two indices. Therefore, a contracted matrix d_{il} is introduced according to the prescription

$$\begin{array}{l}jk: \quad 11 \quad 22 \quad 33 \quad 23,32 \quad 31,13 \quad 12,21 \\ l: \quad 1 \quad 2 \quad 3 \quad 4 \quad 5 \quad 6.\end{array}$$

The second-order nonlinear polarization can then be written as

$$P_i^{(2)} = \varepsilon_0 \sum_{jk} \sum_{(nm)} 2d_{il} E_j(\omega_n) E_k(\omega_m). \quad (3.4.32)$$

The nonlinear susceptibility tensor can then be represented, in terms of d_{il} , as 3×6 matrix in the following form

$$d_{il} = \begin{bmatrix} d_{11} & d_{12} & d_{13} & d_{14} & d_{15} & d_{16} \\ d_{21} & d_{22} & d_{23} & d_{24} & d_{25} & d_{26} \\ d_{31} & d_{32} & d_{33} & d_{34} & d_{35} & d_{36} \end{bmatrix}. \quad (3.4.33)$$

When the Kleinman symmetry condition is valid, only 10 of these elements are independent and the matrix takes the following form

$$d_{il} = \begin{bmatrix} d_{11} & d_{12} & d_{13} & d_{14} & d_{15} & d_{16} \\ d_{16} & d_{22} & d_{23} & d_{24} & d_{14} & d_{12} \\ d_{15} & d_{24} & d_{33} & d_{23} & d_{13} & d_{14} \end{bmatrix}. \quad (3.4.34)$$

The induced nonlinear polarization leading to SHG, in terms of d_{il} is given by

$$\begin{bmatrix} P_x(2\omega) \\ P_y(2\omega) \\ P_z(2\omega) \end{bmatrix} = 2\varepsilon_0 \begin{bmatrix} d_{11} & d_{12} & d_{13} & d_{14} & d_{15} & d_{16} \\ d_{21} & d_{22} & d_{23} & d_{24} & d_{25} & d_{26} \\ d_{31} & d_{32} & d_{33} & d_{34} & d_{35} & d_{36} \end{bmatrix} \begin{bmatrix} E_x^2(\omega) \\ E_y^2(\omega) \\ E_z^2(\omega) \\ 2E_y(\omega)E_z(\omega) \\ 2E_x(\omega)E_z(\omega) \\ 2E_x(\omega)E_y(\omega) \end{bmatrix} \quad (3.4.35)$$

Sipe et al. [29] did a phenomenological study of the theory of optical second- and third-harmonic generation. In their study they showed that for cubic centrosymmetric crystals Eq. (3.4.35) takes different forms for different crystal faces; i.e. for crystals with a (111) face Eq. (3.4.35) becomes [29]:

$$\begin{bmatrix} P_x(2\omega) \\ P_y(2\omega) \\ P_z(2\omega) \end{bmatrix} = 2\varepsilon_0 \begin{bmatrix} d_{11} & -d_{11} & 0 & 0 & d_{15} & 0 \\ 0 & 0 & 0 & d_{15} & 0 & -d_{11} \\ d_{31} & d_{31} & d_{33} & 0 & 0 & 0 \end{bmatrix} \begin{bmatrix} E_x^2(\omega) \\ E_y^2(\omega) \\ E_z^2(\omega) \\ 2E_y(\omega)E_z(\omega) \\ 2E_x(\omega)E_z(\omega) \\ 2E_x(\omega)E_y(\omega) \end{bmatrix}. \quad (3.4.36)$$

The components of the induced nonlinear polarization are:

$$P_x(2\omega) = 2\varepsilon_0 (d_{11}E_x^2(\omega) - d_{11}E_y^2(\omega) + 2d_{15}E_x(\omega)E_z(\omega)) \quad (3.4.37a)$$

$$P_y(2\omega) = 2\varepsilon_0 (2d_{15}E_y(\omega)E_z(\omega) - 2d_{11}E_x(\omega)E_y(\omega)) \quad (3.4.37b)$$

$$P_z(2\omega) = 2\varepsilon_0 (d_{13}E_x^2(\omega) + d_{13}E_y^2(\omega) + d_{33}E_z^2(\omega)). \quad (3.4.37c)$$

For the Si(100) face, Eq. (3.4.35) can be written as [106]

$$\begin{bmatrix} P_x(2\omega) \\ P_y(2\omega) \\ P_z(2\omega) \end{bmatrix} = 2\varepsilon_0 \begin{bmatrix} 0 & 0 & 0 & 0 & d_{15} & 0 \\ 0 & 0 & 0 & d_{15} & 0 & 0 \\ d_{31} & d_{31} & d_{33} & 0 & 0 & 0 \end{bmatrix} \begin{bmatrix} E_x^2(\omega) \\ E_y^2(\omega) \\ E_z^2(\omega) \\ 2E_y(\omega)E_z(\omega) \\ 2E_x(\omega)E_z(\omega) \\ 2E_x(\omega)E_y(\omega) \end{bmatrix}. \quad (3.4.38)$$

In this case, the induced nonlinear polarization components are:

$$P_x(2\omega) = 4\varepsilon_0 d_{15} E_x(\omega) E_z(\omega) \quad (3.4.39a)$$

$$P_y(2\omega) = 4\varepsilon_0 d_{15} E_y(\omega) E_z(\omega) \quad (3.4.39b)$$

$$P_z(2\omega) = 2\varepsilon_0 (d_{31}E_x^2(\omega) + d_{31}E_y^2(\omega) + d_{33}E_z^2(\omega)). \quad (3.4.39c)$$

If the incident electric field is p-polarized, i.e. $E_x = 0$, E_y and E_z are non-zero the components of the polarization of Eq. (3.4.39) become:

$$P_x(2\omega) = 0 \quad (3.4.40a)$$

$$P_y(2\omega) = 4\varepsilon_0 d_{15} E_y(\omega) E_z(\omega) \quad (3.4.40b)$$

$$P_z(2\omega) = 2\varepsilon_0 (d_{31} E_y^2(\omega) + d_{33} E_z^2(\omega)). \quad (3.4.40c)$$

For s-polarized light, incident on the yz -plane, $E_y(\omega) = E_z(\omega) = 0$ and $E_x(\omega) \neq 0$, the induced second-order nonlinear polarization is in the z -direction and is given by

$$P_z(2\omega) = 2\varepsilon_0 d_{31} E_x^2(\omega). \quad (3.4.41)$$

The generated SH beam does not have s-polarization since there is no x -component of the induced polarization.

3.4.6 Multiphoton absorption

Multiphoton processes are interactions of electromagnetic radiation with matter that are accompanied by the absorption and emission of several electromagnetic quanta (photons) in an elementary event. Multiphoton absorption effects are very important since they can initiate processes that linear absorption cannot at a photon energy below the direct band gap¹. With the development of lasers, especially the femtosecond laser, it has become clear that electromagnetic radiation interacts with matter where processes involving more than one photon can occur [107]. One such interaction is two-photon absorption (TPA). There are many techniques used to study TPA; one way of measuring TPA in semiconductors is to measure the attenuation of a beam or pulse propagating through a medium. If the pulse irradiance is I , the pulse is attenuated according to the expression [107–109]

$$\frac{dI}{dz} = -\alpha I - \beta I^2 - \gamma I^3 - \tau I^4 - \dots, \quad (3.4.42)$$

where α , β , γ and τ are the linear, two-photon, three-photon and four-photon absorption coefficients, respectively. For linear and two-photon absorption, the attenuation of the laser beam is given by:

$$\frac{dI}{dz} = -\alpha I - \beta I^2. \quad (3.4.43)$$

¹Semiconductor: when the valence band maximum (VBM) and the conduction band maximum (CBM) are situated in the same direction of the Brillouin zone, the band gap is direct. Otherwise, when those points are situated in different symmetry directions, there is an indirect band gap.

When multiple reflections are neglected within the medium, the transmitted irradiance is given by the expression [107]

$$I(z, l, t) = \frac{\alpha (1 - R)^2 I(z, 0, t) e^{-\alpha l}}{1 + \beta (1 - R) I(z, 0, t) (1 - e^{-\alpha l})}. \quad (3.4.44)$$

Here l is the thickness and R is the reflectivity of the medium. If $\beta = 0$, Eq. (3.4.44) reduces to the well-known Beer-Lambert's law of a single photon absorption. A z-scan technique at different wavelengths λ has been used by several groups to obtain the two-photon absorption coefficient $\beta(\lambda)$ and the Kerr nonlinearity $n_2(\lambda)$ [110–126].

3.4.7 The z-scan technique

The z-scan technique is a method used to measure the nonlinear index and the nonlinear absorption coefficient. It can be performed in two different ways: in an open and close aperture. In a z-scan technique, a sample with thickness d is moved along the focus of a beam with a Gaussian spatial profile, and the transmission through an aperture behind is measured as a function of the longitudinal coordinate z . The open aperture technique is designed to detect all light transmitted through the sample by placing no aperture in front of the photodiode (detector), and consequently the nonlinear absorption coefficient can be obtained. For a Gaussian beam profile, the transmitted light for a z-scan in the open aperture technique is given by [127, 128]:

$$T_{open}(z) = 1 - \frac{1}{2\sqrt{2}} \frac{\beta I_0 l_{eff}}{1 + x^2}, \quad (3.4.45)$$

where $x = z/z_0$, $z_0 = k\omega^2$ is the confocal parameter, with $k = 2\pi/\lambda$ the free space wave vector, ω is the $1/e$ intensity beam waist, I_0 is the peak on-axis intensity, $l_{eff} = \alpha^{-1} (1 - e^{-\alpha l})$ is the effective optical length and α is the linear absorption coefficient. For silicon (Si), α is nonzero for $\lambda < 1100$ nm [129].

In a closed aperture z-scan (aperture transmission $S < 1$), a small aperture is placed at a distance z in front of the photodiode so that only the central part of the transmitted light through the aperture is detected as the sample is scanned along the z -axis providing the nonlinear refractive coefficient. Due to the nonlinear focusing of the beam, the transmission of the aperture displays a characteristic peak-valley shape, which under the approximation of small refractive index and absorption changes depends on the coordinate z as [130, 131]

$$T_{closed}(z) \cong 1 - \frac{4x \langle \Delta \Phi_0 \rangle}{(1 + x^2)(9 + x^2)}. \quad (3.4.46)$$

The time-averaged peak on-axis phase change $\langle \Delta \Phi_0 \rangle$ (at the center of the Gaussian profile) is a function of the nonlinear refractive index n_2 and the aperture transmission S can be approximated as

$$\langle \Delta \Phi_0 \rangle \cong \frac{1}{\sqrt{2}} (1 - S)^{0.25} k l_{eff} n_2 I_0. \quad (3.4.47)$$

3.4.8 Multiphoton absorption in silicon/silicon dioxide system

In metal-oxide-semiconductor (MOS) devices silicon-silicon dioxide (Si/SiO₂) is the most investigated interface between two solid materials [12]. In the past decades optical second harmonic generation (SHG) has been used as a powerful tool to probe the electronic and structural properties of solid-solid interfaces for media with inversion symmetry [4, 47, 100, 132–137]; but many studies using the SHG technique have been directed at surfaces of centrosymmetric media such as silicon (Si) for which the bulk second-order susceptibility vanishes under the dipole approximation [24, 34, 36, 100–102, 138–140]. The Si/SiO₂ interfaces have been studied in an extensive manner and significant progress has been made in understanding the sensitivity of SHG to interface defects, steps, strain, roughness, electric fields, carrier dynamics and chemical modifications [25, 36, 40, 41, 141, 142]. It has been shown that under femtosecond (fs) laser irradiation, the optical properties of silicon can change drastically and the probability of a material absorbing more than one photon before relaxing to the ground state can be enhanced [143]. Ragghunathan et al. [144] showed that multiphoton absorption is strong in the mid- or far-infrared regions, where two or three photons are simultaneously absorbed through virtual intermediate state(s) in the indirect energy gap of 1.1 eV. When irradiating the Si/SiO₂ interface with a fundamental wavelength at frequency ω (with photon energy 1.55 eV), multiphoton absorption can lead to internal photoemission (IPE) of electrons from Si to SiO₂ and external photon emission from Si to vacuum. Internal photon emission can result in a separation of charges which produces an internal electric field response due to the increase in the electric field in Si near the Si/SiO₂ interface; that internal electric field causes electric field induced second harmonic (EFISH).

3.5 Electric field induced second harmonic (EFISH) generation

Optical second harmonic generation (SHG) is a noninvasive probe technique which has been used advantageously to investigate surfaces and interfaces of systems with broken inversion symmetry [4, 12, 13, 17–19, 24, 34, 37, 145, 146] such as the Si surface and the Si/SiO₂ interface. Electric field induced second harmonic (EFISH) generation [18, 19, 34, 38, 41, 147] is a well-established technique to determine the second- and third-order nonlinear optical response from centrosymmetric materials such as silicon (Si) [148].

3.5.1 Sources for second harmonic generation

There are two sources of SHG in the electric dipole approximation; in the absence of an electric field, SHG in centrosymmetric media such as silicon (Si) and amorphous SiO₂ is due to surface electric dipole and bulk quadrupole contributions [29, 38]. The surface polarization density at the second frequency is

$$P_{SD,i}^{(2\omega)} = \varepsilon \sum_{jk} \chi_{ijk}^{(2),S} E_j^\omega E_k^\omega, \quad (3.5.1)$$

while the bulk-quadrupole polarization can be written as

$$P_{BQ}^{(2\omega)} = \varepsilon \sum_{ijkl} \Gamma_{ijkl} E_j^\omega \nabla_k E_l^\omega, \quad (3.5.2)$$

where $\chi_{ijk}^{(2),S}$ is the surface dipole susceptibility tensor, Γ_{ijkl} the bulk-quadrupole susceptibility tensor and E_j^ω the fundamental beam electric field.

When a dc electric field is present there is also a bulk-dipole polarization density which is described by the nonlinear polarization [19, 23, 25, 34, 39, 148]

$$P_{BD,i}^{(2\omega)} = \varepsilon \sum_{ijkl} \chi_{ijkl}^{(3)} E_j^\omega E_k^\omega E_l^{dc}, \quad (3.5.3)$$

where $\chi_{ijkl}^{(3)}$ are the components of the bulk-dipole allowed third-order nonlinear susceptibility tensor, $E_{j,k}^\omega$ are the fundamental optical fields and E_l^{dc} the local dc electric field. $|\chi^{(3)}|$ is $10^4 \times$ smaller in SiO₂ than in Si; EFISH from Si/SiO₂ is dominated by the near-interface electric field in Si [38].

3.5.2 Time-dependent second harmonic generation

The time-dependent second harmonic (TDSH) was observed by Mihaychuk and colleagues [38]. They showed that the increase in second harmonic (SH) signals is attributed to the laser injection of hot electrons into the oxide conduction band and subsequent charge trapping [20, 149]. The charge carriers cause an internal dc electric field, which affects the optical nonlinear susceptibility .

When an electric field is present in the region of excitation, the electric field can directly contribute to the generated SH signal [150]. The generated SH intensity, $I^{(2\omega)}$ can be expressed by [22, 41, 70, 145, 150, 151]

$$I^{(2\omega)}(t) = \left| \chi_0^{(2)} + \chi^{(3)} E^{dc}(t) \right|^2 (I^{(\omega)})^2 \quad (3.5.4)$$

$$= \left| \chi_{eff}^{(2)}(t) \right|^2 (I^{(\omega)})^2, \quad (3.5.5)$$

where $I^{(\omega)}$ is the intensity of the incident laser light, $E^{dc}(t)$ the internal electric field at the interface, $\chi_0^{(2)}$ and $\chi^{(3)}$ the interfacial second- and third-order susceptibilities, respectively, and $\chi_{eff}^{(2)}(t) = \chi_0^{(2)} + \chi^{(3)}E^{dc}(t)$ is the effective photo induced second-order optical susceptibility. The temporal evolution of EFISH intensity $I^{(2\omega)}$ reflects the dynamics of the charge separation processes and is a direct measure for the transient interfacial charge density n_c [19, 22, 38, 151]

$$n_c \propto \left| \chi_{eff}^{(2)} \right| \propto \sqrt{I^{(2\omega)}}, \quad (3.5.6)$$

with $\chi_{eff}^{(2)}$ being the effective internal field dependent interfacial second-order susceptibility, which depends on the internal dc electric field [22, 152].

Fig. 3.5 shows a schematic energy diagram of a non-irradiated SiO_2 interface [38]. Bloch and his group showed that from the intensity dependence of the charging time, internal photoemission (IPE) involves excitation of electrons from the Si valence band (VB) to the oxide conduction band (CB) [19].

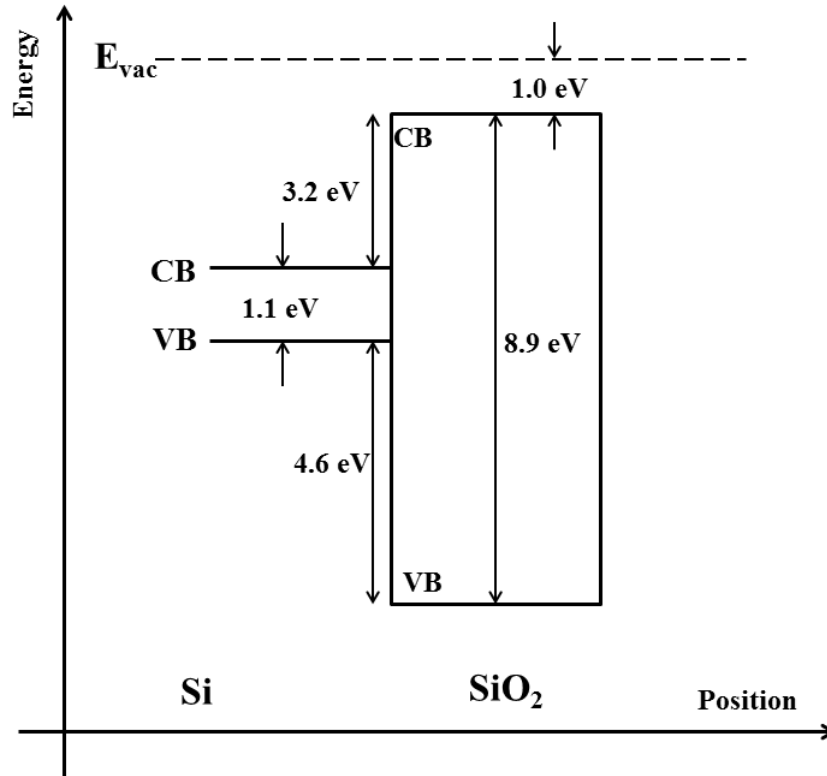


Figure 3.5: Energy levels in Si/SiO_2 for intrinsic and weakly doped silicon: CB, conduction band; VB, valence band; E_{vac} , vacuum energy level.

Under illumination with femtosecond laser there is generation of new electron trap sites. Ambient oxygen enhances charge-carrier trapping at the Si/SiO_2 interface [19, 153]. Charge trapping occurs also under vacuum conditions [38].

The injection of electrons as well as holes and the trapping processes in Si/SiO₂ contribute to the time-dependent SHG signals observed [38, 40, 41, 154]. Injection and trapping as well as trap generation can be divided into two steps [41]:

- (i) The photo excitation of electrons and holes in silicon due to multiphoton processes at high peak intensities; this excitation is independent of the oxide since SiO₂ is transparent in the near infrared spectral region and multiphoton processes are negligible for its large band gap of 7.3 eV.
- (ii) The injection, transport and trapping of charge carriers as well as the trap site generation in the oxide.

Figs. 3.6 and 3.7 are schematic energy band diagrams of the Si/SiO₂ interface of a Si when irradiated with laser pulses at low and high peak intensities, respectively. In bulk silicon, hot electrons can be generated by three-photon processes (red arrows in Figs. 3.6 and 3.7). The electron injection into the SiO₂ layer takes place because, with three-photon absorption processes, electrons have enough energy to overcome the band gap offset of 4.3 eV between the Si valence and SiO₂ conduction bands [38]. When the incident wavelength is in two-photon resonance with the interband transitions of the near interface or bulk silicon, efficient electron-hole (eh) pair creation takes place and a resonantly enhanced electron injection process is observed by SHG [12, 17, 25]. Electron trapping occurs at the SiO₂/air interface (A) [19], in the bulk SiO₂ (B) and at the Si/SiO₂ interface (C) [38]. The resultant charge separation leads to an interfacial electric field E_{int} (blue arrow in Fig. 3.6) formed by both electrons and holes being pumped across the Si/SiO₂ interface. The interfacial electric field E_{int} exceeds 10 V/cm in ultrathin oxides for surface charge densities $> 10^{12} \text{ cm}^{-2}$, which are realistic for intensities employed here [38]. This is sufficient to yield measurable electric field induced changes in the observed SH signal [18, 19, 34, 153].

The energy barrier required for hole injection from the Si conduction band to the SiO₂ valence band is 5.7 eV (Fig. 3.5) [38]. In order to inject holes from Si to SiO₂, it requires a four-photon excitation process.

For a given high peak intensity, the contribution of electron effects is dominant in building up the interfacial electric field (E_{el} in Fig. 3.7) while the contribution of holes to the interfacial electric field (E_h in Fig. 3.7) is delayed (relative to the electron injection). This delay is due to the less efficient four-photon excitation and low hole mobility. As a result, the SH signal representing the transient net charge density is a superposition of electrons and holes at the interface.

A generalized empirical model involving the dynamics of electrons and holes was developed [18, 38, 41] to extract the amplitudes as well as the time con-

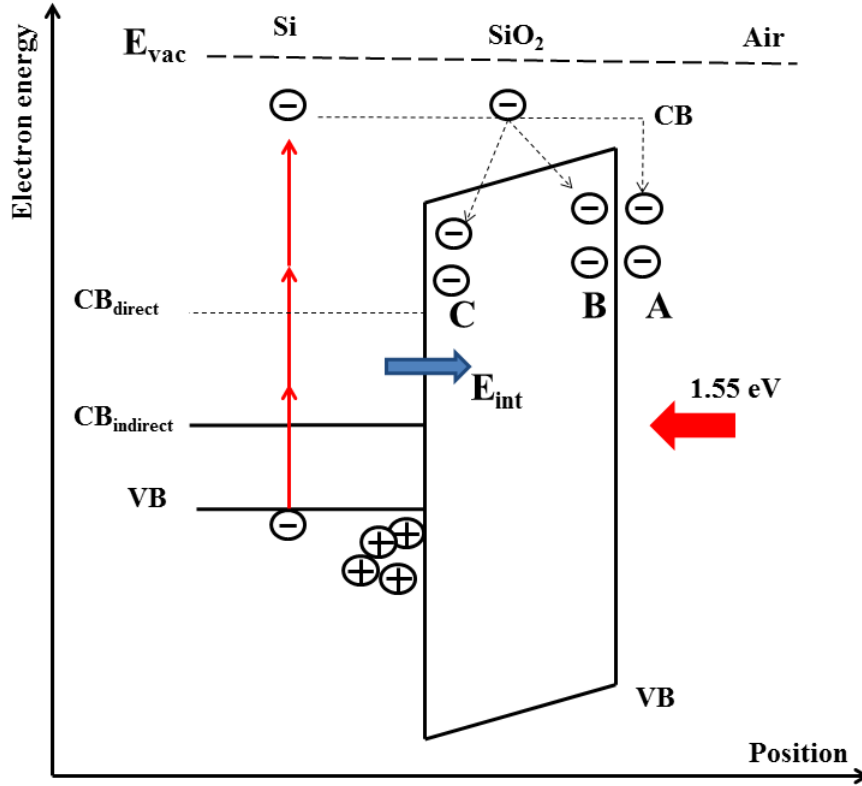


Figure 3.6: Schematic energy band diagram in Si/SiO₂ system when illuminated with a femtosecond laser light at low incident peak intensities; CB_{direct} and $CB_{indirect}$ are the direct and indirect conduction band, respectively; VB is the valence band; E_{vac} , the vacuum energy level; transfer of electron into SiO₂ is achieved by three-photon and cascade of one- and two-photon processes; electron can be trapped at SiO₂/air interface (A), in the bulk Si (B) and at the Si/SiO₂ interface (C).

starts involving electron and hole effects and is given by

$$I^{(2\omega)}(t) \propto \left(1 + \sum_{i=1}^4 a_i \exp(-t/\tau_i) \right)^2, \quad (3.5.7)$$

with a_i and τ_i the amplitudes and time constants of the SH signals.

The contribution involving electron processes in Eq. 3.5.7 is given by [41]:

$$I^{(2\omega)}(t) \propto [1 + a_1 \exp(-t/\tau_1) + a_2 \exp(-t/\tau_2)]^2, \quad (3.5.8)$$

with $a_{1,2} < 0$ and $\tau_{1,2} > 0$,

and the relation (Eq. 3.5.7) involving hole contributions only is given by [41]

$$I^{(2\omega)}(t) \propto [1 + a_3 \exp(-t/\tau_3) + a_4 \exp(-t/\tau_4)]^2, \quad (3.5.9)$$

with $a_{3,4} > 0$ and $\tau_{3,4} > 0$

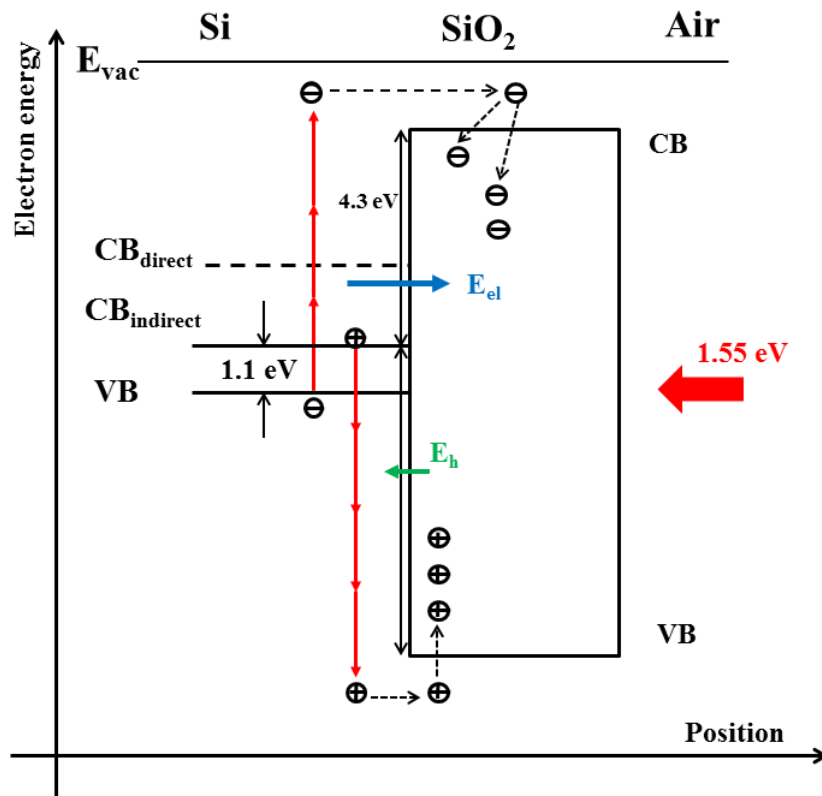


Figure 3.7: Hole (h^+) transfer and trapping in Si/SiO₂ after injection by four-photon excitation: decrease of net interfacial electric field. E_{vac} , vacuum energy level; E_{el} , electric field due to electron transition and trapping from Si to SiO₂; E_h , small contribution of hole processes.

Chapter 4

Experimental

In this chapter, the description of the experimental setup and the optical equipments used to collect data for the characterization of the silicon membranes is explained. A description of the free carrier absorption measurements is given. A characterization of the laser beam as well as the detectors used for simultaneous EFISH measurements in transmission and reflection are also presented. A description of the sample preparation and cleaning process is given.

4.1 Experimental setup

The objectives of these experiments are to do measurements on silicon membranes and be able to simultaneously measure the second harmonic signals in transmission and reflection from the same silicon membrane. In order to achieve that a setup as shown in Fig. 4.1 has to be build. The schematic diagram of the experimental setup shown in Fig. 4.1 can be divided into three parts: the optical source, the detection system and the optical components, which allow the beam to go from the source to the detectors after being incident on the sample.

The optical source used is a titanium-doped sapphire oscillator (Spectra Physics, 3941 – M3S, tsunami) capable of tunable laser operation over a broad range of near infrared (NIR) wavelengths. The energy for the lasing process is provided by a frequency doubled Nd:YVO₄ laser (Spectra Physics, Millennia V) with 5.5 W continuous wave (cw) maximum output power at a wavelength of 532 nm [39]. The laser was tuned at 800 nm output wavelength and the output of the laser is vertically polarized (p-polarization). For second harmonic (SH) measurements, p-p polarization (i.e. vertically polarized incident light and the output SH signal is also vertically polarized) is used because SH signal is higher in this configuration.

The detection system features a power meter (Thorlabs: PM100D) for power

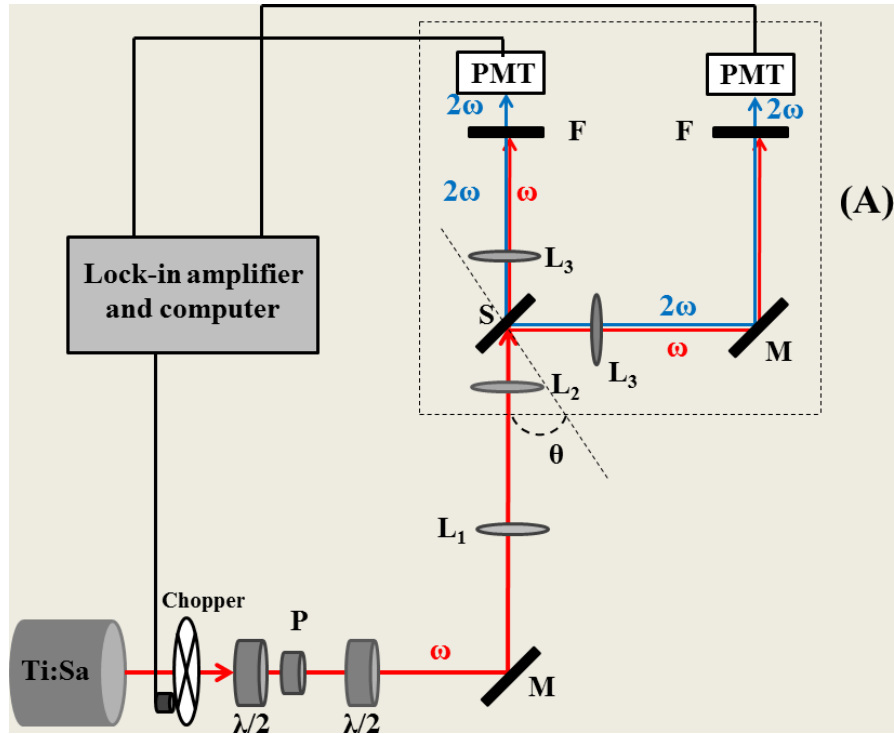


Figure 4.1: Schematic diagram of the experimental setup used for simultaneously measuring second harmonic signals in reflection and in transmission from a thin Si membrane; Ti:Sa, Ti:Sapphire femtosecond laser; $\lambda/2$, half wave plate; F, filter; P_i , polarizers; L_i , lenses; M, silver mirror; PM, photomultiplier tube; ω and 2ω , fundamental and second harmonic signals, respectively; (A) black box shielding PMTs from external light; S, XY translation stage with rotating platform.

measurements, two identical photomultiplier tubes, PMT (Hamamatsu Photonics, Japan, H678003), a digital lock-in amplifier (Zurich Instruments, HF2LI Lock-in Amplifier, 50 MHz, 210 MSa/s) to amplify the signals from the PMTs; a computer equipped with HF2LI software (LabView) for data collection and a chopper (Thorlabs, Optical chopper, MC2000, 1 Hz – 10 kHz frequency range) to enhance the signal-to-noise ratio.

The optical components, used to guide the beams from the optical source to the sample and from the sample to the detection systems, are: two half-wave plates, $\lambda/2$ (Thorlabs, \varnothing^1 : 1 " zero-order half wave plate, 780 nm), a polarizer, P_1 (Thorlabs, Glan-laser polarizer, 10 mm, CA, AR coating: 650 – 1050 nm), silver mirrors, M (Thorlabs, \varnothing : 1" protective silver mirrors, 0.24 " (6.00 mm) thick), lenses with different focal lengths to collimate and focus the beams, a sample holder to hold the sample, S, two filters, F (Schott AG, Mainz, Germany, BG-39, short pass filters for $350 \leq \lambda \leq 590$ nm and $< 0.01\%$ transmission for $\lambda > 700$ nm) and an optical spectrometer (Ocean Optics spectrometer,

¹ \varnothing : diameter

HR4000), not shown on Fig. 4.1, with a CCD array detector equipped with Ocean Optics software which provides a readout on the computer.

Other optical components used (not shown on the experimental setup of Fig. 4.1) are a custom built autocorrelator interferometer made of a beam splitter, BS (50/50 dielectric beam splitter), a custom-modified reversed biased AlGaAs-light emitting diode (LED) [39], and a movable mirror.

4.2 Sample fabrication and preparation

Fabrication and cleaning procedures of Si samples were taken from [106]. The cleaning procedure is a standard method used in our laboratory. The silicon (Si) samples under investigation were fabricated from a bulk silicon wafer using a chemical etching process. An approximately $490\ \mu\text{m}$ thick Si wafer was polished on both sides, with orientation $\langle 100 \rangle$, and moderately p-doped with a doping concentrations of $3 - 6 \times 10^{14}\ \text{cm}^{-3}$ [106]. A low stress silicon nitride layer was deposited by a plasma enhanced chemical vapour deposition process on both sides of the wafer to act as a mask against the etching solution. One side of the wafer surface was patterned in an array of squares ($3 \times 3\ \text{mm}^2$) of exposed silicon while the other side was completely masked. The patterned wafer was immersed in tetramethylammonium hydroxide (TMAH) etching bath under clean room conditions. The wafer was rotated regularly to minimize roughness on the exposed areas. After 72 hours in the slow etching bath, the desired thickness of the remaining silicon membrane was reached. The etching process was terminated and the silicon nitride mask was chemically removed [106].

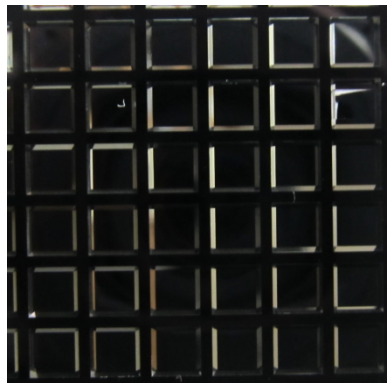


Figure 4.2: Photograph of arrays of weakly p-doped $3 \times 3\ \text{mm}^2$ Si(100) with doping concentration of $2.67 \times 10^{15}\ \text{cm}^{-3}$

Fig. 4.2 shows a photograph of one of the Si membrane samples used in this study, arrays of $3 \times 3\ \text{mm}^2$. Before each measurement, the free standing Si membranes were degrease in organic solvents (methanol, acetone, trichloroethylene,

acetone, methanol) in the listed order and rinsing with deionized water. To remove natural oxide from the wafer, the samples were immersed in diluted hydrofluoric acid (40%). After cleaning, the samples were kept in dark room conditions (room temperature and atmospheric pressure) for 48 hours to allow the growth of natural oxide to reach equilibrium. The uniform ultrathin natural oxide layer is approximately 2 – 3 nm [42]; the samples can be chemically cleaned several times to grow new native oxide layers.

4.3 Laser pulse characterization

Prior to investigating Si membranes, the laser pulses need to be characterized, i.e., the pulse duration and the repetition rate of the laser must be known. Also the laser peak intensity needs to be calculated.

4.3.1 Repetition rate and pulse duration

The pulse repetition rate (PRR) of the laser is defined as the number of pulses emitted per second. The PRR is measured with a pulse train detector connected to an oscilloscope (Tektronix TDS 3032, Two channel color digital phosphor oscilloscope, 300 MHz, 2.5 GS/s). The time between consecutive pulses was found to be 12.5 ns (Fig. 4.3) which gives a repetition rate of 80 MHz. The output spectrum of the laser shown in Fig. 4.5 was recorded using an Ocean Optics spectrometer (HR4000) with a detector connected to a computer (equipped with Ocean Optics Software) via an usb port for readout. A custom built autocorrelator was used to determine the pulse duration of ≈ 80 fs.

The autocorrelation of Fig. 4.4 consists of splitting an incoming pulse into two parts using a 50/50 beam splitter. The two parts of the original incoming pulse are then superimposed in a two-photon detector (AlGaAs -light emitting diode (LED) detector) where two-photon absorption (TPA) takes place, after being reflected back onto themselves by mirrors M_1 and M_2 (movable) and focused onto the detector by a spherical mirror, M_3 . If the optical path length difference is Δx , the time delay between the two splitted beams will be $\Delta t = \Delta x/c$. An interference pattern is then formed and the interference pattern is the autocorrelation function of the laser pulse. The expected maximum signal to offset ratio $PC(S)/PC(O)$ of the autocorrelation function is calculated as follows, taking into account TPA processes in the detector:

$$\frac{PC(S)}{PC(O)} \propto \frac{I(S)^2}{I(O)^2} = \frac{(|E_1 + E_2|^2)^2}{(|E_1|^2)^2 + (|E_2|^2)^2} = \frac{(2E_1)^4}{2E_1^4} = \frac{8}{1}, \quad (4.3.1)$$

where $I(S)$ and $I(O)$ are the resultant signal and offset laser intensities incident on the detector, respectively. E_1 and E_2 are the electric field amplitudes of the

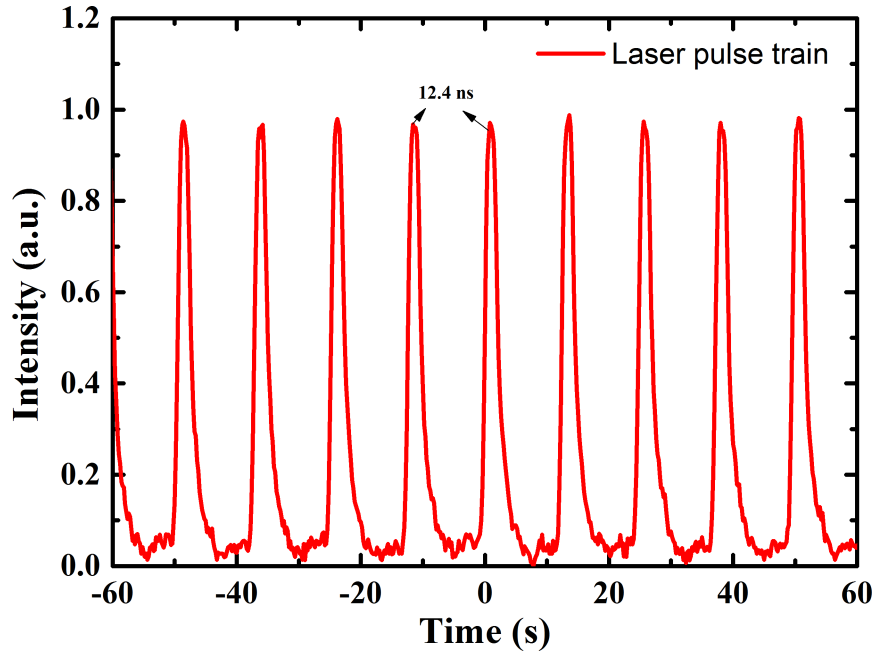


Figure 4.3: Measured pulse train of the femtosecond laser.

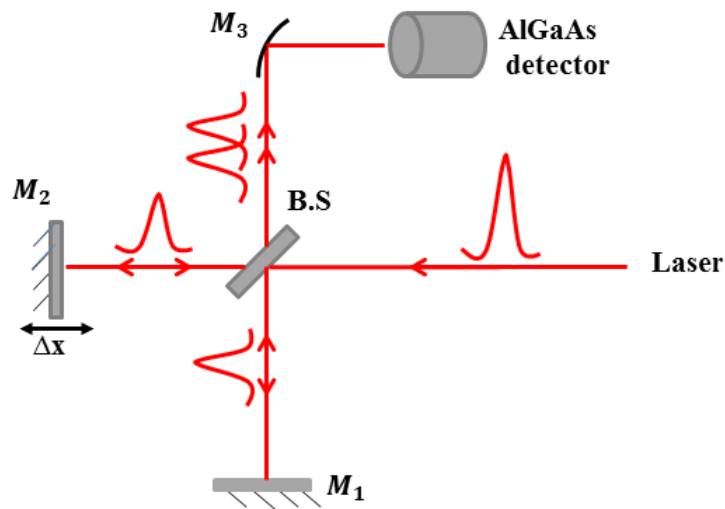


Figure 4.4: illustration of Michelson interferometer. B.S, beam splitter, M_i , silver mirrors; AlGaAs, aluminum gallium arsenide photo detector.

laser pulses originating from the two mirrors M_1 and M_2 , respectively. $E_1 = E_2$ since a 50/50 beam splitter is used. The two parallel beams with electric fields E_1 and E_2 (with $E_1 = E_2 = E$) with a variable delay are generated and focused onto a slow detector to obtain a signal proportional to $(E(t) + E(t - \tau))^2$. Only the beam proportional to the cross-product $(E(t)E(t - \tau))$ is recorded with a slow detector which measures the intensity autocorrelation of the signal

and it is given by:

$$I_{ac}(\tau) = \int_{-\infty}^{\infty} I(t)I(t + \tau)dt. \quad (4.3.2)$$

For a Gaussian shape, the relationship between the duration and spectral bandwidth of the laser is given by the time-bandwidth product $\Delta\tau\Delta\nu \geq 0.44$, where $\Delta\nu$ is the frequency bandwidth at FWHM with $\omega = 2\pi\nu$ and Δt is FWHM in time of the pulse. The minimum time duration of a pulse is given by

$$\Delta\tau \geq \frac{0.44\lambda^2}{c\Delta\lambda}, \quad (4.3.3)$$

where $\Delta\lambda$ is the spectrum bandwidth at FWHM and c the speed of light in vacuum. The pulse duration is determine at the intensity level $1/e$ ($1/\tau$) or $1/e^2$ ($1/\tau^2$). For a Gaussian pulse shape, the relationship between the temporal pulse width at FWHM, τ_p , and the electric field pulse width, $\tau_{1/e}$, is

$$\tau_p = \sqrt{\ln 2}\tau_{1/e}. \quad (4.3.4)$$

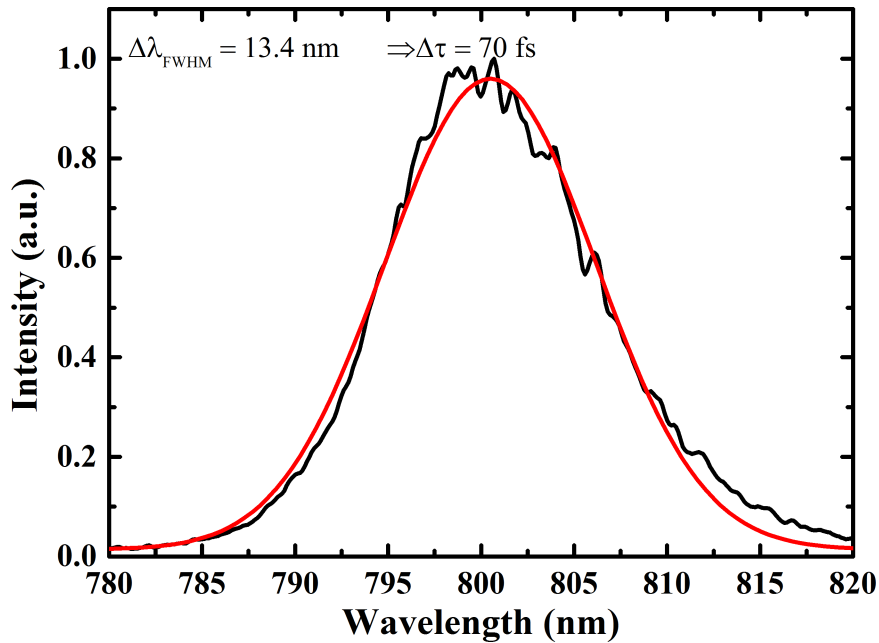


Figure 4.5: Measured spectrum of the optical femtosecond laser used. The pulse duration is calculated using Eq. (4.3.3).

The measured spectrum and autocorrelation trace of the Ti:sapphire laser used, are shown in Fig. 4.5 and Fig. 4.6, respectively. The spectral pulse duration $\Delta\tau(\text{spec})$ was calculated using the following formula Eq. (4.3.3), with $\Delta\lambda$ was measured to be 13.4 nm. The calculated pulse duration of the pulses of the autocorrelation measurement is 80 fs.

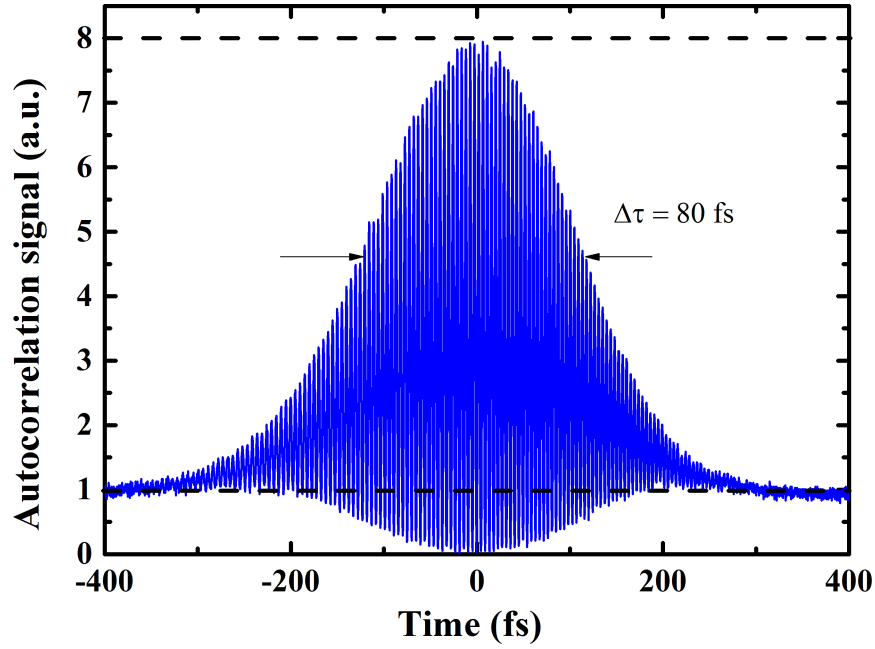


Figure 4.6: Autocorrelation trace measured using Michelson interferometer of Fig. 4.4.

4.3.2 Peak intensity

The spectrum of the fundamental laser beam in Fig. 4.5 has a Gaussian beam profile. The intensity profile of the incident fundamental wave is given by [108]

$$I_{\omega}(x, y) = I_{\omega_0} \exp(-2x^2/w^2) \exp(-2 \cos^2 \theta y^2/w^2), \quad (4.3.5)$$

where I_{ω_0} is the intensity at the position $(x = 0, y = 0)$, θ is the incident angle ($\theta = 45^\circ$ in our case) and $w = w(z)$ the radius of the incident beam of frequency ω at a position z along the propagation direction. $w(z)$ is related to the Rayleigh length by [108]:

$$w = w(z) = w_0 (1 + z^2/z_R^2)^{1/2}, \quad (4.3.6)$$

with $z_R = \pi w^2/\lambda$ and $\lambda = 2\pi c/\omega$, where c is the speed of light in vacuum; $w_0 = w(z = 0)$. The fundamental power, P_{ω} , incident on the sample is obtained by integrating Eq. (4.3.5), which is found equal to:

$$P_{\omega} = I_{\omega_0} \frac{\pi w^2}{2 \cos \theta}. \quad (4.3.7)$$

The generated SH intensity is a quadratic function of the incident fundamental

intensity [39] and is given by

$$I_{2\omega}(x, y) = \eta I_{\omega}^2(x, y) \exp(-4x^2/w^2) \exp(-4 \cos^2 \theta y^2), \quad (4.3.8)$$

with η the SH conversion efficiency constant. The SH power is obtained by integrating over $I_{2\omega}(x, y)$:

$$P_{2\omega} = \eta I_{\omega_0}^2 \frac{\pi w^2}{4 \cos \theta}. \quad (4.3.9)$$

This implies that

$$P_{2\omega} = \eta P_{\omega}^2 \frac{\cos \theta}{\pi w^2} \propto \frac{1}{\omega^2}. \quad (4.3.10)$$

Inserting Eq. (4.3.6) into Eq. (4.3.10) gives

$$P_{2\omega} = \frac{K}{1 + z^2/z_R^2}, \quad (4.3.11)$$

where $K = (\eta P_{\omega}^2)/(\pi w_0^2)$.

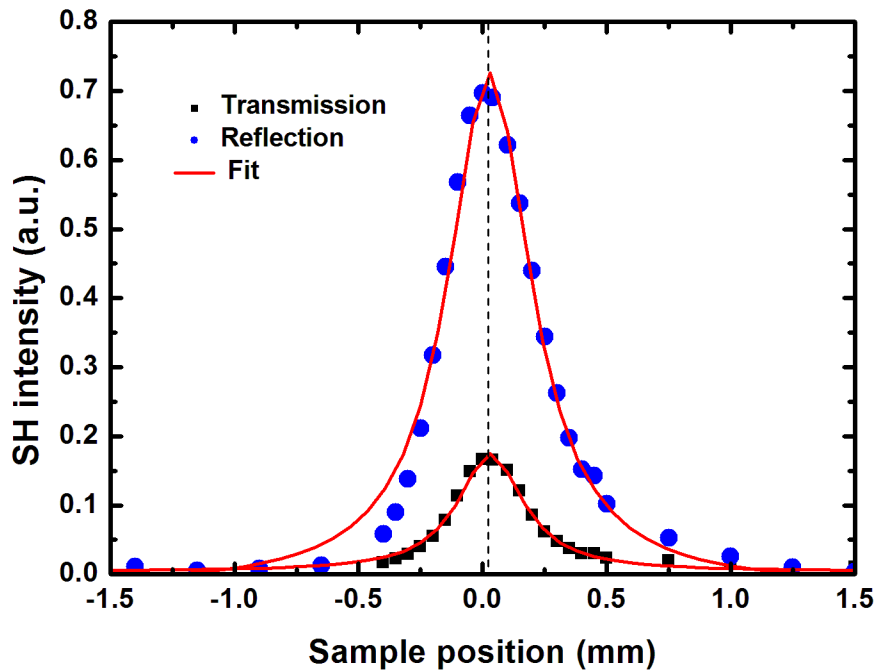


Figure 4.7: Simultaneous measurement of the beam radius in reflection and in transmission at the sample position $z = 0$ on a thin Si membrane. Solid curves are fits according to Eq. (4.3.11).

Fig. 4.7 shows a typical simultaneous measurement of the total SH power $P_{2\omega}(z)$ in transmission and in reflection generated at the Si/SiO₂ interface as a function of the sample position z . The solid curves are fits according to Eq. (4.3.11) with K and z_R the fit parameters. The Rayleigh length was found to be $z_R = 0.122$ mm which corresponds to a beam waist (radius) of $\omega_0 = 5.57$ μm at the focal position $z = 0$. The spot size diameter is (11.2 ± 2) μm .

4.3.3 FCA measurements

The fs Ti:sapphire laser tuned to a central wavelength of $\lambda = 800$ nm ($h\nu = 1.55$ eV) is applied to investigate the linear and nonlinear optical behavior of thin Si membrane samples by measuring the average laser power of the fs pulse train transmitted through the membranes as a function of the incident laser power P_{in} . The vertically polarized (p-polarized) beam from the fs Ti:sapphire laser is collimated and focused by lenses L₁ and L₂, respectively. The beam transmitted through the Si membrane is collected by lens L₃ (see Fig. 4.1). A power meter (Thorlabs PM100D) is used to measure the transmitted and reflected average powers.

4.3.4 Calibration of the photomultiplier tubes

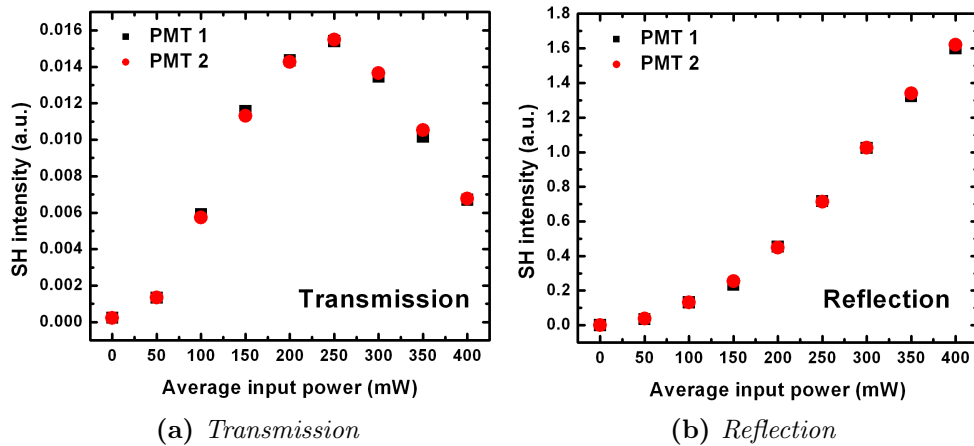


Figure 4.8: Calibration of the photomultiplier tubes; a) in transmission geometry and b) in reflection geometry

Before doing time-dependent second harmonic (TDSH) generation measurements on Si membranes to qualitatively and quantitatively compare the SH signals transmitted through and reflected from the sample, one has to calibrate the photomultiplier tubes (PMTs). The calibration is done by setting up both PMTs to measure the same intensity signal for the same geometry

by adjusting the gain on both PMTs in such a way that they detect the same signal strength for the same geometry as shown in Fig. 4.8.

PMT1 and PMT2 are the photomultiplier tubes measuring the SH intensity in transmission and reflection, respectively. The results show that the PMTs were well balanced prior to comparing the SH signals in transmission and in reflection.

Chapter 5

Results

In this chapter, the experimental results obtained during the investigation of the Si/SiO₂ interfaces of thin Si membranes are reported. Transmitted and reflected fundamental signals, as well as the time-dependent second harmonic signals measured simultaneously in both geometries are reported. The investigation of the linear and nonlinear (FCA) optical behavior of thin Si samples is done by measuring the average laser power of the fs pulse train transmitted through the membranes as a function of the incident laser power (Fig. 5.5).

For the reason explained in section 4.1, all measurements were carried out in the p-p polarization combination, i.e., laser excitation and detection signal are in p-polarization. Second harmonic technique is used as a tool to investigate the Si membrane samples. The samples used are weakly p-doped with different thicknesses. The following measurements were performed:

- time dependent second harmonic (TDSH) generation in reflection on bulk Si samples;
- power measurements of the transmitted and reflected fundamental light; and
- simultaneous TDSH generation measurements in reflection and transmission geometries, for different incident laser intensities, to compare the amplitudes of the signals in transmission and reflection.

5.1 Reflection and transmission of the fundamental laser beam

5.1.1 Fundamental laser wavelength power reflected and transmitted using a femtosecond laser at 800 nm

In chapter 1, Fig. 1.1 shows a schematic diagram of the laser beam reflection from and transmission through a thin Si membrane, illuminated with a femtosecond (fs) laser beam at an angle of $\theta = 45^\circ$, with a frequency ω . The calculated propagation angle inside silicon is $\gamma = 11^\circ$. Figure 5.5 shows an example of power dependences of the fs laser beam reflection and transmission with the contributions of linear absorption (dashed line in Fig. 5.5) and free charge carrier absorption (FCA, shown by the arrow). Laser beam reflection, P_{ref} , shows a nearly perfect linear dependence on the incident laser power P_{in} (Fig. 5.1) with the reflectivity $R = 0.15 \pm 0.001$. This result agrees with previous reports [155, 156] and confirms the validity of the Fresnel equations using the optical constants of the sample under ambient conditions, i.e. refractive indices $n_{air} = 1$, $n_{SiO_2} = 1.45$, and $n_{Si} = 3.69$ [157, 158] yielding $R = 0.155$.

Figures. 5.2 and 5.3 show the measured transmitted power P_{trans} through Si membrane as a function of the incident laser power P_{in} up to 0.8 W. The results show that the transmitted power P_{trans} deviates considerably from linearity (Figs. 5.2 and 5.3): starting with an initial linear increase of P_{trans} for low power P_{in} (< 0.2 W in Figs. 5.2 and 5.3), the transmitted power reaches an absolute maximum value at $P_{in} \approx 0.5 \pm 0.1$ W. For higher laser P_{in} , the transmitted power P_{trans} decreases again. The contributions from internally reflected beams to the transmitted laser power P_{trans} are negligible ($\leq 0.05\%$) even without any account for laser beam attenuation by absorption and scattering in the bulk. The pulse peak intensities incident on the sample amount up to 80 GW/cm^2 averaged over the beam cross section and the pulse duration. Results presented here (Figs. 5.2 and 5.3) do not show error bars because the measurement uncertainty of the instrument (power meter) is 0.5% of the actual measurement range maximum which is too small to be plotted along with the obtained data. The resolution of the power meter is $1 \mu\text{m}$.

For the measurement of the 800 nm transmitted and reflected light, a power meter (Thorlabs: PM100D) is used. No filter is used to block the SH light generated on the sample as its contribution to the measurement is negligibly small. The measurements at 800 nm, especially in transmission through the investigated Si membrane sample helped to estimate the thickness of the sample using the model described in Sect. 5.2 for one-photon absorption inside silicon.

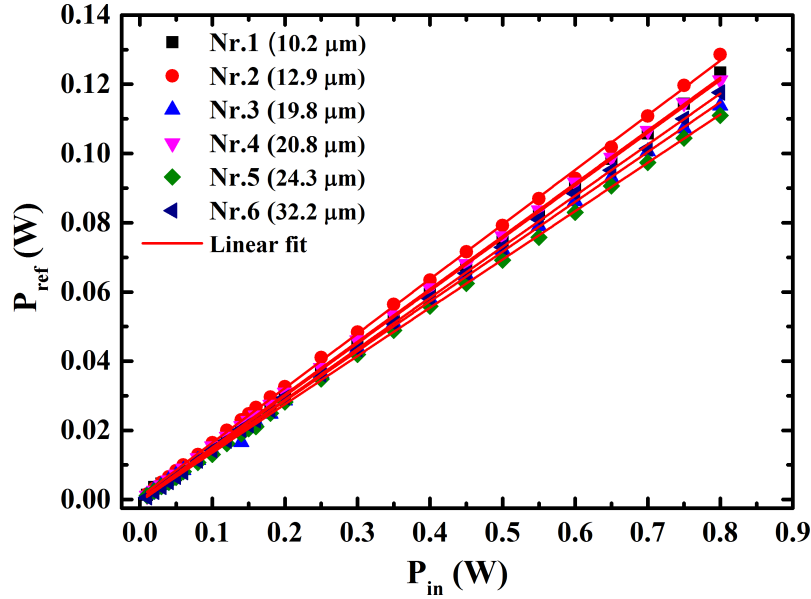


Figure 5.1: Reflected laser power P_{ref} from thin Si membranes as a function of the incident power P_{in} yielding a reflectivity $R = 0.15 \pm 0.01$. Solid lines are linear fits.

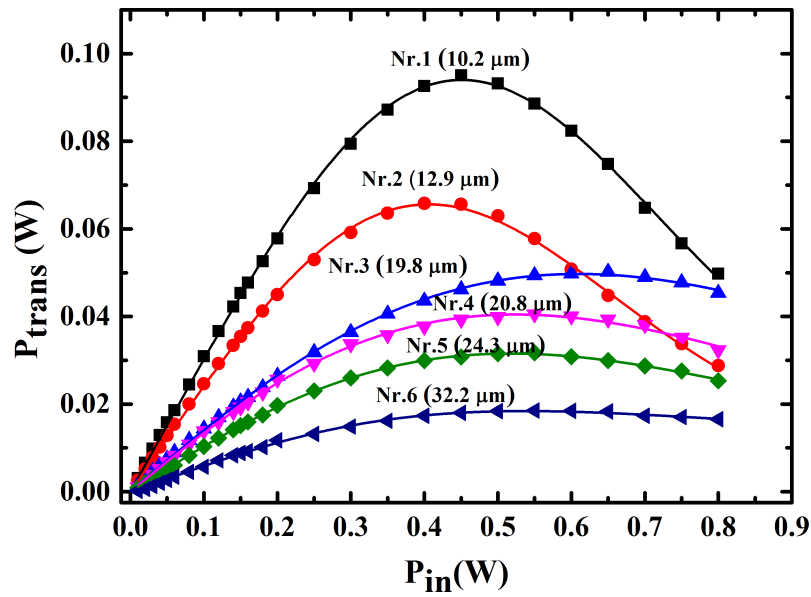


Figure 5.2: Average laser transmitted power P_{trans} of a fs laser pulse train using thin Si membranes as a function of the incident power P_{in} . Solid lines are fits according to Eq. (6.1.12) with n considered as a variable parameter in the fit.

5.1.2 Model calculations

The model developed here will be used to calculate the intensities of the fundamental electric fields in reflection and transmission geometries, compare the intensities at air/SiO₂/Si and Si/SiO₂/air interfaces. In the model, air/SiO₂/Si

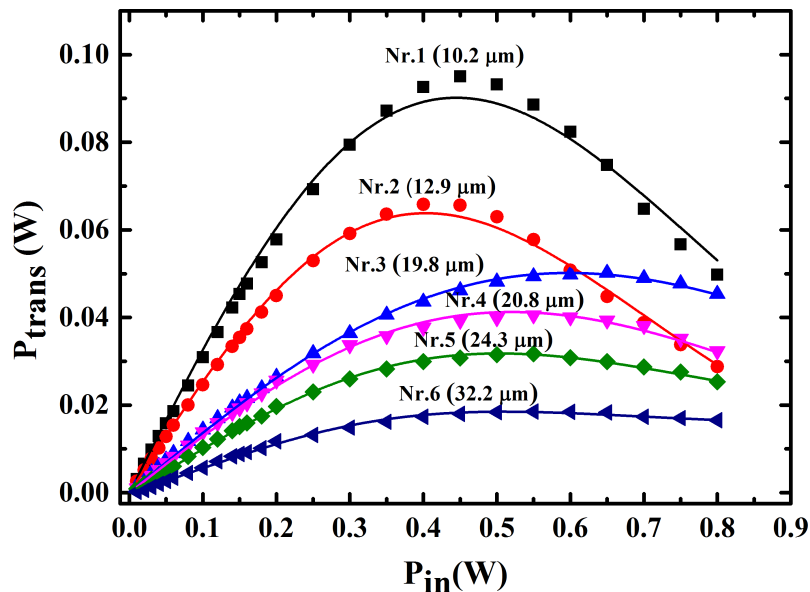


Figure 5.3: Average laser transmitted power P_{trans} of a fs laser pulse train using thin Si membranes as a function of the incident power P_{in} . Solid lines are fits according to Eq. (6.1.12) with $n = 2$ fixed.

and Si/SiO₂/air are defined as "front" and "rear" interfaces, respectively, of the Si model. This is in line with the description of EFISH in reflection by Park et al. [159]. In the following model, we consider only the fundamental electric fields from a single sheet of polarization, located in the Si directly below the SiO₂/Si and Si/SiO₂ interfaces. The dipole approximation will be used throughout. Let us consider a p-polarized incident wave (either in reflection or transmission geometry) and p-polarized second harmonic (SH) wave.

Fig. 5.4 shows a schematic diagram of the light propagation in the Si wafer with native SiO₂ layers. In the description below, numerical subscripts indicate the medium: 0 = air, 1 = SiO₂ and 2 = Si. For the purpose of the model the incident beams are considered to come from different sides of the membrane for reflection and transmission geometries. The propagation paths of the fundamental beam out of the Si through the SiO₂ into air are identical for both reflection and in transmission geometries. Let the magnitude of the electric field of the p-polarized fundamental wave in air before it enters the sample be E_{in} . The Cartesian coordinates are chosen with the x - and y -axis along (100) and (010) crystal plane, respectively. The z -axis is perpendicular to the membrane surfaces. Let us define the vectors direction as follows:

$$\begin{aligned}
 \vec{p}_{0-} &= \cos \theta_0 \hat{x} + \sin \theta_0 \hat{z}, \\
 \vec{p}_{0+} &= -\cos \theta_0 \hat{x} + \sin \theta_0 \hat{z}, \\
 \vec{p}_{2-} &= \cos \theta_2 \hat{x} + \sin \theta_2 \hat{z}, \\
 \vec{p}_{2+} &= -\cos \theta_2 \hat{x} + \sin \theta_2 \hat{z},
 \end{aligned} \tag{5.1.1}$$

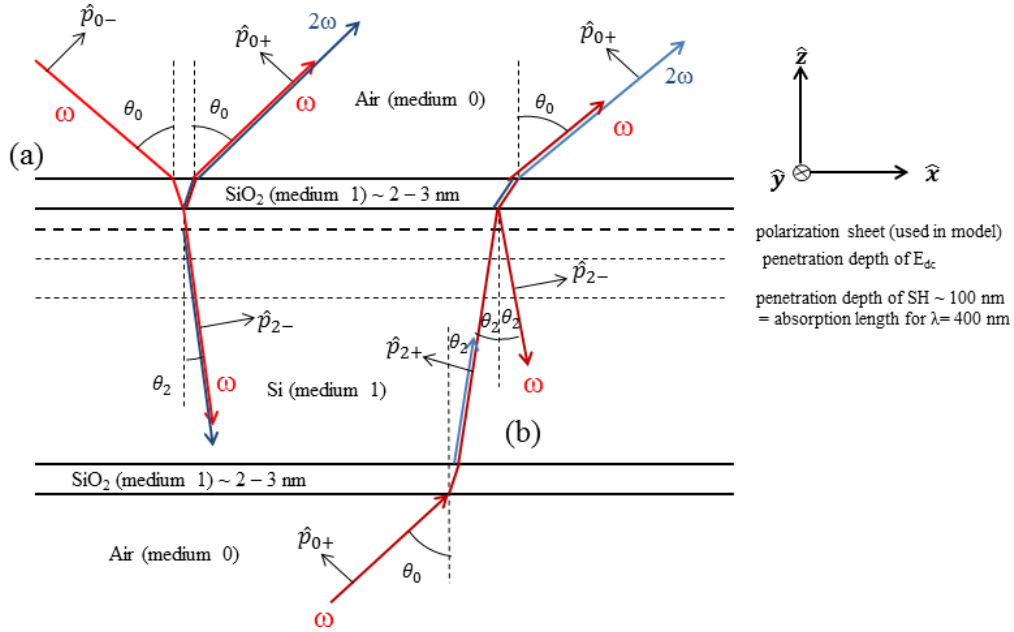


Figure 5.4: Sketch of the beam paths considered in the model for (a) reflection and (b) transmission geometries. Blue beams represent the second harmonic beams escaping from the sample into air. Red beams represent the fundamental beams.

where θ_0 and θ_2 are the angles incident on air/SiO₂ and SiO₂/Si interfaces, respectively.

5.1.3 Calculations of the laser beam intensities at air/SiO₂/Si and Si/SiO₂/air interfaces

The electric field of the incident fundamental wave on the front interface of the sample is given by:

$$\vec{E}_{refl1} = E_{in}\vec{p}_{0-} = E_{in}(\cos\theta_0\hat{x} + \sin\theta_0\hat{z}). \quad (5.1.2)$$

The electric field of the fundamental wave after transmission through the air/SiO₂ and SiO₂/Si interfaces is

$$\vec{E}_{refl2} = t_{01}t_{12}E_{in}\vec{p}_{2-} = t_{01}t_{12}E_{in}(\cos\theta_0\hat{x} + \sin\theta_0\hat{z}), \quad (5.1.3)$$

where t_{ij} are the Fresnel amplitude coefficients of transmission from air/SiO₂ and SiO₂/Si, respectively. The field of the fundamental wave incident on the rear interface of the sample is

$$\vec{E}_{trans1} = E_{in}\vec{p}_{0+} = E_{in}(-\cos\theta_0\hat{x} + \sin\theta_0\hat{z}), \quad (5.1.4)$$

and the fundamental wave after transmission through the air/SiO₂ and SiO₂/Si interfaces is

$$\vec{E}_{trans2} = t_{01}t_{12}E_{in}\vec{p}_{2+} = t_{01}t_{12}E_{in}(-\cos\theta_0\hat{x} + \sin\theta_0\hat{z}). \quad (5.1.5)$$

Then, the fundamental wave propagates through Si membrane of thickness D with path length $l = D/\cos\theta_2$. If both one- and two-photon absorption are considered, the linearized expression on the intensity is given by [160]:

$$I(l) = \frac{\alpha I_0 e^{-\alpha l}}{\alpha + \beta(1 - e^{-\alpha l}) I_0} = \frac{I_0 e^{-\alpha l}}{1 + \frac{\beta}{\alpha}(1 - e^{-\alpha l}) I_0}, \quad (5.1.6)$$

where α and β are the one- and two-photon absorption coefficients, respectively. Therefore, for $I(l) = \frac{c\varepsilon_i}{2n_i} |E(l)|^2 \cos\theta_i$ in medium i with θ the angle between the propagation direction and the normal of the surface considered for the intensity calculation [161], yields

$$\frac{c\varepsilon_i}{2n_i} |E(l)|^2 \cos\theta_i = \frac{\frac{c\varepsilon_i}{2n_i} |E_0|^2 \cos\theta_i e^{-\alpha l}}{1 + \frac{\beta}{\alpha}(1 - e^{-\alpha l}) \frac{c\varepsilon_i}{2n_i} |E_0|^2 \cos\theta_i}.$$

If we assume that the magnitude of the electric field is a real number, then

$$E(l) = \sqrt{\frac{E_0^2 e^{-\alpha l}}{1 + \frac{\beta}{\alpha}(1 - e^{-\alpha l}) \frac{c\varepsilon_i}{2n_i} |E_0|^2 \cos\theta_i}} = E_0 e^{-\frac{\alpha}{2} l} \frac{1}{\sqrt{f(E_0, \theta_i)}}. \quad (5.1.7)$$

where $f(E_0, \theta_i) = 1 + \frac{\beta}{\alpha} \left(1 - e^{-\alpha \frac{D}{\cos\theta_i}}\right) \frac{c\varepsilon_i}{2n_i} |E_0|^2 \cos\theta_i$.

Setting up $E_0 = |E_{trans2}^{(\omega)}| = t_{01} t_{12} E_{in}$, $i = 2$ for propagation in the Si, then

$$E(l) = \frac{t_{01} t_{12} E_{in} e^{-\frac{\alpha}{2} \frac{D}{\cos\theta_2}}}{\sqrt{1 + \frac{\beta}{\alpha}(1 - e^{-\alpha l}) \frac{c\varepsilon_2^{\omega}}{2n_2^{\omega}} (t_{01} t_{12} E_{in})^2 \cos\theta_i}} = \frac{t_{01} t_{12} E_{in} e^{-\frac{\alpha}{2} \frac{D}{\cos\theta_2}}}{\sqrt{f(E_{in}, \theta_2)}}, \quad (5.1.8)$$

where $f(E_{in}, \theta_2) = 1 + \frac{\beta}{\alpha} \left(1 - e^{-\alpha \frac{D}{\cos\theta_2}}\right) \frac{c\varepsilon_2^{\omega}}{2n_2^{\omega}} (t_{01} t_{12} E_{in})^2 \cos\theta_2$. Therefore, the electric field of the fundamental wave reaching the polarization sheet in the Si (medium 2) after attenuation by one- and two-photon absorption in the Si is given by

$$\vec{E}_{trans3}^{\omega} = \frac{t_{01} t_{12} E_{in} e^{-\frac{\alpha}{2} \frac{D}{\cos\theta_2}}}{\sqrt{f(E_{in}, \theta_2)}} \vec{p}_{2+} \quad (5.1.9)$$

$$= \frac{t_{01} t_{12} E_{in} e^{-\frac{\alpha}{2} \frac{D}{\cos\theta_2}}}{\sqrt{f(E_{in}, \theta_2)}} (-\cos\theta_2 \hat{x} + \sin\theta_2 \hat{z}). \quad (5.1.10)$$

The reflection of the fundamental wave from the Si/SiO₂ interface has to be considered too. The reflected electric field at the Si/SiO₂ interface will be in the $-\vec{p}_{2-}$ direction (not in the \vec{p}_{2+})

$$\vec{E}_{trans4}^{\omega} = \left(r_{21} t_{01} t_{12} E_{in} e^{-\frac{\alpha}{2} \frac{D}{\cos\theta_2}} \frac{1}{\sqrt{f(E_{in}, \theta_2)}} \right) (-\vec{p}_{2-}) \quad (5.1.11)$$

$$\vec{E}_{trans4}^{\omega} = r_{21}t_{01}t_{12}E_{in}e^{-\frac{\alpha}{2}\frac{D}{\cos\theta_2}}\frac{1}{\sqrt{f(E_{in},\theta_2)}}(-\cos\theta_2\hat{x} - \sin\theta_2\hat{z}). \quad (5.1.12)$$

The net electric field of the fundamental wave at the polarization sheet is given by the vector sum

$$\vec{E}_{trans}^{\omega} = \vec{E}_{trans3}^{\omega} + \vec{E}_{trans4}^{\omega} \quad (5.1.13)$$

$$\begin{aligned} \vec{E}_{trans}^{\omega} = t_{01}t_{12}E_{in}e^{-\frac{\alpha}{2}\frac{D}{\cos\theta_2}}\frac{1}{\sqrt{f(E_{in},\theta_2)}} \times \\ [- (1 + r_{21}) \cos\theta_2\hat{x} + (1 - r_{21}) \sin\theta_2\hat{z}] \end{aligned} \quad (5.1.14)$$

Therefore, the x and z components will be

$$E'_{x-trans} = -(1 + r_{21})t_{01}t_{12}E_{in}e^{-\frac{\alpha}{2}\frac{D}{\cos\theta_2}}\frac{1}{\sqrt{f(E_{in},\theta_2)}}\cos\theta_2 \quad (5.1.15)$$

$$E'_{z-trans} = (1 - r_{21})t_{01}t_{12}E_{in}e^{-\frac{\alpha}{2}\frac{D}{\cos\theta_2}}\frac{1}{\sqrt{f(E_{in},\theta_2)}}\sin\theta_2 \quad (5.1.16)$$

5.2 Estimation of the thickness of the Si sample

Experimental data were used to estimate the thickness of each Si sample under study. Knowing the intensity of light going through the sample as well as the amount of light incident on the sample, one could estimate the thickness of the sample using Eq. (5.1.6). Taking into account Fresnel coefficients of transmission at air/SiO₂, SiO₂/Si, Si/SiO₂ and SiO₂/air respectively, Eq. (5.1.6) can be written as:

$$I(l) = \frac{a\alpha I_0 e^{-\alpha l}}{\alpha + \beta(1 - e^{-\alpha l})I_0}, \quad (5.2.1)$$

where $a = (t_{01}t_{12}t_{21}t_{10})^2$ and $l = \frac{D}{\cos\theta_2}$. Solving for l , it is found that:

$$l = \frac{D}{\cos\theta_2} = -\frac{1}{\alpha} \ln \left[\frac{(1 + \frac{\beta}{\alpha}I_0) I_{tr}}{(a + \frac{\beta}{\alpha}I_{tr}) I_0} \right], \quad (5.2.2)$$

where I_0 and I_{tr} are the incident and transmitted intensities on and through the Si sample, respectively. Thus, the thickness of the sample D using one- and two-photon absorption, is given by

$$D = -\frac{1}{\alpha} \ln \left[\frac{\left(1 + \frac{\beta}{\alpha} I_0\right) I_{tr}}{\left(a + \frac{\beta}{\alpha} I_{tr}\right) I_0} \right] \cos \theta_2. \quad (5.2.3)$$

If only one-photon absorption is considered, Eq. (5.2.3) reduces to:

$$D = -\frac{1}{\alpha} \ln \left(\frac{I_{tr}}{(t_{01}t_{12}t_{21}t_{10})^2 I_0} \right) \cos \theta_2. \quad (5.2.4)$$

Table 5.1 shows the experimental values of the average incident powers, as well as, the calculated intensities at the front and rear interface and of a Si membrane with a thickness of $24.5 \mu\text{m}$, where P_{in} , P_{ref} and P_{trans} the average incident, reflected and transmitted powers, respectively. I_{in} , I_{ref} , I_{trans} , I_{front} and I_{rear} are the incident, reflected, transmitted intensities, the intensity at the front (SiO_2/Si) and rear (Si/SiO_2) interfaces, respectively.

Table 5.1: Calculated intensities from transmitted and incident powers where $P_{in}, P_{trans}, P_{ref}, I_{in}, I_{ref}, I_{front}, I_{rear}$ and I_{trans} are the incident power, transmitted power, reflected power, the incident intensity, the intensity at the front interface, the intensity at the rear interface and the transmitted intensity, respectively

P_{in} (W)	P_{tr} W	P_{ref} W	I_{in} (GW/cm ²)	I_{ref} (GW/cm ²)	I_{front} (GW/cm ²)	I_{rear} (GW/cm ²)	I_{tr} (GW/cm ²)
0.02	0.00174	0.00256	3.748	0.4798	3.166	0.3861	0.3261
0.03	0.0026	0.00382	5.622	0.7159	4.749	0.5769	0.4873
0.04	0.00344	0.00526	7.496	0.9858	6.331	0.7633	0.6447
0.05	0.00444	0.00666	9.37	1.248	7.914	0.9852	0.8321
0.06	0.00542	0.00864	11.24	1.619	9.497	1.203	1.016
0.08	0.00732	0.01104	14.99	2.069	12.66	1.624	1.372
0.1	0.00934	0.01452	18.74	2.721	15.83	2.072	1.75
0.12	0.01074	0.01756	22.49	3.291	18.99	2.383	2.013
0.14	0.01262	0.0201	26.24	3.767	22.16	2.8	2.365
0.15	0.0135	0.02182	28.11	4.089	23.74	2.995	2.53
0.16	0.01414	0.0235	29.99	4.404	25.33	3.137	2.65
0.18	0.01568	0.02654	33.73	4.974	28.49	3.479	2.939
0.2	0.01728	0.02932	37.48	5.495	31.66	3.834	3.238
0.25	0.02012	0.0368	46.85	6.897	39.57	4.464	3.771
0.3	0.02264	0.04438	56.22	8.317	47.49	5.023	4.243
0.35	0.02448	0.05394	65.59	10.11	55.4	5.432	4.588
0.4	0.02604	0.05928	74.96	11.11	63.31	5.778	4.88
0.45	0.0265	0.0667	84.33	12.5	71.23	5.88	4.966
0.5	0.02726	0.07424	93.7	13.91	79.14	6.049	5.109
0.55	0.0274	0.0826	103.1	15.48	87.06	6.08	5.135
0.6	0.02658	0.0898	112.4	16.83	94.97	5.898	4.981
0.65	0.02574	0.0976	121.8	18.29	102.9	5.711	4.824
0.7	0.02494	0.105	131.2	19.68	110.8	5.534	4.674
0.75	0.0234	0.1132	140.6	21.21	118.7	5.192	4.385
0.8	0.02154	0.1204	149.9	22.56	126.6	4.779	4.037

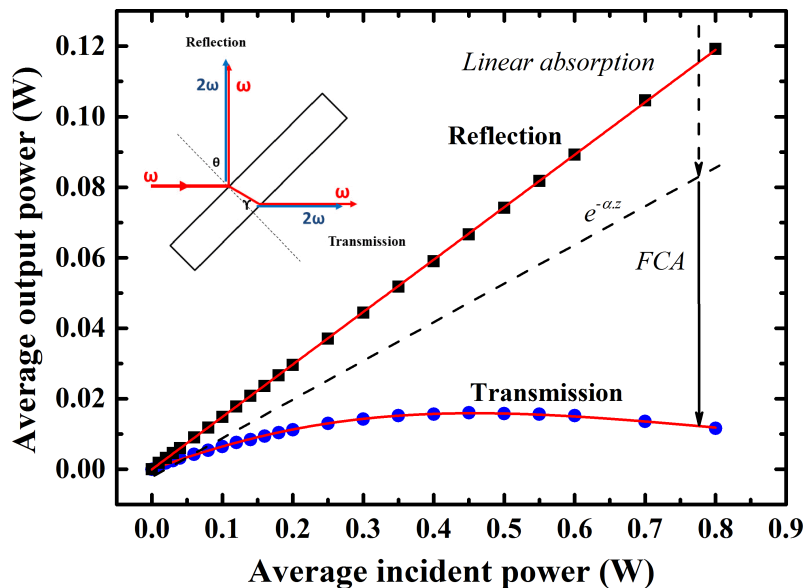


Figure 5.5: Typical power dependence of the fs laser beam reflection and transmission through a thin silicon membrane of $32.9 \mu\text{m}$ when irradiated with a fs laser at 800 nm with the contributions of linear absorption ($e^{-\alpha z}$) and free charge carrier absorption (FCA) indicated by arrows; inset: scheme of the experimental setup with an external angle of incidence $\theta = 45^\circ$ and propagation angle $\gamma = 11^\circ$ within silicon.

Fig. 5.5 shows the fundamental transmitted and reflected power as a function of the average incident powers on a Si membrane with a thickness of $32.9 \mu\text{m}$. The linear part of the transmitted data was used to estimate the thickness of the sample based on Eq. (5.2.4).

5.3 Time-dependent second harmonic measurements

The main reason for doing these measurements is to compare the amplitudes of the SH signals in transmission and reflection from the same oxidized Si membrane. Once the experimental setup has been characterized with balanced detectors, simultaneous measurements of the EFISH signals in transmission and reflection of Si membrane can be carried out.

In this section, the SH measurements performed on native Si/SiO₂ interfaces, for both bulk Si and Si membranes, are presented. All samples are natively oxidized bulk Si and Si membranes and the measurements are done under p-polarization excitation and p-polarization detection. The first set of measurements shows the time-dependent second harmonic (TDSH) response of virgin bulk Si/SiO₂ interfaces, the second set of measurements shows the TDSH on bulk Si/SiO₂ interface with intermediate dark periods (for low and high peak

intensities). The third set of measurements provides simultaneous measurements of SH signals in transmission and reflection geometries from the same Si membrane and the last one is showing simultaneous TDSH measurements in transmission and reflection geometries from the same Si membrane with intermediate dark periods.

The main objectives of these SH measurements include the confirmation, comparison of the predicted results by G. P. Nyamuda [40, 106] under improved experimental conditions, and setting up a new experimental setup capable of measuring simultaneously SH signals in transmission and reflection from the same Si membrane. The characterization of the laser, the experimental setup, the photomultiplier tubes and polarization was done in Chap. 4. EFISH measurements on bulk silicon are done as a test to check the capability of the system to measure SH signals in reflection since EFISH in reflection is well known and well-established in our laboratory [40, 41, 67, 69–71, 150, 151, 162]

5.3.1 Time-dependent second harmonic measurements on bulk Si

The time-dependent second harmonic measurements on bulk Si were done to confirm previous results [40, 41, 150, 151] with a different experimental setup and to make a direct comparison between second harmonic of thin Si membranes and bulk Si.

For peak intensities $\leq 33 \text{ GW/cm}^2$ of Fig. 5.6, the SH intensity increases on a time scale of minutes and subsequently reaches an equilibrium level. The observed data are fitted using Eq. (3.5.8) and these data are consistent with previous work done by other authors [18, 19, 22, 38]. For peak intensities $> 33 \text{ GW/cm}^2$, the SH intensity increases within 1 – 2 minutes, reaches a maximum and thereafter decreases on a time scale of many minutes.

As mentioned previously by Scheidt et al. [41], this behavior becomes more pronounced at higher peak intensity. The solid curves, for this regime, are reproduced using four exponential functions according to Eq. (3.5.9). These results are consistent with what was reported previously [41, 151]

Fig. 5.7 is also an attempt to reproduce with the newly implemented experimental setup work done previously on bulk Si [41]. It shows a temporal evolution of SH signals in reflection (low and high peak intensities) as well as the subsequent SH responses on alternating dark and irradiation periods. After irradiating the sample for a period of 960s, the laser beam is blocked for 10s (indicated by dashed line A), unblocked for 60s until SH recovery, then blocked for 20s (indicated by dashed line B) and unblocked for 60s until recovery, and so forth. The next blocking times are 30s (C), 60s (D), 180s (E), 360s (F), and 600s (G) with intermediate irradiation times of 180s (D),

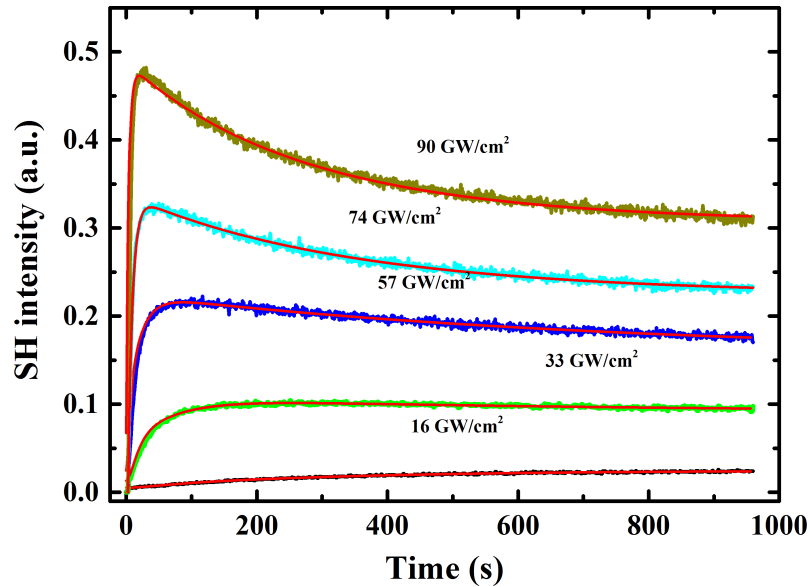


Figure 5.6: Temporal evolution of the EFISH signal in native Si/SiO_2 interfaces of a Si membrane illuminated at peak intensities $> 33 \text{ GW}/\text{cm}^2$ (high regime) and $\leq 33 \text{ GW}/\text{cm}^2$ (low regime). Solid lines are fit curves using two exponential functions (Eq. (3.5.8) for electron dynamics at low regime and four exponential functions, i.e., two functions as in low regime complemented by two exponential functions for hole dynamics (high regime), represented by Eq. (3.5.9).

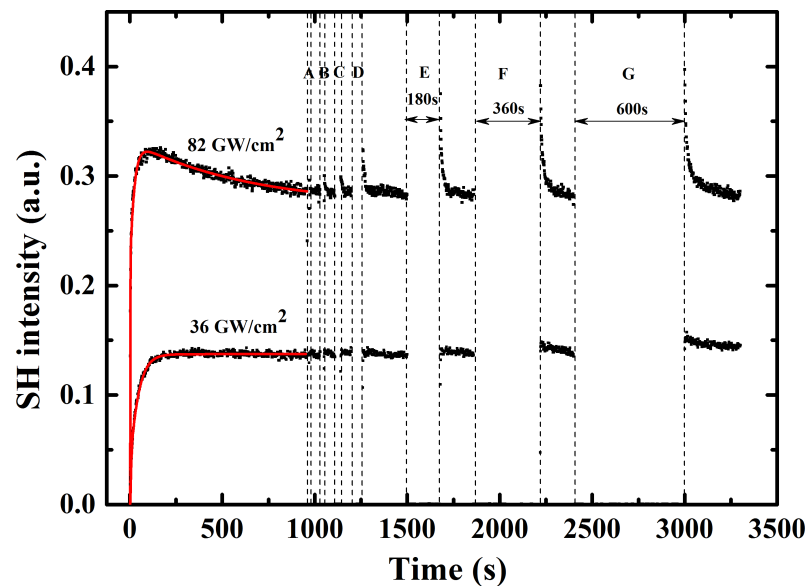


Figure 5.7: Temporal evolution of the EFISH signal in native Si/SiO_2 interfaces irradiated at various peak intensities. A-G indicate dark periods of 10 s (A), 20 s (B), 30 s (C), 60 s (D), 180 s (E), 360 s (F), and 600 s (G).

(E), (F), and (G) to allow signal recovery [41].

5.3.2 SH response of virgin Si membrane samples

Figures 5.8 and 5.9 show the temporal SH signal evolution of Si/SiO₂ interfaces as a function of the applied peak intensity in reflection and transmission geometries, respectively. Each measurement was performed on a "virgin" sample spot. The laser light focus was optimized to measure a simultaneous maximum SH signal in transmission and reflection, as was shown in Fig. 4.7.

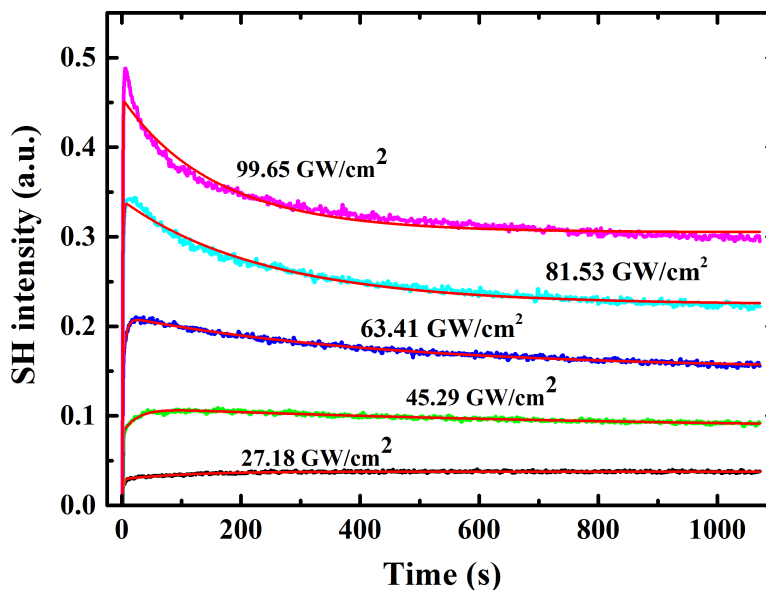


Figure 5.8: Time dependent SH signals from a 33.6 μm thick Si membrane measured in reflection, for different incident laser peak intensities at the front SiO₂/Si interface, as a function of the irradiation time. The solid lines are fits according to Eq. (3.5.9).

The SH signals measured in reflection geometry show similar results as for bulk Si which was described in Sect. 5.3.1. As the incident peak intensity is increased, the SH signal increases and reaches equilibrium, for peak intensities $\leq 45.3 \text{ GW/cm}^2$, which for peak intensity $> 45.3 \text{ GW/cm}^2$ the SH increases, reaches a maximum and then decreases till it reaches equilibrium. This effect was reported by different research group [18, 34, 40, 41, 67, 68, 70, 71, 150, 151, 162] as the electric field induced second harmonic (EFISH) generation.

For transmission geometry in Fig. 5.9, the temporal evolution of the SH from Si/SiO₂ interfaces of Si membrane was recorded at different laser intensity (intensities at the back interface). These intensities were calculated using Fresnel equations at $n(\text{air}) = 1$, $n(\text{Si}) = 3.69$, and $n(\text{SiO}_2) = 1.45$ for 800 nm [40]. The results show the same trend as for those of the TDSH signals in reflection geometry for bulk Si irradiated at peak intensities $\leq 45.3 \text{ GW/cm}^2$ [41]. Therefore Eq. (3.5.8) is used to reproduced the experimental findings.

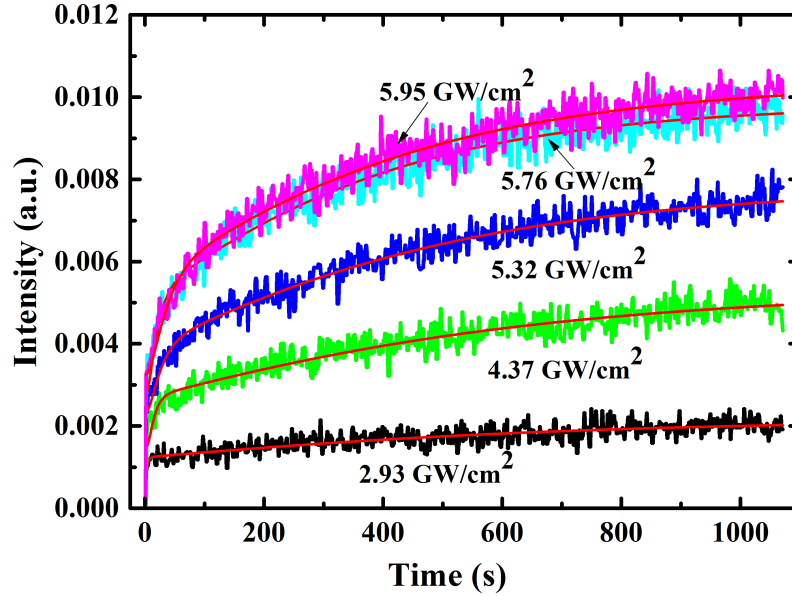


Figure 5.9: Time dependent SH signals through a $33.6 \mu\text{m}$ thick Si membrane measured in transmission, for different calculated laser peak intensities at the rear Si/SiO₂ interface, as a function of the irradiation time. The solid lines are fits according to Eq. (3.5.8).

5.3.3 SH response of pre-irradiated Si membrane samples

Figure 5.10 and 5.11 display measurements of second harmonic signals reflected from and transmitted through a silicon membrane as a function of the irradiation time, respectively. Those sets of measurements were done simultaneously. Each measurement starts on a virgin sample spot. The beam is blocked for 10 s after 960 s of irradiation, then unblocked and so forth as described in Sect. 5.3.1.

For SH signals transmission through the Si membrane of Fig. 5.11, the SH signal increases as the irradiation time increases [90]. The transmitted intensities for the TD were calculated from transmitted powers and using Fresnel's equations at air/SiO₂ and SiO₂/Si interfaces. These intensities are calculated from transmitted power (measured) using Fresnel equations without part reflected from near Si/SiO₂ and SiO₂/Si interfaces. Upon re-irradiation the SH intensity returns instantaneously to the initial level before the dark period.

For reflection geometry from the Si membrane, Fig. 5.10 shows a time evolution of the SH intensity for different peak intensities. For low peak intensity (27.2 GW/cm^2) the EFISH signal increases on a time scale of minutes, then reaches an equilibrium value while for high peak intensities ($> 27.2 \text{ GW/cm}^2$), the SH signal increases on a time scale of seconds, reaches a maximum and then decreases again before reaching an equilibrium value [90]. These results

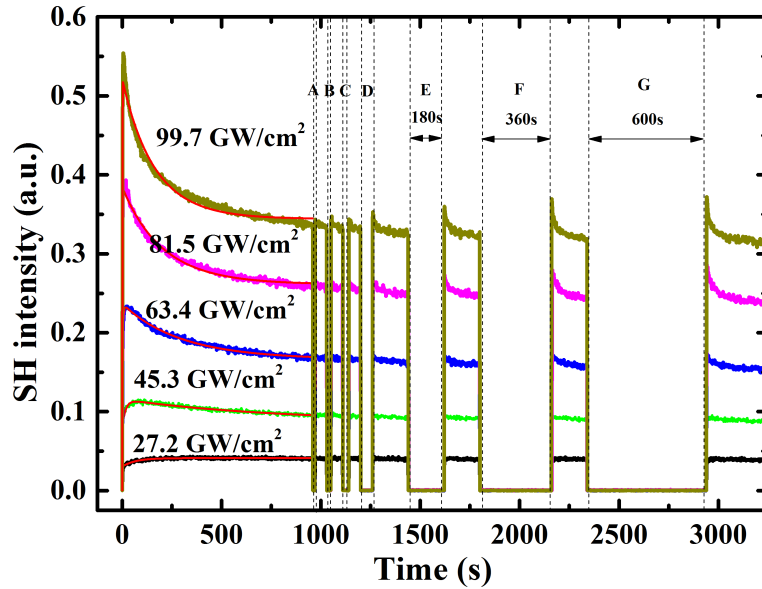


Figure 5.10: SH traces measured in reflection from a $33.6 \mu\text{m}$ thick Si membrane with interrupted irradiation time of 10 s (A), 20 s (B), 30 s (C), 60 s (D), 180 s (E), 360 s (F) and 600 s (G) with irradiation times of 180 s in between (D), (E), (F) and (G).

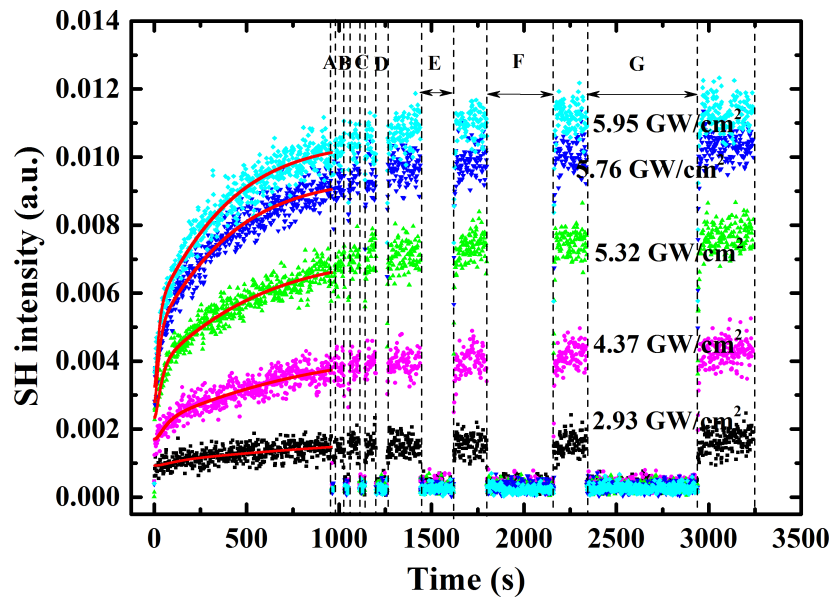


Figure 5.11: SH traces measured in transmission through a $33.6 \mu\text{m}$ thick Si membrane with interrupted irradiation time of 10 s (A), 20 s (B), 30 s (C), 60 s (D), 180 s (E), 360 s (F) and 600 s (G) with irradiation times of 180 s in between (D), (E), (F) and (G).

are reproduced for the first 960 s using Eq. (3.5.8) (low peak intensity) and Eq. (3.5.9) (high peak intensity). It is observed that:

- (i) Upon re-irradiation the SH intensity increases above the level before the dark period but less than the initial SH intensity upon onset of laser irradiation.
- (ii) The decline after each new SH signal maximum occurs on a significantly shorter time scale than the slow decline after the initial maximum of the virgin spot. This was also observed for bulk Si in Fig. 5.6 and Fig. 5.7 and in [41].

5.3.4 SH response of Si membrane with different thicknesses

The temporal evolution of the SH signal was also measured on Si membranes with different thicknesses of $19.4\ \mu\text{m}$ (Fig. 5.12 and Fig. 5.13), $28.2\ \mu\text{m}$ (Fig. 5.14 and Fig. 5.15) and $32.3\ \mu\text{m}$ (Fig. 5.16 and Fig. 5.17), respectively. For each specific thickness, the SH signals in transmission and reflection were measured simultaneously.

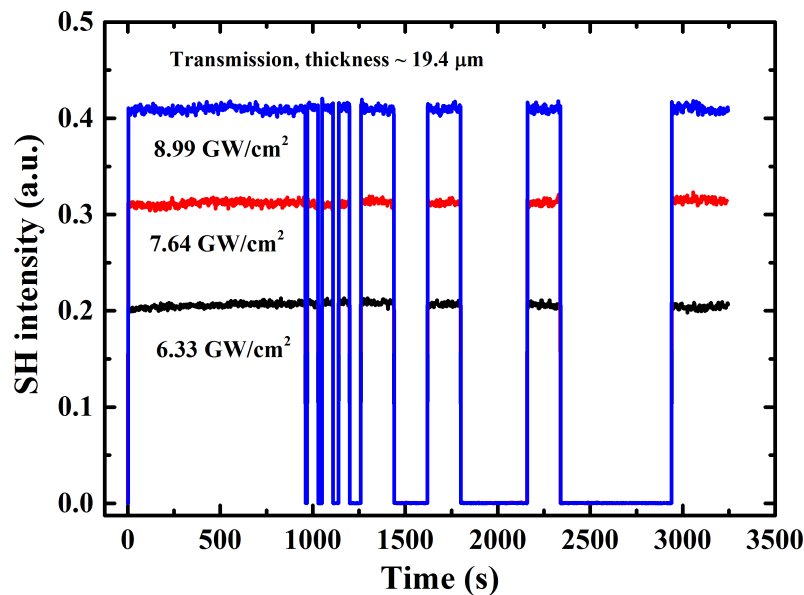


Figure 5.12: Time dependent SH signal in transmission from a Si membrane with thickness of $\approx 19.4\ \mu\text{m}$.

For the Si membrane with thickness of $19.4\ \mu\text{m}$, the time-dependent SH signals measured in transmission in Fig. 5.12 show a constant SH signal upon irradiation of the sample with a femtosecond laser, while the subsequent time-dependent SH in reflection of the same Si membrane shows a dynamics evolution of the SH signal (Fig. 5.13).

In Fig. 5.14 and Fig. 5.16, the SH signal increases as the "calculated" incident peak intensity (rear interface) increases, reaches a maximum and then decreases again. Fig 5.18 shows how the SH signals in transmission, for $19.4\ \mu\text{m}$

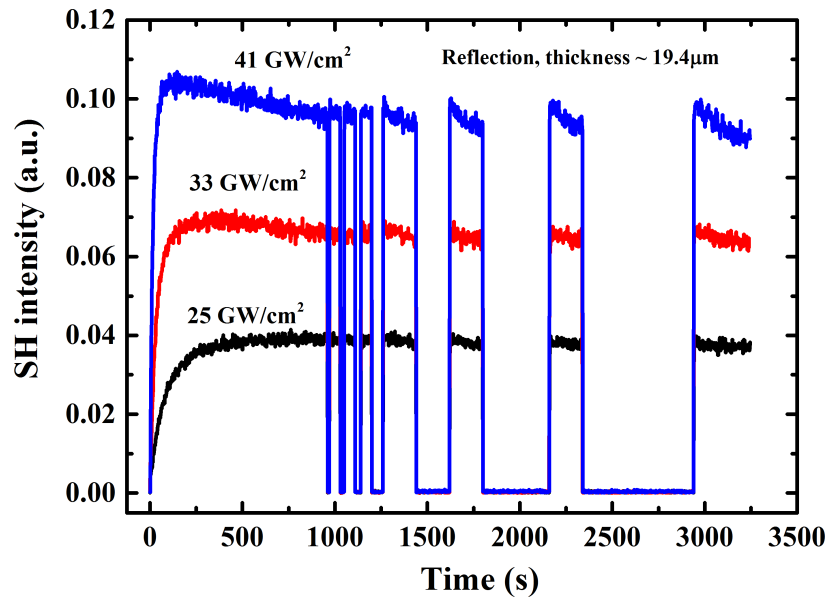


Figure 5.13: Time dependent SH signal in reflection from a Si membrane with thickness of $\approx 19.4 \mu\text{m}$.

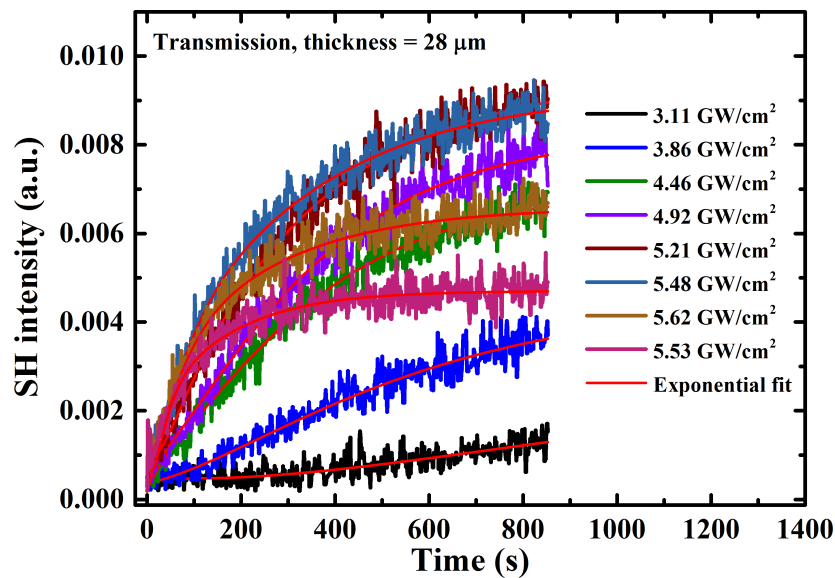


Figure 5.14: Time dependent SH signal in transmission from a Si membrane with thickness of $\approx 28.2 \mu\text{m}$.

and $34 \mu\text{m}$ samples, increase, reach a maximum and decrease. Their SH signals in reflection (Fig. 5.13, Fig. 5.15 and Fig. 5.17) exhibit the same behaviour as described for bulk Si and other Si membranes.

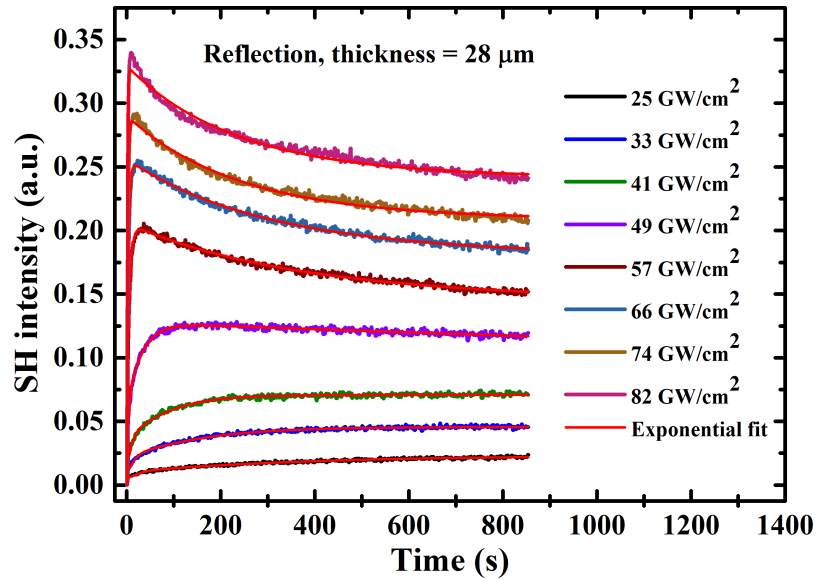


Figure 5.15: Time dependent SH signal in reflection from a Si membrane with thickness of $\approx 28.2 \mu\text{m}$.

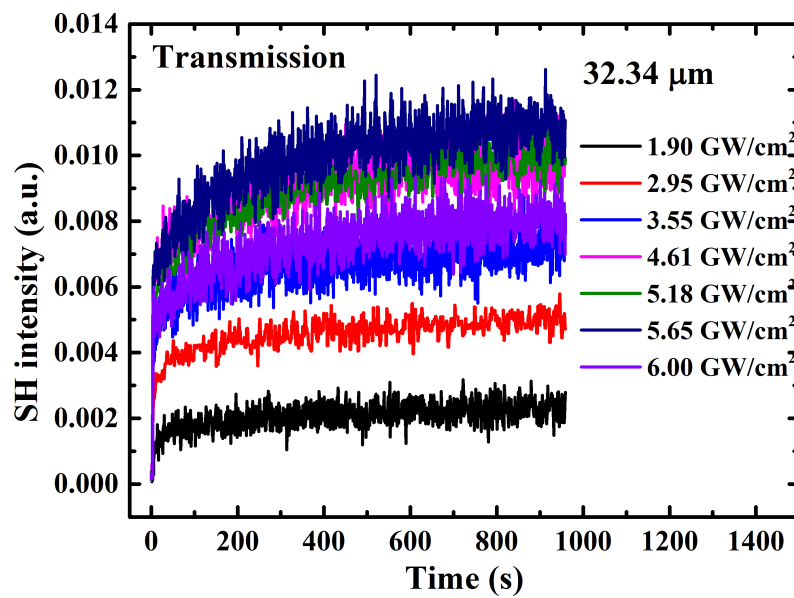


Figure 5.16: Time dependent SH signal in transmission from a Si membrane with thickness of $\approx 32.3 \mu\text{m}$.

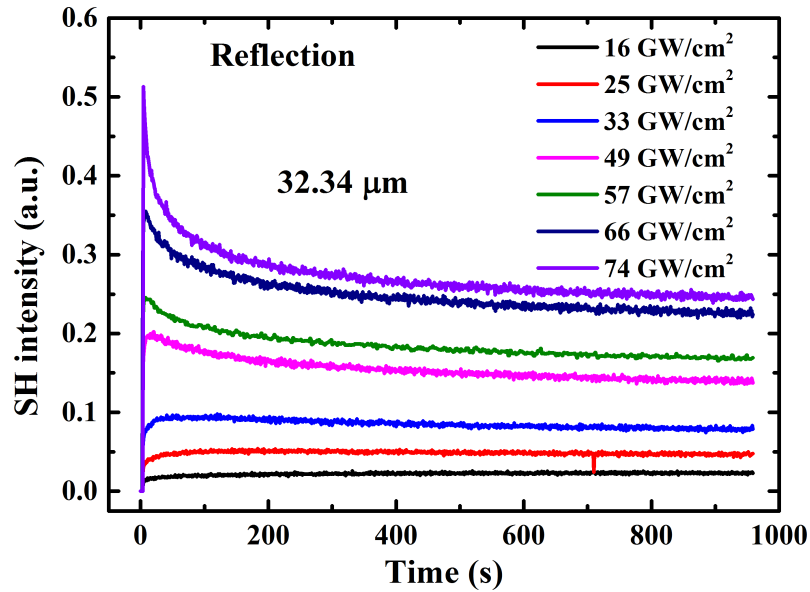


Figure 5.17: Time dependent SH signal in reflection from a Si membrane with thickness of $\approx 32.3 \mu\text{m}$.

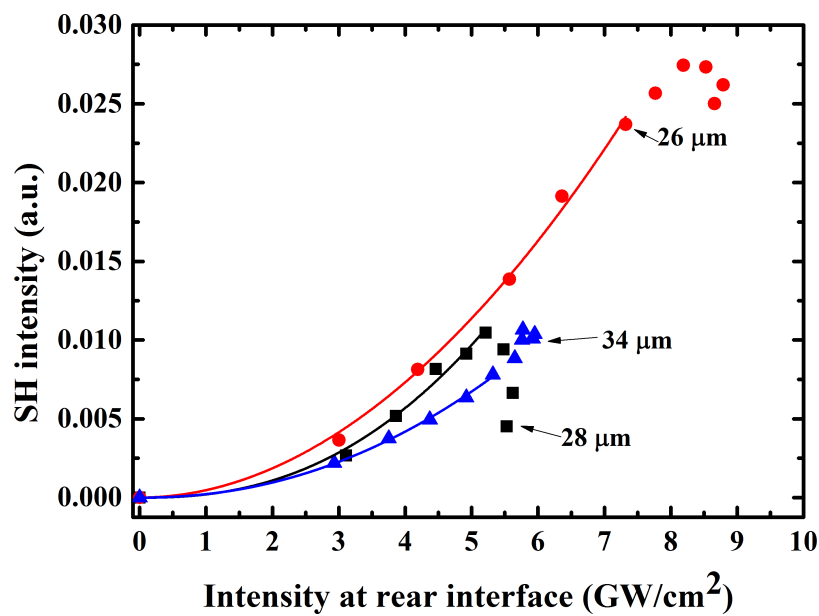


Figure 5.18: Saturated SH intensity in transmission, obtained on Si membranes with thicknesses of $28 \mu\text{m}$ and $34 \mu\text{m}$, respectively

Chapter 6

Discussion

In this chapter the experimental results obtained in Chap. 5 are presented and discussed. Firstly, a discussion of fundamental laser beam reflection and transmission are presented; then the time-dependent second harmonic results of virgin bulk and silicon membranes in reflection and transmission are discussed.

6.1 Reflection and transmission of the fundamental laser wavelength power

The obtained results in Figs. 5.2 and 5.3 can be explained using works we have done on Si membranes [10]. Discussion of these results are explained by considering a low power regime where Beer's law is applicable (indirect interband transition) and in the high incident power regime, where free charge carrier absorption (FCA) is considered as the effect controlling the experimental findings [6, 9, 10].

For weakly doped Si samples, the lifetime of electron-hole (eh) pairs in thermal equilibrium is about $\tau_{eh} \approx 10^{-5}$ s [163, 164]. This lifetime is longer than the laser pulse train interval duration used for the excitation of the Si membranes (12.5 ns); during this long time additional absorption of the laser beam by free charge carriers is generated. The build-up of eh pairs occurs during pulsed irradiation which leads to a power dependent stationary density n_{eh} of eh. The n_{eh} density is determined by the ratio between the power dependent eh pairs generation and its losses. The experimental results of Fig. 5.2 are approximated, at low incident power P_{in} , by Beer's law (linear absorption) and at high incident power by additional absorption defined by FCA [6, 8, 9, 94, 155, 164–176]

Free charge carrier absorption has been studied by many research groups under different experimental conditions [6, 9, 155, 169, 173, 176–180]. These condi-

tions depend on the optical characteristics of the sample (thickness) and the mode of irradiation such as wavelength, pulse repetition rate as well as the temporal and spatial pulse shapes.

6.1.1 Linear laser beam absorption (Beer's law)

The transmitted intensity $I(z_m)$ of femtosecond laser light through a sample is given by (Beer's law)

$$I(z_m) = I_0 e^{-\alpha_1 \cdot z_m}, \quad (6.1.1)$$

where I_0 , α_1 and $z_m = d/\cos \gamma$ are the incident intensity, the linear absorption coefficient of Si at λ_{laser} and the optical path length within the Si membrane of thickness d , respectively. γ is the propagation angle inside silicon when light is incident at a non-zero angle of incidence. I_0 and $I(z_m)$ indicate the intensities at the front $I(z = 0)$ and rear $I(z = z_m)$ sides of silicon membranes behind and before the Si/SiO₂ interfaces, respectively.

Equation 6.1.1 can be expressed in a logarithmic form

$$\ln(I(z_m)/I_0) = -\alpha_1 \cdot z_m, \quad (6.1.2)$$

The relations between I_0 , $I(z_m)$, P_{in} and P_{trans} are established by assuming $I_0 = \kappa_{in} \cdot P_{in} \cdot T_{air/Si}$ and $I(z_m) = \kappa_{trans} \cdot P_{trans} / T_{Si/air}$ where $T_{air/Si} = T_{Si/air} = 1 - R = 0.845$ (R : reflectivity) is the intensity transmission factor from air through the SiO₂ layer into Si and from Si through the SiO₂ layer into air, respectively [11]. κ_{in} and κ_{trans} are factors used to convert the average laser power to the laser pulse intensity. If we assume identical spatial and temporal beam profiles at the front and rear sides of the membrane, then $\kappa_{in} = \kappa_{trans}$. In equation (6.1.2) I_0 and $I(z_m)$ can be replaced by the measured values P_{in} and P_{trans} (Figs. 5.2, 5.3, respectively, and yield [11]:

$$\ln(I(z_m)/I_0) = \ln(P_{trans}/P_{in}) - \ln T^2 = -\alpha_1 \cdot z_m \quad (6.1.3)$$

As quoted in [11] "Eq. (6.1.3) provides the basis of Fig. 6.1 and the option to empirically determine the product $\alpha_1 z_m$ for each investigated Si membrane. As far as Beer's law is applicable, the product $\alpha_1 z_m$ should stay constant in dependence of P_{in} and have a specific value for each membrane thickness $d = z_m \cos \gamma$ and allows to estimate the P_{in} range of linear absorption (Beer's law) for the individual Si membranes. Consequently the P_{in} range of linear absorption is characterized by the horizontal part of each trace in Fig. 6.1 as indicated by the dashed lines."

At low incident power P_{in} , the traces ($-\alpha_1 \cdot z_m$) turn to negative values due to small power measurement errors (baseline imperfections), while for high

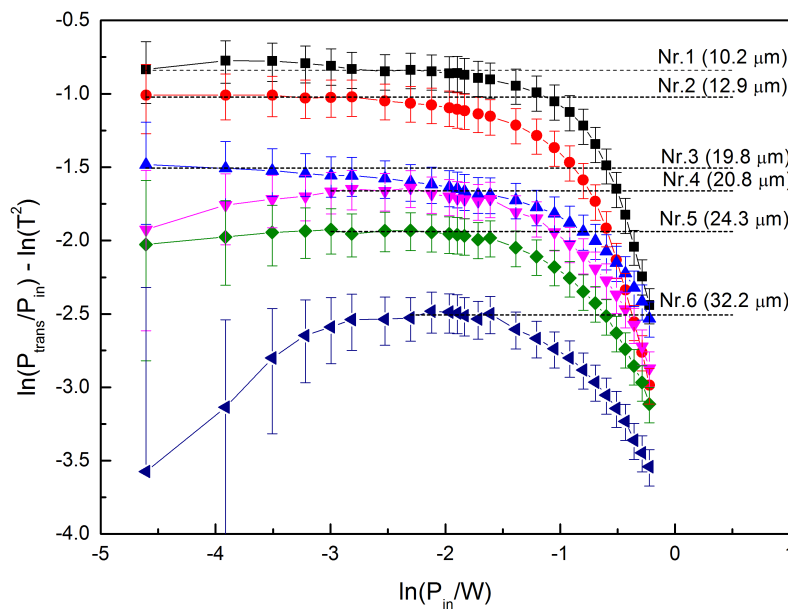


Figure 6.1: Plot of $\ln(P_{trans}/P_{in}) - \ln T^2 = -\alpha_1 z_m$ from Eq. (6.1.3) where $I(z = z_m)$ and $I_0 = I(z = 0)$ are the laser beam intensities at the rear and the front sides of the Si membrane as a function of the natural logarithm $\ln(P_{in})$ of the average laser power P_{in} incident onto the Si membranes.

incident power P_{in} , the $(-\alpha_1 z_m)$ -turn strongly negative due to FCA. The absorption coefficient α_1 covers a broad range of values i.e. $604 \text{ cm}^{-1} \leq \alpha_1 \leq 1100 \text{ cm}^{-1}$ [40, 181]. Green et al. [182] found that $\alpha_1 = 785 \text{ cm}^{-1}$. Table 6.1 lists values of $(\alpha_1 z_m)$ and the thickness d_i of the Si membranes obtained from the linear absorption regime (Beer's law) and the FCA model (see Eq. (6.1.12)). The z values of $(\alpha_1 z_m)_i^{lin}$ (where *lin* : linear) listed in Table 6.1 were obtained by averaging over the data points in the horizontal part of each curve in Fig. 6.1, with the standard deviation taken as the error. Values of d_i^{lin} were calculated using $\alpha_1 = 785 \pm 100 \text{ cm}^{-1}$; this measurement of the absorption coefficient value [182] appears to fit our model and calculations.

The thickness of the sample d_i was found from the experimentally determined $(\alpha_1 z_m)_i^{lin}$ product values of Fig. 6.1 using the relation

$$d_i = (\alpha_1 z_m)_i (\cos \gamma / \alpha_1). \quad (6.1.4)$$

Another term of $(\alpha_1 z_m)_i$ can be found from the expression $\exp(-\alpha_1 z_m)$ term in the FCA model (Eq. (6.1.9)) in section 6.1.2 and the related fit curve parameter F in Eq. (6.1.11). In Table 6.1, the values of d_i and $(\alpha_1 z_m)_i$

obtained using Beer's law are written as $d_i^{lin} (\alpha_1 z_m)_i^{lin}$ while d_i^{FCA} describe the thickness values of Si membranes extracted from the FCA model.

Table 6.1: Parameters ($\alpha_1 z_m$) and thickness d_i of the S_i membranes obtained from linear absorption regime (Beer's law, Fig. 5.5, index: *lin*) and the FCA model (Eqs. 5 and 7) used to fit the measurement point in Fig. 5.2 (with n taken as variable, index: *FCA, var*) and Fig. 5.3 (with $n = 2$ fixed, index: *FCA, fix*); d_{mean} is the average and Δd_{SD} is the standard deviation of the 3 values

Membrane number	$(\alpha_1 z_m)^{\text{lin}}$	d_i^{lin}	$d_i^{\text{FCA,fix}}$ [μm] ($n = 2$)	$d_i^{\text{FCA,var}}$ [μm] ($n = \text{variable}$)	n	$d_{\text{mean}} \pm \Delta d_{\text{SD}}$ [μm]
1	0.84 ± 0.04	10.5 ± 1.4	9.5 ± 1.9	10.7 ± 2.0	2.60 ± 0.05	10.2 ± 0.7
2	1.02 ± 0.01	12.8 ± 1.6	12.6 ± 2.1	13.5 ± 2.3	2.38 ± 0.05	12.9 ± 0.5
3	1.51 ± 0.02	18.8 ± 2.4	20.5 ± 3.0	20.0 ± 3.0	1.77 ± 0.04	19.8 ± 0.9
4	1.66 ± 0.01	20.8 ± 2.7	21.2 ± 3.1	20.5 ± 3.0	1.71 ± 0.05	20.8 ± 0.4
5	1.94 ± 0.01	24.2 ± 3.1	24.9 ± 3.5	24.0 ± 3.4	1.77 ± 0.03	24.3 ± 0.5
6	2.51 ± 0.02	31.3 ± 4.0	33.0 ± 4.5	32.3 ± 4.4	1.68 ± 0.07	32.2 ± 0.8

6.1.2 Free charge carrier absorption (FCA)

Let us consider that the effective absorption coefficient α_{eff} of the Si membrane consists of a linear, small signal absorption coefficient α_1 and the FCA contribution α_{FCA} :

$$\alpha_{eff} = \alpha_1 + \alpha_{FCA}, \quad (6.1.5)$$

Equation (6.1.1) becomes:

$$\begin{aligned} I(z_m, I_0) &= I_0 \exp(-\alpha_{eff} z_m) \\ &= I_0 \exp(-\alpha_1 z_m) \exp(-\alpha_{FCA} z_m), \end{aligned} \quad (6.1.6)$$

where z_m is laser beam path length through the Si membrane and is expressed by $z_m = d_{Si}/\cos \gamma$; with d_{Si} the thickness of the Si membranes.

In the laser irradiated volume, upon photon generation, the FCA coefficient α_{FCA} is related to the absorption cross section σ_{eh} and the density of electron-hole (eh) pairs n_{eh} ($n_{eh} = n_e = n_h$) by $\alpha_{FCA} = n_{eh}\sigma_{eh}$ [6, 9, 173].

The measured transmitted intensity $I(z_m)$ is related to the homogeneous stationary n_{eh} concentration and α_{FCA} value which is assumed to be z -independent. n_{eh} and α_{FCA} depend on the incident intensity I_0 i.e. $n_{eh} = n_{eh}(I_0)$ and $\alpha_{FCA} = \alpha_{FCA}(I_0)$. σ_{eh} also depends on n_{eh} [164, 175], i.e. $\sigma_{eh} = \sigma_{eh}(n_{eh}(I_0))$. Therefore, the absorption coefficient α_{FCA} is expressed as follows

$$\alpha_{FCA} \approx n_{eh}\sigma_{eh}(n_{eh}) \approx \sigma_0 n_{eh}^2 \approx \sigma_0 (\kappa I_0)^2 = \kappa_2 I_0^2, \quad (6.1.7)$$

with n_{eh} the density of eh pairs and $\sigma_{eh} \approx \sigma_0 n_{eh}$ [175]; thus $\kappa_2 = \sigma_0 \kappa^2$. The transmission of 800 nm fs laser light through thin Si samples is modeled as follows [10]:

$$I(z_m, I_0) = I_0 \exp(-\alpha_1 z_m) \quad \text{for } I_0 < I_c \quad (6.1.8a)$$

$$\begin{aligned} I(z_m, I_0) &= (I_0 - I_c) \exp(-\alpha_1 z_m) \exp(-\alpha_{FCA} z_m) \\ &\quad + I_c \exp(-\alpha_1 z_m) \quad \text{for } I_0 > I_c, \end{aligned} \quad (6.1.8b)$$

where I_c is interpreted as an I_0 threshold value below which eh pairs are generated, but do not contribute to FCA as shown in Fig. 6.2.

Taking into account Eq. (6.1.7), Eq. (6.1.8b) can be written as:

$$I(z_m, I_0) = (I_0 - I_c) \exp(-\alpha_1 z_m) \exp(-\kappa_2 I_0^2 z_m) + I_c \exp(-\alpha_1 z_m) \quad (6.1.9)$$

or in a more general way:

$$I(z_m, I_0) = (I_0 - I_c) \exp(-\alpha_1 z_m) \exp(-\kappa_n I_0^n z_m) + I_c \exp(-\alpha_1 z_m), \quad (6.1.10)$$

with $\kappa_{2,n}$ being the empirical constant and n a variable parameter. By considering the conversion of the intensities into the measured average powers defined in section 6.1.1, Eq. (6.1.10) becomes:

$$P_{trans}(z_m) = T^2 \exp(-\alpha_1 z_m) (P_{in} - I_c/(\eta T)) \exp(-\kappa_n (\eta P_{in} T)^n z_m) + T^2 \exp(-\alpha_1 z_m) I_c/(\eta T), \quad (6.1.11)$$

which can be simplified in the following form:

$$P_{trans}(z_m) = F [(P_{in} - C) \exp(-E_n P_{in}^n) + C]. \quad (6.1.12)$$

with $F = T^2 \exp(-\alpha_1 z_m)$, $C = I_c/(\eta T)$, $E_n = \kappa_n (\eta T)^n z_m$ and the scaling factor $\eta = 1.0 \times 10^{11} [\text{pulse.cm}^2]^{-1}$ [11].

Equation 6.1.12 is used to perform fitting of data obtained for the Si membrane thickness series of Fig. 5.2 (n considered as variable, and the fits are represented with solid lines(red)), and Fig. 5.3 (with n fixed to 2). The parameters from the fits are summarized in Table 6.2 [11].

Table 6.2: Fit parameters for the $P_{\text{trans}}(P_{\text{in}})$ traces in Fig. 5.2 and Fig. 5.3 obtained from Eq. (6.1.12). The parameter values for n are graphed in Fig. 6.3

Membrane number	n = variable			n = 2 fixed			
	F	E_n [W] ⁻ⁿ	C_n [mW]	n	F	E_2 [W] ⁻²	C_2 [mW]
1	0.303 ± 0.002	3.45 ± 0.24	52.8 ± 17	2.60 ± 0.05	0.334 ± 0.005	2.53 ± 0.05	≈ 0
2	0.243 ± 0.002	4.05 ± 0.28	46.9 ± 13	2.38 ± 0.06	0.261 ± 0.005	3.07 ± 0.04	≈ 0
3	0.144 ± 0.001	1.36 ± 0.01	≈ 0	1.77 ± 0.04	0.138 ± 0.0008	1.40 ± 0.02	≈ 0
4	0.139 ± 0.002	1.77 ± 0.02	≈ 0	1.71 ± 0.05	0.134 ± 0.001	1.85 ± 0.03	≈ 0
5	0.105 ± 0.002	2.00 ± 0.16	47.5 ± 33	1.77 ± 0.03	0.097 ± 0.001	2.92 ± 0.3	25 ± 290
6	0.054 ± 0.002	3.02 ± 0.54	237 ± 45	1.68 ± 0.07	0.051 ± 0.001	4.68 ± 0.06	22 ± 470

Results of the fit plots of Figs. 5.2 and 5.3 when using Eq. (6.1.12), for n considered as variable parameter and n fixed to 2, show similarities except for the two thinnest Si membranes (10.2 μm and 12.9 μm). From Tab. 6.2, $1.7 \leq n \leq 2.6$, i.e. $n = 2.1 \pm 0.6$ is close to the value $n = 2$. The F parameters obtained with n variable and $n = 2$ fixed are similar (with a maximum deviation of 10 %, membrane 1) and the values of E_n and C obtained from the fits are given in Tab. 6.2.

Figure 6.2 shows the deviation ΔI_{FCA} of the laser beam intensity transmitted through the thin Si membrane from the linear absorption signal (Beer's law). This deviation is attributed to FCA (as shown in Fig. 5.5). ΔI_{FCA} is given by [10, 11]:

$$\begin{aligned} \Delta I_{FCA} &= I^0(z_m, I_0) - I(z_m, I_0) \\ &= \eta P_{in} T \exp(-\alpha_1 z_m) - \eta P_{trans}/T \end{aligned} \quad (6.1.13)$$

with $\eta = 1.0 \times 10^{11} [\text{pulse.cm}^2]^{-1}$ being the constant scaling factor. Figure 6.2 shows that the square root of the deviation ΔI_{FCA} , after the threshold values, increases approximately linearly as the incident input power P_{in} is increased. The calculated FCA contribution depends, however, on the assumed linear absorption behavior, with respect to α_1 and z_m values.

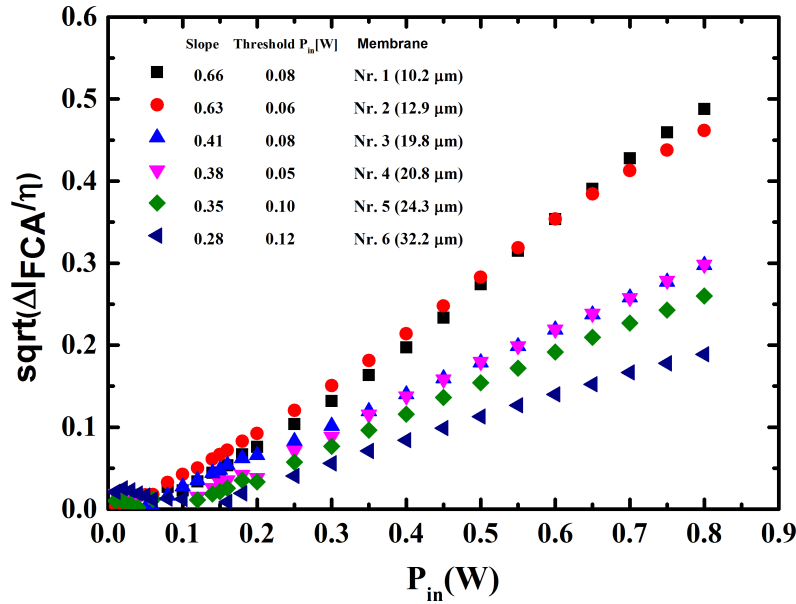


Figure 6.2: Square root of the deviation $\Delta I_{FCA}/\eta$ W of the measured transmission values from the ideal behavior of Beer's law (Eq. (6.1.13)) plotted versus the average laser power P_{in} [W] incident onto the Si membranes.

For simplicity Eq. (6.1.13) is divided by η and the FCA behavior ΔI_{FCA} is tested with $\sqrt{\Delta I_{FCA}/\eta}$ as shown in Fig. 6.2. It appears interesting to check the FCA behavior of ΔI_{FCA} with $\alpha_1 = 785 \pm 100 \text{ cm}^{-1}$ and the newly determined membrane thickness values from Table 6.1. From Fig. 6.2, the plot $\sqrt{\Delta I_{FCA}/\eta}$ appears to almost increase linearly with increasing input power P_{in} above a P_{in} threshold value, which depends on the membrane thickness. This result confirms previous results in [10] and confirms that n is close to 2. The slope of the linear parts $d(\sqrt{\Delta I_{FCA}/\eta})/dP_{in} = 1/\sqrt{\eta} \cdot d(\sqrt{\Delta I_{FCA}})/d(I_0/\eta T) = T\sqrt{\eta}d(\sqrt{\Delta I_{FCA}})/d(I_0)$ on the average decreases with increasing membrane thickness (see Figs. 6.2 and 6.3). The threshold on the P_{in} axis for the linear behavior is difficult to determine and the values given in Fig. 6.2 are rough estimates only. The dependence of the fitting parameters on the membrane thickness d is displayed in Fig. 6.3

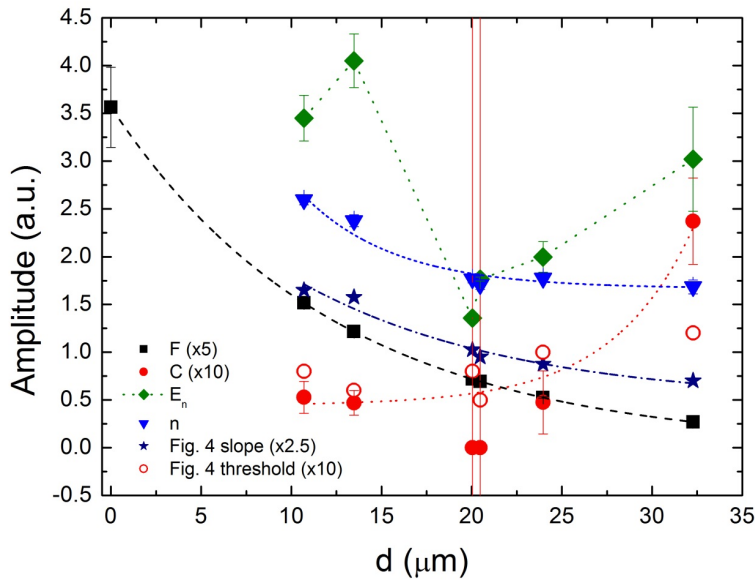


Figure 6.3: Fit parameters of the FCA model of Eq. (6.1.11) namely F (squares), E (diamonds), C (filled circles), n (triangles; from Table 6.2) and the slope of Fig. 6.2 (stars) and threshold values of Fig. 6.2 (empty circles) are graphed as a function of the membrane thickness d

The values of the parameter $F = T^2 \exp(-\alpha_1 z_m)$ in Eq. (6.1.12) show an exponential thickness dependence (as expected, since the d values on the x-axis have been obtained from the F parameter) [11]. The C values and the threshold values increase with membrane thickness (an exponential growth fitted to the C data is shown). The values of n decrease as d increases (an exponential decay fitted to the data is shown). The slope of the linear trace sections in Fig. 6.2 is also fitted well by an exponential decay, but it cannot be directly related to any single physical parameter. As for the E_i values no simple correlation with d is found. The variation of the fit parameters C_i , n ,

and the slope of Fig. 6.2 with membrane thickness d require a close look and their physical meaning has to be discussed.

The physical meaning of n is found in Eq. (6.1.7) and can be written in a general form given by

$$\alpha_{FCA} \approx n_{eh} \sigma_{eh}(n_{eh}) \approx \sigma_0 n_{eh}^n \approx \sigma_0 (\kappa I_0)^n = \kappa_n I_0^n. \quad (6.1.14)$$

The value n comes from the dependence of the absorption cross section σ_{eh} on the density n_{eh} of the eh pairs [10]:

$$\sigma_{eh} = \sigma_0 n_{eh}^{n-1}. \quad (6.1.15)$$

Thus, a change in the value of n corresponds to a change in the absorption cross section $\sigma_{eh}(n_{eh})$ of the eh pairs for a given eh pair density n_{eh} .

The value of C (equivalent to the threshold values in Fig. 6.2) is indicative of a constant amount of energy of each laser pulse that undergoes linear absorption, but does not contribute to FCA. The possible reasons for this phenomenon are (i) that part of the eh pairs are out of resonance with the incident laser photons and (ii) that the eh pairs that build up during the first and final parts of the laser pulse does not fully contribute to FCA. Reason (ii), however, is ruled out by previous observation on the same threshold behavior when a continuous laser beam is used [10].

6.2 Time-dependent second harmonic measurements

The time-dependent EFISH signals obtained in reflection from and transmission through the same silicon membrane selectively come from the front and rear Si/SiO₂ interfaces, respectively [40]. This can easily be rationalized by considering the effective susceptibility tensor of Eq. (3.5.4), which has two terms: the $\chi^{(2)}$ term, which is zero in the bulk centrosymmetric Si and non-zero at the Si/SiO₂ interface where symmetry is broken, and the $\chi^{(3)} E^{dc}(t)$ term which is non-zero in the Si as deep as the interface. The penetration depth depends on the doping concentration of the Si and was calculated to be 50 nm for our samples [40]. To a good approximation, the interfacial electric field can be assumed to be constant over the penetration depth; therefore the penetration depth will be the same for the front and rear Si/SiO₂ interfaces even if the magnitudes of the interfacial field at the two interfaces differs. In the absence of an electric field at the Si/SiO₂ interface, SHG occurs within a few atomic or surface monolayers of the Si [36, 183] because of symmetry breaking at the interface. This SH signal is very small compared to EFISH

signals which dominate in time-dependent measurements. In the presence of an electric field, the SH is enhanced by EFISH generated from the volume of Si penetrated by the interfacial electric field. EFISH from the Si/SiO₂ system is dominated by the contribution generated in the near-interface layer of Si rather than in the oxide [18] because of the spectroscopic evidence for the existence of energetic positions of SH resonances which match with the lowest direct energy gaps in Si [17, 184–186] and since $|\chi^{(3)}|$ is $\approx 10^4$ times smaller in SiO₂ than in Si. The EFISH signals measured are therefore generated in the Si within the penetration depth of the electric fields at each interface. The time-dependent EFISH signals during continuous illumination (as illustrated by Figs. 5.8 and 5.9) is due to the build up of a quasi-static interfacial electric field E^{dc} caused by transfer of electrons into the SiO₂ layer.

6.2.1 Second harmonic response of virgin bulk Si samples

The time-dependent SH signals shown in Fig. 5.6 and Fig. 5.7 reproduce previous work done in our laboratory [40, 41, 67, 68, 71, 150, 151] and by other research groups [18, 19, 22]. The discussion of these results will be based on previous interpretations. The measured SH traces are attributed to electron and hole effects. For electron effects, two processes are involved: electron injection and electron trap generation in the oxide layer. Electron processes are well established by second harmonic generation in Si [18, 19, 22, 38, 152, 153] and other methods such as tunneling microscopy [187, 188]. For hole effects, two processes are also involved: hole injection and a photoinduced generation of hole trap sites. A model [41] was developed to numerically fit the recorded data of Fig. 5.6 involving the dynamics of electrons and holes; this empirical model is given by:

$$I^{(2\omega)} \propto \left(1 + \sum_{i=1}^4 a_i \exp(-t/\tau_i) \right)^2, \quad (6.2.1)$$

with $a_1, a_2 < 0$, $a_3, a_4 > 0$ and $\tau_i > 0$.

The energy barrier for electron injection into SiO₂ (process 1) amounts to 4.3 eV [38] as shown in Fig. 3.5. Electrons surmount this barrier from the valence band (VB) of Si to the conduction band (CB) of SiO₂ by direct three-photon absorption or cascaded processes. Trapping occurs at the Si/air interface [19], in bulk SiO₂ or at the Si/SiO₂ interface [38]. Under illumination additional electron trap sites are created (process 2). These lead to a faster rise time in the SH response with pre-illuminated sample spots (Fig. 5.7). Hole injection (process 3) has an energy barrier of 5.7 eV [38] (Fig. 3.5) from the CB of Si to the VB of SiO₂ and requires a four-photon process, which becomes

significant at high peak intensities. For a given peak intensity, at first the efficiency of electrons is dominant in building up the interfacial electric field (increase in SH signal). The delayed contribution of the holes to the electric field is due to the slow generation of hole trap sites (process 4) [41]. As a result, the TDSH signal increase slows down, the signal reaches a maximum, and subsequently decreases very slowly as recorded in Fig. 5.6 and Fig. 5.7.

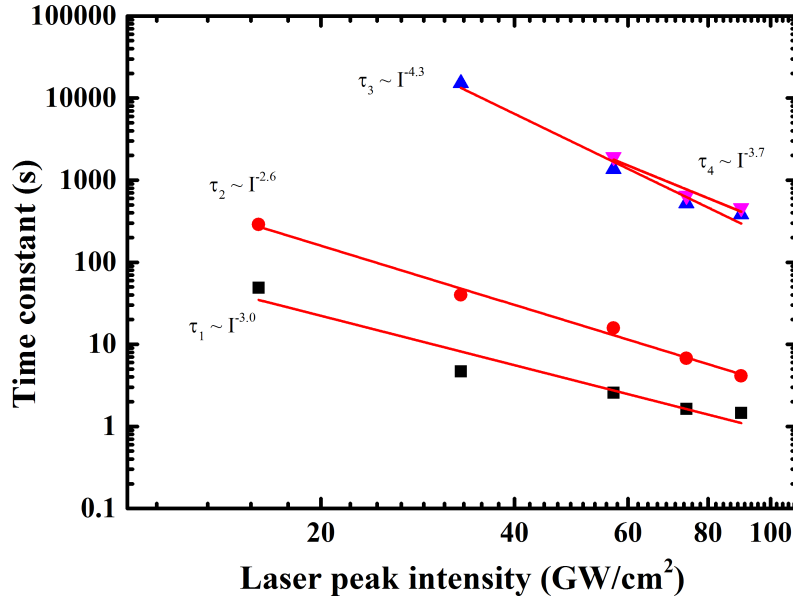


Figure 6.4: Time constants τ_i , $i = 1, 2, 3, 4$ extracted from the numerical fit of the data in Fig. 5.6 using Eq. (3.5.8) and Eq. (3.5.9), respectively.

Fig. 6.4 shows the time constants τ_i for electrons (processes 1 and 2) and holes (processes 2 and 4) in a double logarithmic plot. The values of τ_i extracted from the numerical fit of Fig. 5.6 using Eq. (6.4) are given in Table 6.3.

Table 6.3: Extracted time constants τ_i from numerical fits of Fig. 5.6 using Eq. 6.2.1

Intensity (GW/cm ²)	τ_1 (s)	τ_2 (s)	τ_3 (s)	τ_4 (s)
16	49.00	288.12		
33	4.66	39.92	15168.91	1.06×10^{21}
57	2.57	15.82	1368.93	1925.09
74	1.63	6.73	522.51	647.60
90	1.46	4.11	383.12	459.13

The time constants τ_i extracted from Fig. 6.4 depend on the incident laser peak intensity $I_{l,p}$ following the power law $1/\tau_i(I_{l,p}) \propto I_{l,p}^{n_i}$, with $n_1 = (3.0 \pm 0.3)$,

$n_2 = (2.6 \pm 0.1)$, $n_3 = (4.3 \pm 0.1)$ and $n_4 = (3.7 \pm 0.5)$. The n_i values obtained from the fits indicate that it requires two-, three- and four-photon absorption processes to transfer electrons and holes from Si to SiO₂. These values are in agreement with previously published results of $n_1 = (2.80 \pm 0.2)$, $n_2 = (2.5 \pm 0.3)$ [18] and $n_3 = 3.2$, $n_4 = 3.3$ [41]. Looking at the values of τ_i in Table 6.3, the time constant related to the electron contribution to the second harmonic evolution (τ_1 and τ_2) are approximately two orders of magnitude smaller than τ_3 and τ_4 , related to the hole contribution.

The SH signal after illumination interrupts from A to G (Fig. 5.7) increases rapidly. The amplitude of the SH increase depends on the duration of the dark period. The increase in amplitude of the SH signal is due to the superposition of opposing contributions from electrons and holes [41]. The maximum SH signal (net electric field) increase is observed for 600 s and is attributed to pure electron effects and the hole effect and is mainly attributed to the depopulation of hole trap sites under dark conditions.

The here obtained results with bulk Si show that the newly implemented experimental setup for simultaneous measurements of EFISH signals in transmission and reflection geometries is operating properly, since it was possible to reproduce previous work [41] done on bulk Si. It also shows that differences seen in the measurements from the membranes are due to the thickness.

6.2.2 Time-dependent second harmonic response of Si membrane samples

The time-dependent second harmonic (TDSH) for Si membranes are measured simultaneously in order to compare SH signals in reflection and transmission

6.2.2.1 TDSH in reflection geometry

For laser peak intensities $\leq 45.3 \text{ GW/cm}^2$, the temporal evolution of the experimental second harmonic results of Fig. 5.8 are reproduced using two exponential functions defined in Eq. (3.5.8) (electron effects):

$$I^{(2\omega)}(t) \propto [1 + a_1 \exp(-t/\tau_1) + a_2 \exp(-t/\tau_2)]^2, \quad (6.2.2)$$

with $a_i < 0$ and $\tau_i > 0$. For incident peak intensities $> 45.3 \text{ GW/cm}^2$, the temporal evolution of the SH response could not be explained only with electron effects. An additional effect was added to describe hole dynamics, which requires additional two exponential functions.

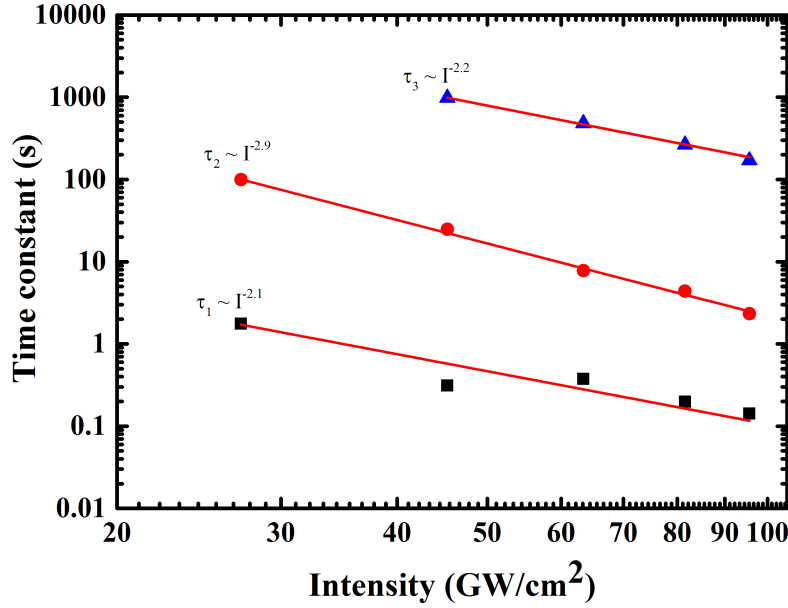


Figure 6.5: Time constants τ_i , $i = 1, 2, 3$, for reflection geometry, as a function of the incident intensities at the front Si/SiO_2 interface.

Usually, as discussed for the SH response of bulk Si, the equation describing hole and electron dynamics is given by Eq. (3.5.7):

$$I^{(2\omega)}(t) \propto \left(1 + \sum_{i=1}^4 a_i \exp(-t/\tau_i) \right)^2, \quad (6.2.3)$$

with a_i and τ_i the amplitudes and time constants of the SH signals with $a_1, a_2 < 0$; $a_3, a_4 > 0$ and $\tau_i > 0$. However, upon fitting the experimental data with Eq. (6.2.3), the time constant of the fourth exponential, τ_4 , gives an unrealistic value. The experimental data were then reproduced using three exponential functions defined as:

$$I^{(2\omega)}(t) \propto \left(1 + \sum_{i=1}^3 a_i \exp(-t/\tau_i) \right)^2, \quad (6.2.4)$$

where $a_1, a_2 < 0$; $a_3 > 0$ and $\tau_i > 0$. The time constants $\tau_i > 0$ are dependent on the incident laser peak intensity $I_{l,p}$ [19] and follow also the power law $1/\tau_i \propto I_{l,p}^{n_i}$. The extracted time constants are shown in Fig. 6.5. It shows the extracted time constant as a function of the incident laser peak intensities in a double logarithmic plot where the values are given in Table 6.4. The values of n_i extracted are $n_1 = 2.14 \pm 0.52$, $n_2 = 2.94 \pm 0.15$ and $n_3 = 2.28 \pm 0.07$.

Table 6.4: *Extracted time constants τ_i from numerical fits of Fig. 5.8 using Eq. (6.2.4)*

Intensity (GW/cm ²)	$\tau_1(s)$	$\tau_2(s)$	$\tau_3(s)$
27.2	1.76	100.04	
45.3	0.31	24.8	985.0
63.4	0.37	5.70	483.0
81.5	0.27	2.60	265.0
99.7	0.36	1.56	171.0

The obtained results from the membranes do not agree with the previously published model [41], three-exponents versus four-exponents [41]. This seems to indicate that the sample thickness plays a significant role in charge trapping and charge carrier dynamics. The interpretation of these results can be explained with laser irradiation which leads to electron injection and trapping in the ultrathin SiO₂ [39, 41] and to a permanent modification of the SH response due to photoinduced trap site creation. The superposition of electron and hole processes lead to a time-dependent EFISH signal. The energy barrier for electron injection into the SiO₂ amounts to 4.3 eV [41, 189]; the energy barrier for hole injection from Si to SiO₂ is 5.7 eV. Electrons surmount this interface by direct three-photon absorption or cascade processes. Hole injection requires a four-photon excitation process, which is significant at high incident intensities.

6.2.2.2 TDSH in transmission geometry

The time dependent SH signals shown in Fig. 5.9 are similar to the TDSH traces measured in reflection at low incident peak intensities in bulk Si (Fig. 5.6) with small differences in the rise time. The rise times of the SH signals of a Si membrane measured in transmission are longer compared to those measured in bulk Si. The SH signal increases over several minutes before reaching a steady state. The same explanation employed to explain the TDSH signal for bulk Si in Section 5.3.1 (at low peak intensities) can be applied here.

The time evolution of the SH signal measured in transmission is due to multiphoton injection of electrons from the valence band (VB) of Si to the conduction band (CB) of the SiO₂ at the rear Si/SiO₂ interface. This injection of electrons is done by direct three photon absorption process since the electrons have to surmount a barrier of 4.3 eV. As the irradiation continues, trap sites are created, thus trapping electrons. A steady state is reached at longer illumination times when the rate of populating or ionizing trap sites is equal to the detrapping rate. Hole dynamics do not play a role here, since a small amount of fundamental light reaches the rear Si/SiO₂ interface, thus small

peak intensities at the back SiO₂ interface. The experimental data of Fig. 5.9 were reproduced using Eq. (3.5.8) and subsequent time constants, τ_1 and τ_2 , were extracted.

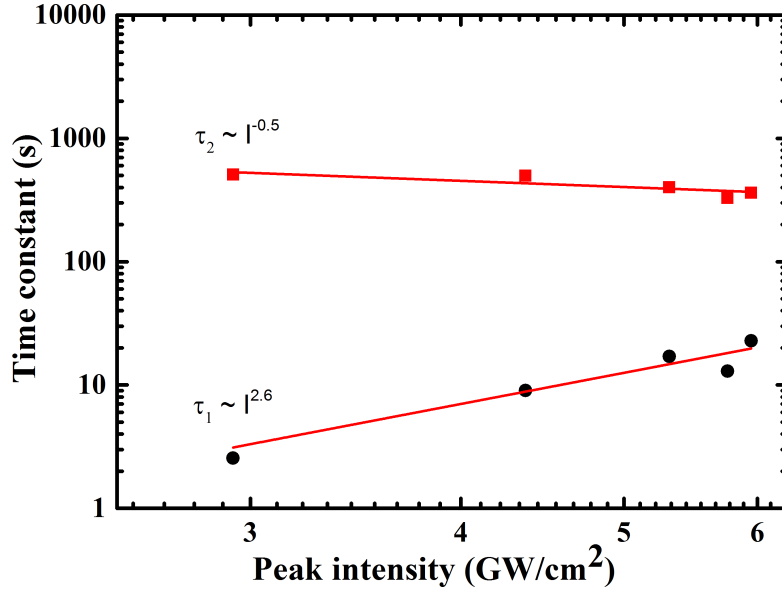


Figure 6.6: Time constants τ_i , $i = 1, 2$, for transmission geometry, as a function of the calculated intensities at the back Si/SiO₂ interface.

Fig. 6.6 shows the extracted time constants τ_1 and τ_2 of the SH transmission signals of Fig. 5.9 through a Si membrane in a double logarithmic plot. The extracted values of τ_1 and τ_2 from the numerical fit of Eq. (3.5.8) are given in Table 6.5. They are correlated to the laser peak intensity $I_{l,p}$ at the back Si/SiO₂ interface and do not follow a simple power law dependence on the incident intensity at the rear interface, as described in Section 6.2.1, with $n_1 = -2.6 \pm 1.1$ and $n_2 = 0.5 \pm 0.2$. The n_1 values obtained indicate that three absorption processes are required to transfer electrons from Si to the SiO₂. The intensities presented here are calculated by assuming that all the fundamental beam reaches the rear interface by applying Fresnel equations at air/SiO₂ and SiO₂/Si interfaces, respectively. The fundamental light reaching the rear interface contributes to the SH observed. These results seem to indicate that free carrier absorption (FCA) plays a significant role in the establishment of the interfacial electric field at the back Si/SiO₂ interface. Further investigations are necessary to pinpoint the role of FCA.

In our knowledge, simultaneous EFISH measurements in reflection and transmission from Si/SiO₂ interfaces of thin, free standing Si membranes were done (with balanced detectors), for the first time. EFISH signals in reflection and transmission originate from the front and rear Si/SiO₂ interfaces, respectively [40]. EFISH signals in reflection do not fit the existing model [41]; this seems

Table 6.5: *Extracted time constants τ_1 and τ_2 from numerical fits of Fig. 5.9 using Eq. 3.5.8*

Intensity (GW/cm ²)	τ_1 (s)	τ_2 (s)
2.93	2.55	509.0
4.37	9.02	498.0
5.32	17.0	400.0
5.76	12.9	329.0
5.95	22.8	362.0

to indicate that the sample thickness plays a significant role in charge trapping and charge carrier dynamics. The explanation is still unknown but the results do point to an effect which is a function of the sample thickness. The rise time and saturation values of the SH signals in reflection (5.10) and transmission (5.11) show remarkable differences.

6.2.3 Second harmonic response of pre-illuminated Si membrane samples

The temporal evolution of the SH signal obtained from pre-illuminated Si/SiO₂ of Si membranes shows an accelerated SH signal increase upon pre-illumination after dark periods from A to G in reflection geometry of Fig. 5.10. For laser peak intensity < 45 GW/cm², the SH signal recovers within seconds to its previous equilibrium level, as was reported previously by other authors [22, 41]. The magnitude of the enhanced SH signal amplitude increases with the duration of the dark period, up to 600 s. Even longer illumination interrupts have no additional effect. As for bulk Si, the SH amplitude increase is attributed to changes of the net electric field, being a superposition of contributions from both electrons and holes [41]. The maximum SH signal (net electric field) in reflection is observed after 600 s and is attributed to pure electron effects. The hole effect is reflected by the SH signal decrease and is attributed to hole trap generation [41]. Unlike in bulk Si samples, upon re-illumination the maximum SH signal is not that pronounced; this might be caused by other effects affecting the Si membrane such as free carrier absorption in the Si membrane. The accelerated electron and hole dynamics observed in pre-illuminated Si/SiO₂ of the Si membrane is explained by the photoinduced generation of electron and hole trap sites at the Si/SiO₂ interface under near infrared femtosecond laser illumination. To rationalize the accelerated electron and hole separation processes observed in pre-illuminated Si membrane samples, Scheidt in his PhD thesis [39] stipulated that there is a presence of a large density of photoinduced electron and hole traps in the Si/SiO₂ sample after re-illumination leading to accelerated charge carrier separation processes.

For transmission geometry (Fig. 5.11), the SH response of the Si/SiO₂ interface of the Si membrane after beam interrupts is similar to the SH response in reflection for bulk Si for peak intensities $< 45 \text{ GW/cm}^2$ in Fig. 5.10. After each interruption of the laser beam (A - G), the SH signal recovers within seconds to its previous equilibrium level. The measured time evolution is due to multiphoton injection of electrons at the rear interface from Si into the SiO₂ by direct three-photon absorption processes to surmount a barrier of 4.3 eV. Hole effects do not play a role in SH signals in transmission since little intensity reaches the rear interface.

In summary, for both bulk Si and Si membranes, the SH signals increase on a time scale of minutes for low peak intensities and are faster for high peak intensities. For high peak intensities, upon re-irradiation the SH intensity increases above the level before the dark period from A - G but are less than the initial SH intensity upon onset of laser irradiation; the decline after each new SH signal occurs in significantly shorter period than the slow decline after the initial maximum of the virgin spot. The amplitudes of the SH increase depends on the duration of the dark period and the maximum SH signal increase is observed after 600 s of dark period. The amplitudes upon onset of laser illumination are less in bulk Si (5.7) than in Si membranes (5.10) and the SH amplitudes after dark periods are more pronounced in bulk Si than in silicon membranes.

6.2.4 Comparison between TDSH in transmission and reflection

A comparison of the SH signals measured in transmission and reflection was done simultaneously with balanced detectors and the result is shown in Fig. 6.7 which shows the time evolution SH signals measured in transmission (5.92 GW/cm^2) and reflection (7.25 GW/cm^2) geometries as a function of the illumination time.

The comparison of SH signals was done on a virgin sample spot in such a way that the highest measured SH signal in transmission (5.92 GW/cm^2) be compared approximately with the same incident peak intensity in reflection (7.25 GW/cm^2). The experimental results displayed in Fig. 6.7 show that, throughout the beam exposure, the recorded SH signal in transmission is higher than the SH signal recorded in reflection. The time constants extracted from the experimental data, by fitting with two exponential functions defined in Eq. (3.5.8) are given in Table 6.6. The rise time of the SH signal in transmission is longer than the rise time of the SH signal in reflection. These results are similar to those obtained previously [40]. The signal increase originates from the build-up of the photoinduced interfacial electric fields [40, 41] and the time constants τ_1 and τ_2 correspond to the processes of electron injection into the oxide and electron trap generation in the oxide, respectively [18, 40].

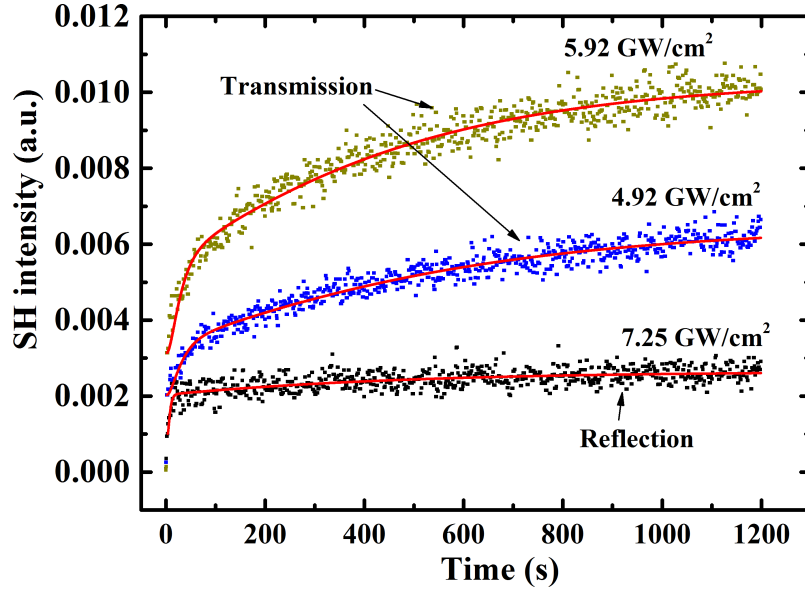


Figure 6.7: Time dependent SH signals measured in transmission at a calculated peak intensity of 4.92 GW/cm^2 , 5.92 GW/cm^2 and in reflection at an incident (behind Si/SiO_2 interface) peak intensity of 7.25 GW/cm^2 . Solid curves are fits according to Eq. (3.5.8).

Table 6.6: Extracted time constants τ_1 and τ_2 from numerical data fit of Fig. 6.7 using Eq. 3.5.8 to compare the TDSH in transmission and in reflection

	Intensity (GW/cm^2)	a_1	a_2	τ_1 (s)	τ_2 (s)
Transmission	4.92	-0.54	-0.46	21.0	477.0
Transmission	5.92	-0.57	-0.43	19.7	398.0
Reflection	7.25	-0.79	-0.21	3.57	430.0

It was suggested [40] that the fast signal rise time and the higher SH amplitude observed in transmission may be related to the dynamics of build-up of the interfacial electric field at the rear interface of the Si membrane.

Chapter 7

Summary, conclusion and outlook

Summary and conclusion

The incidence of a Ti:sapphire fs laser beam ($\lambda = 800$ nm, 90 fs and 80 MHz repetition rate) is used to irradiate weakly doped silicon membranes using the newly developed and implemented experimental setup.

The fs Ti:sapphire laser is applied to investigate the linear and nonlinear optical behavior of thin Si membrane samples in the $10 \mu\text{m}$ to $30 \mu\text{m}$ thickness range by measuring the average laser power transmitted through and reflected from the membranes as a function of the incident laser power. The average laser power incident onto the membranes was increased up to 0.8 W. This variation revealed a strong nonlinear power dependence of the beam transmission through the samples whereas the laser beam reflection remained a linear function. The linear part of the transmitted signal through the Si membranes was used to optically determine the membrane thickness d by two ways, using either the linear absorption regime at low laser power (Beer's law) or the related fit parameters of the applied FCA model (Eq. (6.1.12)). Both ways lead to approximately identical results with a standard deviation $\Delta d_{SD} < 1 \mu\text{m}$ for a given value of the linear absorption coefficient α_1 , where $\alpha_1 = 785 \text{ cm}^{-1}$ appears most reliable within the $600 \text{ cm}^{-1} \leq \alpha_1 \leq 1200 \text{ cm}^{-1}$ literature value range.

The nonlinearity observed for the transmitted laser beam is mainly attributed to free charge carrier absorption (FCA) in silicon and quantitatively reproduced by a recently derived FCA model [10]. The model uses an effective absorption coefficient $\alpha_{eff} = \alpha_1 + \alpha_{FCA}$ with α_{FCA} increasing quadratically with the average laser intensity (input power): $\alpha_{FCA} = \kappa_n I_0^n$ with $n = 2$. The FCA model with its empirical fit parameters allows quantitative calculations of the transmission behavior of Si membranes within the investigated sample thickness, doping and laser power (intensity) regimes.

In order to test the newly implemented experimental setup, another aspect of the nonlinear properties of Si was also investigated: the time-dependent second harmonic (TDSH) of the electric field induced second harmonic (EFISH) signals were measured. Firstly the TDSH signals of virgin bulk Si samples were measured and the results obtained were similar to previous work done [41]. The results are interpreted by photoinduced electron and hole injection and trapping in the ultrathin SiO₂ contributing to the EFISH response of Si/SiO₂. At higher input intensity regimes, not only electrons are transferred from the silicon into the SiO₂ conduction band via three-photon excitation, but also holes are transferred across the interface into the SiO₂ valence band following four-photon excitation. The temporal SH evolution signal is reproduced by an empirical numerical model involving the superposition of opposing electron and hole contributions to the interfacial SH response. The extracted time constant obtained followed a power law dependence $1/\tau_i \propto I^{n_i}$ and are in good agreement with the literature values [41].

The TDSH signals upon beam interrupt show different behavior compared to those measured with virgin bulk Si. Upon re-illumination with identical parameters, both electron as well as hole effects take place on a considerably shortened time scale after dark periods of 10 to 600 s. The charge carrier relaxation behavior under dark conditions shows an enhanced maximum SH signal immediately upon re-illumination, the amplitude depending on the duration of the preceding dark period and saturating times for ≥ 600 s. This enhancement as a function of dark time follows a simple exponential function and is attributed to the depopulation of hole trap sites.

Using the information obtained from SHG experiments on virgin bulk Si/SiO₂ interface, simultaneous measurements of the EFISH signals in transmission through and reflection from thin Si membranes were performed for the "*first time*". The magnitudes of the SH signal from Si membranes were measured in transmission and reflection geometries at different incident laser intensities. The temporal evolution of the SH signals obtained from Si membranes shows similar results as that obtained with bulk Si, i.e, the trend lines of SH signals obtained in transmission with Si membranes follow the same trend as for those obtained with bulk Si in reflection at low peak intensities [41] and are reproduced by the empirical numerical model involving electron and hole effects in order to reproduce the experimental data. The time constants were extracted. The SH yield intensity as a function of the incident intensity at the Si/SiO₂ interface in transmission reveals an increase of the SH signal up to a maximum value, and then decreases again for increased input intensities. It exhibits a similar behavior like that for the transmitted laser beam through the Si membrane. The nonlinearity of the transmitted SH responses still are not yet well understood. Thus there is a need for further experimental investigations and a well defined SH model for Si.

A comparison of the SH signals in transmission and reflection shows that SH signal measured in transmission geometry is higher than SH signal measured in reflection. This result confirms earlier observation done in our laboratory [40]. We still are not able to find or devise a proper model capable of explaining why the EFISH signal in transmission geometry is higher than the EFISH signal measured in reflection for the same incident intensity.

Outlook

The work done in this thesis contributes to the continuing need of understanding the Si/SiO₂ system. Based on the experimentally obtained results, this work opens up a variety of new questions and ideas for further investigations of Si. These refer to the understanding of the FCA in Si under 800 nm illumination. The sample thickness shall cover the full range from the absorption length of the fundamental laser beam of about 10 μm down to the technically achievable minimum thickness of thin crystalline films on the 100 nm scale. These thicknesses range from several wavelengths of the fundamental laser beam (0.8 μm) down to a fraction of the fundamental and frequency doubled laser beams. With shrinking sample thickness, optical interference will play an increasing role in signal formation and provide additional valuable information about the inherent processes and sample properties on the nanometer scales.

Another challenge is to further develop a proper Si model for SH in transmission and reflection geometries, respectively, to precisely determine the mechanisms of charge transfer at the front and rear Si/SiO₂ of thin silicon membranes. Further experimental investigations such as the investigation of the temporal SH response using different polarization combinations. The dynamics of the EFISH process may be investigated by setting up a pump-probe setup to measure the time evolution of the interfacial electric field on short time scales for samples with different doping concentration. The mechanism of defect creation and charge trapping in transmission can be further be explored by using vacuum ultraviolet (VUV) light sources to create defects and probe these defects using the femtosecond light source.

List of References

- [1] Neethling Pieter Herman. *Electric field induced second harmonic (EFISH) measurements of highly boron doped p-type Si/SiO₂*. PhD thesis, Stellenbosch University, December 2008.
- [2] X.C. Tong. *Advanced Materials for Integrated Optical Waveguides*. Springer Series in Advanced Microelectronics. Springer International Publishing, 2013.
- [3] C. R. Helms and E H Poindexter. The silicon-silicon dioxide system: its microstructure and imperfections. *Reports on Progress in Physics*, 57(8):791, 1994.
- [4] G. Lüpke. Characterization of semiconductor interfaces by second-harmonic generation. *Surface Science Reports*, 35(3–4):75–161, 1999.
- [5] Zhong-Yi Lu, C. J. Nicklaw, D. M. Fleetwood, R. D. Schrimpf, and S. T. Pantelides. Structure, properties, and dynamics of oxygen vacancies in amorphous si_o₂. *Phys. Rev. Lett.*, 89:285505, Dec 2002.
- [6] J. M. Moison, F. Barthe, and M. Bensoussan. Laser-induced nonlinear absorption in silicon: Free-carrier absorption versus thermal effects. *Phys. Rev. B*, 27:3611–3619, Mar 1983.
- [7] H. B. Briggs and R. C. Fletcher. Absorption of infrared light by free carriers in germanium. *Phys. Rev.*, 91:1342–1346, Sep 1953.
- [8] Masayoshi Yamada, Hisakazu Kotani, Keiichi Yamamoto, and Kenji Abe. Non-linear transmission of intense laser pulse in silicon-on-sapphire. *Physics Letters A*, 85(3):191 – 194, 1981.
- [9] Rohan D. Kekatpure and Mark L. Brongersma. Quantification of free-carrier absorption in silicon nanocrystals with an optical microcavity. *Nano Letters*, 8(11):3787–3793, 2008.
- [10] P. C Heisel, W. I. Ndebeka, P. H. Neethling, W. Paa, C. M. Steenkamp, Rohwer E.G., and Stafast H. Free charge carrier absorption in silicon at 800 nm. *Appl. Phys. B: Lasers and Optics*, 122:60(3), March 2016.
- [11] W.I. Ndebeka, P.H. Neethling, C.M. Steenkamp J. Bergmann, E.G. Rohwer, and H. Stafast. Interband and free charge carrier absorption in silicon at 800 nm: experiment and model calculations. *Manuscript submitted*, Sept 2016.

- [12] W. Daum, H. J. Krause, U. Reichel, and H. Ibach. Identification of strained silicon layers at Si-SiO₂ interfaces and clean Si surfaces by nonlinear optical spectroscopy. *Phys. Rev. Lett.*, 71:1234–1237, Aug 1993.
- [13] G. Lüpke, D. J. Bottomley, and H. M. van Driel. SiO₂/Si interfacial structure on vicinal Si(100) studied with second-harmonic. *Phys. Rev. B*, 47:10389–10394, Apr 1993.
- [14] G. Lüpke, C. Meyer, U. Emmerichs, F. Wolter, and H. Kurz. Influence of Si-O bonding arrangements at kinks on second-harmonic generation from vicinal Si(111) surfaces. *Phys. Rev. B*, 50:17292–17297, Dec 1994.
- [15] J.I. Dadap, X.F. Hu, M. Russell, J.G. Ekerdt, J.K. Lowell, and M.C. Downer. Analysis of second-harmonic generation by unamplified, high-repetition-rate, ultrashort laser pulses at Si(001) interfaces. *Selected Topics in Quantum Electronics, IEEE Journal of*, 1(4):1145–1155, dec 1995.
- [16] C. W. van Hasselt, M. A. C. Devillers, Th. Rasing, and O. A. Aktsipetrov. Second-harmonic generation from thick thermal oxides on Si(111): the influence of multiple reflections. *J. Opt. Soc. Am. B*, 12(1):33–36, Jan 1995.
- [17] C. Meyer, G. Lüpke, U. Emmerichs, F. Wolter, H. Kurz, C. H. Bjorkman, and G. Lucovsky. Electronic transitions at Si(111)/SiO₂ and Si(111)/Si₃N₄ interfaces studied by optical second-harmonic spectroscopy. *Phys. Rev. Lett.*, 74:3001–3004, Apr 1995.
- [18] J. G. Mihaychuk, J. Bloch, Y. Liu, and H. M. vanDriel. Time-dependent second harmonic generation from the Si–SiO₂ interface induced by charge transfer. *Opt. Lett.*, 20(20):2063 – 2065, Oct 1995.
- [19] J. Bloch, J. G. Mihaychuk, and H. M. van Driel. Electron photoinjection from silicon to ultrathin SiO₂ films via ambient oxygen. *Phys. Rev. Lett.*, 77:920–923, Jul 1996.
- [20] N. Shamir, J. G. Mihaychuk, and H. M. van Driel. Transient charging and slow trapping in ultrathin SiO₂ films on si during electron bombardment. *Journal of Vacuum Science & Technology A*, 15(4):2081–2084, 1997.
- [21] O. Aktsipetrov, A. Fedyanin, E. Mishina, A. Nikulin, A. Rubtsov, C. van Hasselt, M. Devillers, and Th. Rasing. Macroscopic size effects in second harmonic generation from Si(111) coated by thin oxide films: The role of optical casimir nonlocality. *Phys. Rev. Lett.*, 78:46–49, Jan 1997.
- [22] M. Cernusca, R. Heer, and G.A. Reider. Photoinduced trap generation at the Si-SiO₂ interface. *Applied Physics B: Lasers & Optics*, 66(3):367, 1998.
- [23] O. A. Aktsipetrov, A. A. Fedyanin, E. D. Mishina, A. N. Rubtsov, C. W. van Hasselt, M. A. C. Devillers, and Th. Rasing. dc-electric-field-induced second-harmonic generation in Si(111)-SiO₂-Cr metal-oxide-semiconductor structures. *Phys. Rev. B*, 54:1825–1832, Jul 1996.

- [24] J. I. Dadap, X. F. Hu, M. H. Anderson, M. C. Downer, J. K. Lowell, and O. A. Aktsipetrov. Optical second-harmonic electroreflectance spectroscopy of a Si(001) metal-oxide-semiconductor structure. *Phys. Rev. B*, 53:R7607–R7609, Mar 1996.
- [25] P. Godefroy and W. de Jong. Electric field induced second harmonic generation spectroscopy on a metal-oxide-silicon structure. *Applied Physics Letters*, 68(14):1981, 1996.
- [26] Ajay Nahata, Tony F. Heinz, and James A. Misewich. High-speed electrical sampling using optical second-harmonic generation. *Applied Physics Letters*, 69(6):746–748, 1996.
- [27] C. Ohlhoff, C. Meyer, G. Lüpke, T. Löffler, T. Pfeifer, H. G. Roskos, and H. Kurz. Optical second-harmonic probe for silicon millimeter-wave circuits. *Applied Physics Letters*, 68(12):1699–1701, 1996.
- [28] C. Ohlhoff, G. Lüpke, C. Meyer, and H. Kurz. Static and high-frequency electric fields in silicon MOS and MS structures probed by optical second-harmonic generation. *Phys. Rev. B*, 55:4596–4606, Feb 1997.
- [29] J. E. Sipe, D. J. Moss, and H. M. van Driel. Phenomenological theory of optical second- and third-harmonic generation from cubic centrosymmetric crystals. *Phys. Rev. B*, 35:1129–1141, Jan 1987.
- [30] G.L. Richmond, J.M. Robinson, and V.L. Shannon. Second harmonic generation studies of interfacial structure and dynamics. *Progress in Surface Science*, 28(1):1–70, 1988.
- [31] T. Heinz, F. Himpsel, E. Palange, and E. Burstein. Electronic transitions at the CaF/Si(111) interface probed by resonant three-wave mixing spectroscopy. *Phys. Rev. Lett.*, 63:644–647, Aug 1989.
- [32] C. van Hasselt, M. Verheijen, and Th. Rasing. Vicinal Si(111) surfaces studied by optical second-harmonic generation: Step-induced anisotropy and surface-bulk discrimination. *Phys. Rev. B*, 42:9263–9266, Nov 1990.
- [33] C. H. Bjorkman, C. E. Shearon, Y. Ma, T. Yasuda, G. Lucovsky, U. Emmerichs, C. Meyer, K. Leo, and H. Kurz. Second-harmonic generation in Si-SiO₂ heterostructures formed by chemical, thermal, and plasma-assisted oxidation and deposition processes. *Journal of Vacuum Science & Technology A*, 11(4):964–970, 1993.
- [34] O. A. Aktsipetrov, A. A. Fedyanin, V. N. Golovkina, and T. V. Murzina. Optical second-harmonic generation induced by a dc electric field at the Si/SiO₂ interface. *Opt. Lett.*, 19(18):1450–1452, Sep 1994.
- [35] G. Lüpke, D. J. Bottomley, and H. M. van Driel. Second- and third-harmonic generation from cubic centrosymmetric crystals with vicinal faces: phenomenological theory and experiment. *J. Opt. Soc. Am. B*, 11(1):33–44, Jan 1994.

- [36] Robert M. Corn and Daniel A. Higgins. Optical second harmonic generation as a probe of surface chemistry. *Chemical Reviews*, 94(1):107–125, 1994.
- [37] J.I. Dadap and B. Doris. Randomly oriented angstrom-scale microroughness at the Si(100)/SiO₂ interface probed by optical second harmonic generation. *Applied Physics Letters*, 64(16):2139, 1994.
- [38] J. G. Mihaychuk, N. Shamir, and H. M. van Driel. Multiphoton photoemission and electric-field-induced optical second-harmonic generation as probes of charge transfer across the Si/SiO₂ interface. *Phys. Rev. B*, 59:2164–2173, Jan 1999.
- [39] T. Scheidt. Charge Carrier Dynamics and Defect Generation at the Si/SiO₂ Interface Probed by Femtosecond Optical Second Harmonic Generation. PhD thesis, Friedrich-Schiller University Jena- Germany, 2005.
- [40] G. Nyamuda, E. Rohwer, C. Steenkamp, and H. Stafast. First comparison of electric field induced second harmonic of near-infrared femtosecond laser pulses in reflection and transmission generated from Si/SiO₂ interfaces of a silicon membrane. *Applied Physics B: Lasers and Optics*, 104:735–740, 2011. 10.1007/s00340-011-4682-1.
- [41] T. Scheidt, E. G. Rohwer, H. M. von Bergmann, and H. Stafast. Charge-carrier dynamics and trap generation in native Si/SiO₂ interfaces probed by optical second-harmonic generation. *Phys. Rev. B*, 69:165314, Apr 2004.
- [42] C. Logofatu, C. C. Negrila, R. V. Ghita, F. Ungureanu, C. Cotirlan, C. G. A. S. Manea, and M. F. Lazarescu. Study of SiO₂/Si interface by surface techniques. *Intech*, pages 24–42, 2011.
- [43] M. F. Chung and D. Haneman. Properties of clean silicon surfaces by paramagnetic resonance. *Journal of Applied Physics*, 37(4):1879–1889, 1966.
- [44] Akos G. Revesz and Bernard Goldstein. Electron paramagnetic resonance investigation of the Si-SiO₂ interface. *Surface Science*, 14(2):361 – 374, 1969.
- [45] P. A. Franken, A. E. Hill, C. W. Peters, and G. Weinreich. Generation of optical harmonics. *Phys. Rev. Lett.*, 7:118–119, Aug 1961.
- [46] N. Bloembergen and Y. R. Shen. Optical nonlinearities of a plasma. *Phys. Rev.*, 141:298–305, Jan 1966.
- [47] N. Bloembergen, R. K. Chang, S. S. Jha, and C. H. Lee. Optical second-harmonic generation in reflection from media with inversion symmetry. *Phys. Rev.*, 174:813–822, Oct 1968.
- [48] Fielding Brown and Robert E. Parks. Magnetic-dipole contribution to optical harmonics in silver. *Phys. Rev. Lett.*, 16:507–509, Mar 1966.

- [49] T. F. Heinz, C. K. Chen, D. Ricard, and Y. R. Shen. Spectroscopy of molecular monolayers by resonant second-harmonic generation. *Phys. Rev. Lett.*, 48:478–481, Feb 1982.
- [50] H. W. K. Tom, T. F. Heinz, and Y. R. Shen. Second-harmonic reflection from silicon surfaces and its relation to structural symmetry. *Phys. Rev. Lett.*, 51:1983–1986, Nov 1983.
- [51] T. F. Heinz, M. M. T. Loy, and W. A. Thompson. Study of Si(111) surfaces by optical second-harmonic generation: Reconstruction and surface phase transformation. *Phys. Rev. Lett.*, 54:63–66, Jan 1985.
- [52] S. T. Cundiff, W. H. Knox, F. H. Baumann, K. W. Evans-Lutterodt, and M. L. Green. Second-harmonic generation at the interface between Si(100) and thin SiO₂ layers. *Journal of Vacuum Science & Technology A*, 16(3):1730–1734, 1998.
- [53] D. Schuhmacher, G. Marowsky, A.A. Fedyanin, T.V. Dolgova, and O.A. Akt-sipetrov. Probe of the vicinal Si(111) surface by second harmonic phase spectroscopy. *Materials Science in Semiconductor Processing*, 4(1–3):51 – 53, 2001. Advanced Characterisation of Semiconductor Materials.
- [54] C. H. Bjorkman, T. Yasuda, C. E. Shearon, Y. Ma, G. Lucovsky, U. Emmerichs, C. Meyer, K. Leo, and H. Kurz. Influence of surface roughness on the electrical properties of Si-SiO₂ interfaces and on second-harmonic generation at these interfaces. *Journal of Vacuum Science & Technology B*, 11(4):1521–1527, 1993.
- [55] S. T. Cundiff, W. H. Knox, F. H. Baumann, K. W. Evans-Lutterodt, M. T. Tang, M. L. Green, and H. M. Van Driel. Si/SiO₂ interface roughness: Comparison between surface second harmonic generation and x-ray scattering. *Applied Physics Letters*, 70(11):1414–1416, 3 1997.
- [56] M.A. Verheijen, C.W. van Hasselt, and Th. Rasing. Optical second harmonic generation study of vicinal Si(111) surfaces. *Surface Science*, 251:467 – 471, 1991.
- [57] S. A. Mitchell, T. R. Ward, D. D. M. Wayner, and G. P. Lopinski. Charge trapping at chemically modified Si(111) surfaces studied by optical second harmonic generation. *The Journal of Physical Chemistry B*, 106(38):9873–9882, 2002.
- [58] S. Bergfeld, B. Braunschweig, and W. Daum. Nonlinear optical spectroscopy of suboxides at oxidized Si(111) interfaces. *Phys. Rev. Lett.*, 93:097402, Aug 2004.
- [59] U. Emmerichs, C. Meyer, H. J. Bakker, F. Wolter, H. Kurz, G. Lucovsky, C. E. Bjorkman, T. Yasuda, Yi Ma, Z. Jing, and J. L. Whitten. Optical second harmonic generation: A probe of atomic structure and bonding at Si-SiO₂ interfaces, and other chemically modified si surfaces. *Journal of Vacuum Science & Technology B*, 12(4):2484–2492, 1994.

- [60] U. Emmerichs, C. Meyer, H. Bakker, H. Kurz, C. Bjorkman, C. Shearon, Y. Ma, T. Yasuda, Z. Jing, G. Lucovsky, and J. Whitten. Second-harmonic response of chemically modified vicinal Si(111) surfaces. *Phys. Rev. B*, 50:5506–5511, Aug 1994.
- [61] Hiroyuki Hirayama, Fuminori Ito, and Kohji Watanabe. Effect of hydrogen annealing on second-harmonic generation from SiO₂/Si(111) interfaces. *Journal of Vacuum Science & Technology A*, 13(3):750–752, 1995.
- [62] S. A. Mitchell, R. Boukherroub, and S. Anderson. Second harmonic generation at chemically modified Si(111) surfaces. *The Journal of Physical Chemistry B*, 104(32):7668–7676, 2000.
- [63] Fuminori Ito and Hiroyuki Hirayama. Second-harmonic generation from SiO₂/Si(111) interfaces. *Phys. Rev. B*, 50:11208–11211, Oct 1994.
- [64] C.W. van Hasselt, E. Mateman, M.A.C. Devillers, Th. Rasing, A.A. Fedyanin, E.D. Mishina, O.A. Aktsipetrov, and J.C. Jans. Oxide-thickness dependence of second harmonic generation from thick thermal oxides on Si(111). *Surface Science*, 331:1367 – 1371, 1995.
- [65] Y R Shen. Optical second harmonic generation at interfaces. *Annual Review of Physical Chemistry*, 40(1):327–350, 1989.
- [66] O.A. Aktsipetrov, A.A. Fedyanin, E.D. Mishina, A.N. Rubtsov, C.W. van Hasselt, M.A.C. Devillers, and Th. Rasing. Probing the silicon-silicon oxide interface of Si(111)-SiO₂-Cr {MOS} structures by dc-electric field-induced second harmonic generation. *Surface Science*, 352–354:1033–1037, 1996. Proceedings of the 15th European Conference on Surface Science.
- [67] T. Scheidt, E. G. Rohwer, H. M. von Bergmann, and H. Stafast. Optical second harmonic imaging of zinc oxide thin films grown by metal organic chemical vapour deposition (MOCVD). *physica status solidi (c)*, 1(9):2243–2249, 2004.
- [68] T. Scheidt, E. G. Rohwer, H. M. von Bergmann, E. Saucedo, E. Diéguez, L. Fornaro, and H. Stafast. Optical second-harmonic imaging of Pb_xCd_{1-x}Te ternary alloys. *American Institute of Physics*, 97:103104, 2005.
- [69] T. Scheidt, E. G. Rohwer, H. M. von Bergmann, and H. Stafast. Ultraviolet pulse laser induced modifications of native silicon/silica interfaces analyzed by optical second harmonic generation. *Journal of Applied Physics*, 100:023118, 2006.
- [70] T. Scheidt, E. G. Rohwer, P. Neethling, H. M. von Bergmann, and H. Stafast. Ionization and shielding of interface states in native p⁺-Si/SiO₂ probed by electric field induced second harmonic generation. *Journal of Applied Physics*, 104(8):083712–083712–8, oct 2008.
- [71] P. H. Neethling, E. G. Rohwer, H. M. Von Bergmann, and H. Stafast. Analysis of ZnO thin films by second harmonic generation. *physica status solidi (c)*, 5(2):552–554, 2008.

- [72] H. Park, J. Qi, Y. Xu, K. Varga, S. M. Weiss, B. R. Rogers, G. Lüpke, and N. Tolk. Characterization of boron charge traps at the interface of Si/SiO₂ using second harmonic generation. *Applied Physics Letters*, 95(6):062102, 2009.
- [73] Heungman Park, Jingbo Qi, Ying Xu, Kalman Varga, Sharon M. Weiss, Bridget R. Rogers, Gunter Lüpke, and Norman Tolk. Boron induced charge traps near the interface of Si/SiO₂ probed by second harmonic generation. *physica status solidi (b)*, 247(8):1997–2001, 2010.
- [74] Julie L. Fiore, Vasiliy V. Fomenko, Dora Bodlaki, and Eric Borguet. Second harmonic generation probing of dopant type and density at the Si/SiO₂ interface. *Applied Physics Letters*, 98(4), 2011.
- [75] M. Cazzanelli, F. Bianco, E. Borga, G. Pucker, M. Ghulinyan, E. Degoli, E. Luppi, V. Véniard, S. Ossicini, D. Modotto, S. Wabnitz, R. Pierobon, and L. Pavesi. Second-harmonic generation in silicon waveguides strained by silicon nitride. *Nat Mater*, 11:148 – 154, 02 2012.
- [76] Akihiro Kitao, Kenji Imakita, Ibuki Kawamura, and Minoru Fujii. An investigation into second harmonic generation by Si-rich SiNx thin films deposited by rf sputtering over a wide range of si concentrations. *Journal of Physics D: Applied Physics*, 47(21):215101, 2014.
- [77] Tingyin Ning, Chunlei Tan, Tapio Niemi, Martti Kauranen, and Goëry Genty. Enhancement of second-harmonic generation from silicon nitride with gold gratings. *Opt. Express*, 23(24):30695–30700, Nov 2015.
- [78] Ori Hazut, Arunava Agarwala, Iddo Amit, Thangavel Subramani, Seva Zaidiner, Yossi Rosenwaks, and Roie Yerushalmi. Contact doping of silicon wafers and nanostructures with phosphine oxide monolayers. *ACS Nano*, 6(11):10311–10318, 2012. PMID: 23083376.
- [79] Laurent Mathey, Thibault Alphazan, Maxence Valla, Laurent Veyre, Hervé Fontaine, Virginie Enyedi, Karim Yckache, Marianne Danielou, Sébastien Kerdiles, Jean Guerrero, Jean-Paul Barnes, Marc Veillerot, Nicolas Chevalier, Denis Mariolle, François Bertin, Corentin Durand, Maxime Berthe, Jolien Dendooven, François Martin, Chloé Thieuleux, Bruno Grandidier, and Christophe Copéret. Functionalization of silica nanoparticles and native silicon oxide with tailored boron-molecular precursors for efficient and predictive p-doping of silicon. *The Journal of Physical Chemistry C*, 119(24):13750–13757, 2015.
- [80] John O’Connell, Giuseppe Alessio Verni, Anushka Gangnaik, Maryam Shayesteh, Brenda Long, Yordan M. Georgiev, Nikolay Petkov, Gerard P. McGlacken, Michael A. Morris, Ray Duffy, and Justin D. Holmes. Organo-arsenic molecular layers on silicon for high-density doping. *ACS Applied Materials & Interfaces*, 7(28):15514–15521, 2015. PMID: 26111734.
- [81] A. Pereyaslavtsev, I. Sokolov, and A. Vatopedsky. Complex investigation of multilayer nanostructure of a-Si/SiO_{1.9} by probe and spectroscopic analysis

- techniques. visualization of the band structure. studying of the band structure of the suboxide border layers. *Surface and Interface Analysis*, 47(4):498–505, 2015. SIA-14-0340.R1.
- [82] F. Priolo, T. Gregorkiewicz, M. Galli, and T. F. Krauss. Silicon nanostructures for photonics and photovoltaics. *Nat. Nano.*, 9:19 – 32, Jan 2014.
- [83] Erik M. Grumstrup, Emma M. Cating, Michelle M. Gabriel, Christopher W. Pinion, Joseph D. Christesen, Justin R. Kirschbrown, Ernest L. Vallorz, James F. Cahoon, and John M. Papanikolas. Ultrafast carrier dynamics of silicon nanowire ensembles: The impact of geometrical heterogeneity on charge carrier lifetime. *The Journal of Physical Chemistry C*, 118(16):8626–8633, 2014.
- [84] Maarten K. Vanbel, Chen-Yi Su, Jean-Pierre Locquet, and Thierry Verbiest. Electric-Field-Induced Second-Harmonic Generation Demonstrates Different Interface Properties of Molecular Beam Epitaxy Grown MgO on Si. *The Journal of Physical Chemistry C*, 118(4):1919–1924, 2014.
- [85] Long He. *Optical Second Harmonic Generation Measurements for Characterization of Amorphous Silicon Interfaces*. PhD thesis, University of Colorado Boulder, July 2014.
- [86] D. Damianos, L. Pirro, G. Soylu, I. Ionica, Nguyen V., G. Vitrant, A. Kaminski, D. Blanc-Pelissier, L. Onestas, J. Changala, M. Kryger, and S. Cristoloveanu. Second harmonic generation for contactless non-destructive characterization of silicon on insulator wafers. *Solid-State Electronics*, 115, Part B:237 – 243, Jan 2016. Selected papers from the EUROSOI-ULIS conference.
- [87] M. K. Vanbel, V. V. Afanas'ev, C. Adelman, M. Caymax, V. K. Valev, and T. Verbiest. Tunneling of holes is observed by second-harmonic generation. *Applied Physics Letters*, 102(8), 2013.
- [88] Yong Q. An, J. Price, Ming Lei, and M. C. Downer. Role of photo-assisted tunneling in time-dependent second-harmonic generation from si surfaces with ultrathin oxides. *Applied Physics Letters*, 102(5), 2013.
- [89] C. A. Nelson, J. Luo, A. K.-Y. Jen, R. B. Laghumavarapu, D. L. Huffaker, and X.-Y. Zhu. Time-, energy-, and phase-resolved second-harmonic generation at semiconductor interfaces. *The Journal of Physical Chemistry C*, 118(48):27981–27988, 2014.
- [90] WI Ndebeka, PH Neethling, CM Steenkamp, H Stafast, and EG Rohwer. Investigated charge carrier effects in silicon membranes using a femtosecond laser. In *Proceedings of The 60 th annual conference of The South African Institute of Physics (SAIP2015)*, pages 260–266. The South African Institute of Physics (SAIP), 2016.

- [91] Wilfrid I. Ndebeka, Herbert Stafast, Erich Rohwer, Christine Steenkamp, and Pieter Neethling. Investigation of free charge carrier effects in silicon membranes. In *Frontiers in Optics 2015*, page JTU4A.84. Optical Society of America, 2015.
- [92] F.L. Pedrotti and L.S. Pedrotti. *Introduction to Optics*. Prentice Hall, 1993.
- [93] E. Hecht. *Optics*. Pearson Education, third edition edition, 2003.
- [94] D.K. Schroder, R.N. Thomas, and J.C. Swartz. Free carrier absorption in silicon. *Electron Devices, IEEE Transactions on*, 25(2):254–261, Feb 1978.
- [95] J. Geist, A.R. Schaefer, J.F. Song, Y.H. Wang, and E.F. Zalewski. An accurate value for the absorption coefficient of silicon at 633 nm. *Journal of Research of NIST*, 95(5):549, 1990.
- [96] Robert W. Boyd. *Nonlinear Optics, Third Edition*. Academic Press, 3 edition, April 2008.
- [97] Alejandro A. Duarte and Hernán G. Solari. Slowly varying envelope approximation in a laser with optical feedback. *Phys. Rev. A*, 64:033803, Aug 2001.
- [98] A.E. Siegman. *Lasers*. University Science Books, 1986.
- [99] G.P. Agrawal and N.K. Dutta. Long-wavelength semiconductor lasers. Van Nostrand Reinhold electrical/computer science and engineering series. Van Nostrand Reinhold, 1986.
- [100] Y.R. Shen. Surfaces probed by nonlinear optics. *Surface Science*, 299 – 300(0):551 – 562, 1994.
- [101] Y.R. Shen. Surface studies by optical second harmonic generation: An overview. *Journal of Vacuum Science Technology B: Microelectronics and Nanometer Structures*, 3(5):1464–1466, 1985.
- [102] Jerry I. Dadap, Jie Shan, and Tony F. Heinz. Theory of optical second-harmonic generation from a sphere of centrosymmetric material: small-particle limit. *J. Opt. Soc. Am. B*, 21(7):1328–1347, Jul 2004.
- [103] Y.R. Shen. Wave mixing spectroscopy for surface studies. *Solid State Communications*, 102(2–3):221–229, 1997. Highlights in Condensed Matter Physics and Materials Science.
- [104] J. F. McGilp. Optical second-harmonic generation as a semiconductor surface and interface probe. *physica status solidi (a)*, 175(1):153–167, 1999.
- [105] M.C. Gupta and J. Ballato. *The Handbook of Photonics, Second Edition*. Taylor & Francis, 2006.
- [106] G. Nyamuda. Optical second harmonic generation and pump-probe reflectivity measurements from Si/SiO₂ interfaces. PhD thesis, Univeristy of Stellenbosch, December 2010.

- [107] J. H. Bechtel and W. L. Smith. Two-photon absorption in semiconductors with picosecond laser pulses. *Phys. Rev. B*, 13:3515–3522, Apr 1976.
- [108] P.W. Milonni and J.H. Eberly. *Lasers*. Wiley Series in Pure and Applied Optics. Wiley, 1988.
- [109] G.S. He and S.H. Liu. *Physics of nonlinear optics*. World Scientific Publishing Company Incorporated, 1999.
- [110] M. Sheik-Bahae, D. J. Hagan, and E. W. Van Stryland. Dispersion and band-gap scaling of the electronic kerr effect in solids associated with two-photon absorption. *Phys. Rev. Lett.*, 65:96–99, Jul 1990.
- [111] M. Sheik-Bahae, A. A. Said, and E. W. Van Stryland. High-sensitivity, single-beam n_2 measurements. *Opt. Lett.*, 14(17):955–957, Sep 1989.
- [112] Lina Yang, R. Dorsinville, Q. Z. Wang, P. X. Ye, R. R. Alfano, R. Zamboni, and C. Taliani. Excited-state nonlinearity in polythiophene thin films investigated by the z-scan technique. *Opt. Lett.*, 17(5):323–325, Mar 1992.
- [113] J. Wang, M. Sheik-Bahae, A. A. Said, D. J. Hagan, and E. W. Van Stryland. Time-resolved z-scan measurements of optical nonlinearities. *J. Opt. Soc. Am. B*, 11(6):1009–1017, Jun 1994.
- [114] L.C. Oliveira and S.C. Zilio. Single-beam time-resolved z-scan measurements of slow absorbers. *Applied Physics Letters*, 65(17):2121, 1994.
- [115] S. Hughes, J. M. Burzler, G. Spruce, and B. S. Wherrett. Fast fourier transform techniques for efficient simulation of z-scan measurements. *J. Opt. Soc. Am. B*, 12(10):1888–1893, Oct 1995.
- [116] S. M. Mian, B. Taheri, and J. P. Wicksted. Effects of beam ellipticity on z-scan measurements. *J. Opt. Soc. Am. B*, 13(5):856–863, May 1996.
- [117] Marek Samoc, Anna Samoc, Barry Luther-Davies, Zhenan Bao, Luping Yu, Bing Hsieh, and Ullrich Scherf. Femtosecond z-scan and degenerate four-wave mixing measurements of real and imaginary parts of the third-order nonlinearity of soluble conjugated polymers. *J. Opt. Soc. Am. B*, 15(2):817–825, Feb 1998.
- [118] Chong Hoon Kwak, Yeung Lak Lee, and Seong Gyu Kim. Analysis of asymmetric z-scan measurement for large optical nonlinearities in an amorphous As_2S_3 thin film. *J. Opt. Soc. Am. B*, 16(4):600–604, Apr 1999.
- [119] Minjoung Kyoung and Minyung Lee. Nonlinear absorption and refractive index measurements of silver nanorods by the z-scan technique. *Optics Communications*, 171(1–3):145 – 148, 1999.
- [120] M. Yin, H.P. Li, S.H. Tang, and W. Ji. Determination of nonlinear absorption and refraction by single z-scan method. *Applied Physics B: Lasers & Optics*, 70(4):587, 2000.

- [121] R. de Nalda, R. del Coso, J. Requejo-Isidro, J. Olivares, A. Suarez-Garcia, J. Solis, and C. N. Afonso. Limits to the determination of the nonlinear refractive index by the z-scan method. *J. Opt. Soc. Am. B*, 19(2):289–296, Feb 2002.
- [122] Thomas Olivier, Franck Billard, and Hassan Akhouayri. Nanosecond z-scan measurements of the nonlinear refractive index of fused silica. *Opt. Express*, 12(7):1377–1382, Apr 2004.
- [123] Bing Gu, Jing Chen, Ya-Xian Fan, Jianping Ding, and Hui-Tian Wang. Theory of gaussian beam z scan with simultaneous third- and fifth-order nonlinear refraction based on a gaussian decomposition method. *J. Opt. Soc. Am. B*, 22(12):2651–2659, Dec 2005.
- [124] Martin C. Fischer, Henry C. Liu, Ivan R. Piletic, and Warren S. Warren. Simultaneous self-phase modulation and two-photon absorption measurement by a spectral homodyne z-scan method. *Opt. Express*, 16(6):4192–4205, Mar 2008.
- [125] Jianwei Wu and Fengguang Luo. Ultrafast femtosecond all-optical modulation through nondegenerate two-photon absorption in silicon-on-insulator waveguides. *Journal of Russian Laser Research*, 29(5):490–496, 2008.
- [126] L. Pálfalvi, B. Tóth, G. Almási, J. Fölöp, and J. Hebling. A general z-scan theory. *Applied Physics B: Lasers & Optics*, 97(3):679 – 685, 2009.
- [127] M. Dinu, F. Quochi, and H. Garcia. Third-order nonlinearities in silicon at telecom wavelengths. *Applied Physics Letters*, 82(18):2954–2956, 2003.
- [128] Alan D. Bristow, Nir Rotenberg, and Henry M. van Driel. Two-photon absorption and kerr coefficients of silicon for 850–2200 nm. *Applied Physics Letters*, 90(19):191104, 2007.
- [129] E.D. Palik. *Handbook of Optical Constants of Solids*. Academic Press handbook series. Academic Press, p.547, 1991.
- [130] Todd D. Krauss and Frank W. Wise. Femtosecond measurement of nonlinear absorption and refraction in CdS, ZnSe, and ZnS. *Applied Physics Letters*, 65(14):1739, 1994.
- [131] Yunjin Choi, June H. Park, Myong R. Kim, Wonho Jhe, and Bum Ku Rhee. Direct observation of self-focusing near the diffraction limit in polycrystalline silicon film. *Applied Physics Letters*, 78(7):856, 2001.
- [132] N. Bloembergen and P. S. Pershan. Light waves at the boundary of nonlinear media. *Phys. Rev.*, 128:606–622, Oct 1962.
- [133] P. S. Pershan. Nonlinear optical properties of solids: Energy considerations. *Phys. Rev.*, 130:919–929, May 1963.

- [134] Fielding Brown, Robert E. Parks, and Arthur M. Sleeper. Nonlinear optical reflection from a metallic boundary. *Phys. Rev. Lett.*, 14:1029–1031, Jun 1965.
- [135] Sudhanshu S. Jha. Nonlinear optical reflection from a metal surface. *Phys. Rev. Lett.*, 15:412–414, Aug 1965.
- [136] C. H. Lee, R. K. Chang, and N. Bloembergen. Nonlinear electroreflectance in silicon and silver. *Phys. Rev. Lett.*, 18:167–170, Jan 1967.
- [137] TF Heinz, HE Ponath, and GI Stegeman. Nonlinear surface electromagnetic phenomena. *by H. E. Ponath and GI Stegeman (Elsevier Science Publishers BV, Amsterdam, 1991) p, 353, 1991.*
- [138] D. Guidotti, T.A. Driscoll, and H.J. Gerritsen. Second harmonic generation in centro-symmetric semiconductors. *Solid State Communications*, 46(4):337–340, 1983.
- [139] P. Guyot-Sionnest, W. Chen, and Y. R. Shen. General considerations on optical second-harmonic generation from surfaces and interfaces. *Phys. Rev. B*, 33:8254–8263, Jun 1986.
- [140] P. Guyot-Sionnest and Y. R. Shen. Bulk contribution in surface second-harmonic generation. *Phys. Rev. B*, 38:7985–7989, Oct 1988.
- [141] J.H. Thomas III and F.J. Feigl. Electron trapping levels in silicon dioxide thermally grown on silicon. *Journal of Physics and Chemistry of Solids*, 33(12):2197 – 2216, 1972.
- [142] Vasilii Fomenko, Cédric Hurth, Tao Ye, and Eric Borguet. Second harmonic generation investigations of charge transfer at chemically-modified semiconductor interfaces. *Journal of Applied Physics*, 91(7):4394, 2002.
- [143] R.L. Sutherland, D.G. McLean, and S. Kirkpatrick. Handbook of nonlinear optics. Optical Engineering - Marcel Dekker. MARCEL DEKKER Incorporated, 2003.
- [144] V. Raghunathan, R. Shori, O. M. Stafsudd, and B. Jalali. Nonlinear absorption in silicon and the prospects of mid-infrared silicon raman lasers. *physica status solidi (a)*, 203(5):R38–R40, 2006.
- [145] H.E. Ponath and G.I. Stegeman. Nonlinear Surface Electromagnetic Phenomena, edited by H.-E. Ponath and G. I. Stegeman, Modern Problems in Condensed Matter Sciences Vol. 29 (North-Holland, Amsterdam, 1991), p. 355. Modern Problems in Condensed Matter Sciences. Elsevier Science, 1991.
- [146] G. Lüpke, S. Lehmann, G. Marowsky, C. Meyer, C. Ohlhoff, and H. Kurz. Optical second-harmonic generation as a probe of electric-field-induced perturbation of centrosymmetric media. *Opt. Lett.*, 20(19):1997–1999, Oct 1995.

- [147] Scheidt T., Rohwer E.G., Bergmann H.M.V., and Stafast H. Femtosecond laser diagnostics of thin films, surfaces and interfaces. *South African J. Science*, 101:267–271, May/June 2005.
- [148] Oksana Ostroverkhova, Andrew Stickrath, and Kenneth D. Singer. Electric field-induced second harmonic generation studies of chromophore orientational dynamics in photorefractive polymers. *Journal of Applied Physics*, 91(12):9481–9486, 2002.
- [149] D. J. DiMaria, E. Cartier, and D. Arnold. Impact ionization, trap creation, degradation, and breakdown in silicon dioxide films on silicon. *Journal of Applied Physics*, 73(7):3367, 1993.
- [150] P.H. Neethling, T. Scheidt, E.G. Rohwer, H.M. von Bergmann, and H. Stafast. Second harmonic generation as a technique to probe buried interfaces. *South African Journal of Science*, 105:282–284, 08 2009.
- [151] T. Scheidt, E. G. Rohwer, H. M. von Bergmann, and H. Stafast. Optical second harmonic imaging: a versatile tool to investigate semiconductor surfaces and interfaces. *European Physical Journal: Applied Physics*, 27:393–397, 2004.
- [152] G.A. Reider, M. Cernusca, and M. Hofer. Coherence artifacts in second harmonic microscopy. *Applied Physics B: Lasers & Optics*, 68(3):343, 1999.
- [153] N. Shamir, J. G. Mihaychuk, H. M. van Driel, and H. J. Kreuzer. Universal mechanism for gas adsorption and electron trapping on oxidized silicon. *Phys. Rev. Lett.*, 82:359–361, Jan 1999.
- [154] Yu. D. Glinka, W. Wang, S. K. Singh, Z. Marka, S. N. Rashkeev, Y. Shirokaya, R. Albridge, S. T. Pantelides, N. H. Tolk, and G. Lucovsky. Characterization of charge-carrier dynamics in thin oxide layers on silicon by second harmonic generation. *Phys. Rev. B*, 65:193103, Apr 2002.
- [155] K. Sokolowski-Tinten, J. Bialkowski, and D. von der Linde. Ultrafast laser-induced order-disorder transitions in semiconductors. *Phys. Rev. B*, 51:14186–14198, May 1995.
- [156] Janusz Bogdanowicz, Fabian Dortu, Trudo Clarysse, Wilfried Vandervorst, and Alex Salnik. Electrothermal theory of photomodulated optical reflectance on active doping profiles in silicon. *Journal of Applied Physics*, 108(10), 2010.
- [157] G. Vuye, S. Fisson, V. Nguyen Van, Y. Wang, J. Rivory, and F. Abeles. Temperature dependence of the electric function of silicon using in situ spectroscopic ellipsometry. *Thin Solid Films*, 1993.
- [158] E.D. Palik. *Handbook of Optical Constants of Solids*. Number v. 3 in Academic Press handbook series. Academic Press, 1998.
- [159] Heungman Park, Jingbo Qi, Ying Xu, Gunter Lüpke, and Norman Tolk. Polarization-dependent temporal behaviour of second harmonic generation in Si/SiO₂ systems. *Journal of Optics*, 13(5):055202, 2011.

- [160] Adrian Dragonmir, John G. McInerney, and David N. Nikogosyan. Femtosecond measurements of two-photon absorption coefficients at $\lambda = 264$ nm in glasses, crystals, and liquids. *Appl. Opt.*, 41(21):4365–4376, Jul 2002.
- [161] D.J. Griffiths. *Introduction to Electrodynamics*. Prentice Hall, 1999.
- [162] P. H. Neethling, E. G. Rohwer, and H. Stafast. Femtosecond laser diagnostics of the built-in electric field across the p⁺-Si/SiO₂ interface and its ultrafast shielding. *Journal of Applied Physics*, 113(22):–, 2013.
- [163] D. J. Sandiford. Temperature dependence of carrier lifetime in silicon. *Proc. Phys. Soc.*, 71:1002, 1958.
- [164] C.M. Horwitz and R.M. Swanson. The optical (free-carrier) absorption of a hole-electron plasma in silicon. *Solid-State Electronics*, 23(12):1191–1194, 1980.
- [165] H. Y. Fan, Spitzer W., and R. J. Collins. Infrared absorption in *n*-type germanium. *Phys. Rev.*, 101:566–572, Jan 1956.
- [166] W. Spitzer and H. Y. Fan. Infrared absorption in *n*-type silicon. *Phys. Rev.*, 108:268–271, Oct 1957.
- [167] K G Svantesson and N G Nilsson. Determination of the temperature dependence of the free carrier and interband absorption in silicon at 1.06 μ m. *Journal of Physics C: Solid State Physics*, 12(18):3837, 1979.
- [168] V. Grivitskas, M. Willander, and J. Vaitkus. The role of intercarrier scattering in excited silicon. *Solid-State Electronics*, 27(6):565 – 572, 1984.
- [169] J. M. Liu, H. Kurz, and N. Bloembergen. Picosecond time-resolved plasma and temperature-induced changes of reflectivity and transmission. *Applied Physics Letters*, 41(7):643–646, 1982.
- [170] Richard A. Soref and B.R. Bennett. Electrooptical effects in silicon. *Quantum Electronics, IEEE Journal of*, 23(1):123–129, Jan 1987.
- [171] Bo E. Sernelius. Optical free-carrier absorption of an electron-hole plasma in silicon. *Phys. Rev. B*, 39:10825–10830, May 1989.
- [172] D.K. Schroder. Carrier lifetimes in silicon. *Electron Devices, IEEE Transactions on*, 44(1):160–170, Jan 1997.
- [173] Jan Linnros. Carrier lifetime measurements using free carrier absorption transients. I. Principle and injection dependence. *Journal of Applied Physics*, 84(1):275, 1998.
- [174] Jan Linnros. Carrier lifetime measurements using free carrier absorption transients. ii. lifetime mapping and. *Journal of Applied Physics*, 84(1):284, 1998.

- [175] Jet Meitzner, Frederick G. Moore, Brock M. Tillotson, Stephen D. Kevan, and Geraldine L. Richmond. Time-resolved measurement of free carrier absorption, diffusivity, and internal quantum efficiency in silicon. *Applied Physics Letters*, 103(9):092101, 2013.
- [176] Martina De Laurentis and Andrea Irace. Optical measurement techniques of recombination lifetime based on the free carriers absorption effect. *Journal of Solid State Physics*, 2014:291469, 2014.
- [177] J. E. Geusic, S. Singh, D. W. Tipping, and T. C. Rich. Three-photon stepwise optical limiting in silicon. *Phys. Rev. Lett.*, 19:1126–1128, Nov 1967.
- [178] J. M. Ralston and R. K. Chang. Optical limiting in semiconductors. *Applied Physics Letters*, 15(6):164–166, 1969.
- [179] W. B. Gauster and J. C. Bushnell. Laser-induced infrared absorption in silicon. *Journal of Applied Physics*, 41(9):3850–3853, 1970.
- [180] John F. Reintjes and James C. McGroddy. Indirect two-photon transitions in Si at 1.06 μm . *Phys. Rev. Lett.*, 30:901–903, May 1973.
- [181] Rubin Braunstein, Arnold R. Moore, and Frank Herman. Intrinsic optical absorption in germanium-silicon alloys. *Phys. Rev.*, 109:695–710, Feb 1958.
- [182] Martin A. Green. Self-consistent optical parameters of intrinsic silicon at 300 k including temperature coefficients. *Solar Energy Materials and Solar Cells*, 92(11):1305 – 1310, 2008.
- [183] V. I. Gavrilenko. Differential reflectance and second-harmonic generation of the Si/SiO₂ interface from first principles. *Phys. Rev. B*, 77:155311, Apr 2008.
- [184] S.A Mitchell, M Mehendale, D.M Villeneuve, and R Boukherroub. Second harmonic generation spectroscopy of chemically modified Si(111) surfaces. *Surface Science*, 488(3):367 – 378, 2001.
- [185] A. Rumpel, B. Manschwetus, G. Lilienkamp, H. Schmidt, and W. Daum. Polarity of space charge fields in second-harmonic generation spectra of Si(100)/SiO₂ interfaces. *Phys. Rev. B*, 74:081303, Aug 2006.
- [186] W. Daum. Optical studies of Si/SiO₂ interfaces by second-harmonic generation spectroscopy of silicon interband transitions. *Applied Physics A*, 87(3):451–460, 2007.
- [187] Heiji Watanabe, Ken Fujita, and Masakazu Ichikawa. Observation and creation of current leakage sites in ultrathin silicon dioxide films using scanning tunneling microscopy. *Applied Physics Letters*, 72(16):1987–1989, 1998.
- [188] B. Kaczer, Z. Meng, and J. P. Pelz. Nanometer-scale creation and characterization of trapped charge in SiO₂ films using ballistic electron emission microscopy. *Phys. Rev. Lett.*, 77:91–94, Jul 1996.

- [189] P. Balk. *The Si-SiO₂ system*, volume 32 of *Materials science monographs*. Elsevier, 1988.